Research and Development of a Multiplexed Readout for Micromegas Detectors

Masterarbeit an der Fakultät für Physik
der
Ludwig-Maximilians-Universität München

vorgelegt von

Christoph Simon Maximilian Jagfeld
geboren in München

München, den 11.06.2019

Forschung und Entwicklung einer gemultiplexten Auslese für Micromegas Detektoren

Masterarbeit an der Fakultät für Physik
der
Ludwig-Maximilians-Universität München

vorgelegt von
Christoph Simon Maximilian Jagfeld
geboren in München

München, den 11.06.2019

Gutachter: Prof. Dr. Otmar Biebel

Abstract

In Micro-MEsh GAseous Structures (Micromegas) detectors, a modern form of micro-pattern gaseous detectors, every single micro strip is read out by a single electronic channel. For large scale Micromegas detectors this results in a huge demand of electronic readout channels and corresponding readout electronics. High power consumption and heat dissipation are a consequence, as well as a huge amount of data acquired by measurements. A reduction of the electronics is also desirable from financial aspects.
One possibility to achieve a reduction of electronic channels is the usage of a multiplexed readout. In this thesis a multiplex readout scheme is developed and investigated that reduces the electronics by a factor of two by connecting two readout strips to the same electronic channel.
The developed multiplexed readout is tested with a high intensity 20 MeV proton beam at different angles of inclination, using a small sized Micromegas strip detector. The impact of the multiplexed readout on the position reconstruction efficiency, angular resolution and signal pulse height is studied.
Finally, the impact of the multiplexed readout on $2\,\mathrm{m}^2$ large strip Micromegas detectors is studied. Therefore, measurements with cosmic muons were performed at the cosmic ray facility of our institute with emphasis on the impact of the multiplexed readout on the efficiency and the spatial resolution.
While the influence of the multiplexed readout is barely noticeable in small sized detectors, the influence of the increased capacitance by coupling of several strips is reflected in the measured properties of large sized detectors.

Kurzfassung

Micromegas Detektoren sind eine moderne Form von mikrostrukturierter Gasdetektoren. Aktuell wird jeder einzelne Mikrostreifen von einem eigenen elektronischen Kanal ausgelesen. Für großflächige Micromegas-Detektoren führt dies zu einem enormen Bedarf an elektronischen Auslesekanälen und entsprechender Ausleseelektronik. Sowohl ein hoher Stromverbrauch und eine hohe Wärmeabgabe sind die Folge als auch eine riesige Menge an Messdaten. Auch aus finanzieller Sicht ist eine Reduzierung der Elektronik ebenfalls wünschenswert.
Eine Möglichkeit, die benötigten elektronischen Kanäle zu verringern, ist die Anwendung einer gemultiplexten Auslese. In dieser Arbeit wird ein Multiplex-Ausleseschema entwickelt und untersucht. Dieses verringert die Elektronik um den Faktor zwei indem zwei Auslesestreifen an denselben elektronischen Kanal angeschlossen werden.
Die entwickelte Multiplexauslese wird mit einem 20 MeV Protonenstrahl unter verschiedenen Einfallswinkeln an einem $10 \times 10\,\mathrm{cm}^2$ großem Micromegas Detektor getestet. Der Einfluss der gemultiplexten Auslese auf die Positionsrekonstruktionseffizienz, die Winkelauflösung und die Signalimpulshöhe wird untersucht.
Schließlich wird die Auswirkung der gemultiplexten Auslese auf großflächige Micromegas-Detektoren untersucht. Hierfür wurden Messungen mit kosmischen Myonen am Myonen Teststand unseres Institutes durchgeführt. Bei diesen Messungen stand der Einfluss der gemultiplexten Auslesung auf die Effizienz und die räumliche Auflösung im Vordergrund.
Während sich bei kleinflächigen Detektoren der Einfluss der gemultiplexed Auslese kaum bemerkbar macht, spiegelt sich der Einfluss, der erhöhten Kapazität durch Kopplung mehrerer Streifen, in den gemessenen Eigenschaften großflächiger Detektoren wieder.

Contents

Chapter 1

Particle Detection with Micromegas Detectors

Gaseous detectors are used in many fields of high energy physics. A simple design makes it usable in versatile applications. Next to particle physics they can be used for instance for medical imaging or for muon tomography. A common type of gaseous detectors is the MICROMEsh GAseous Structure detector (Micromegas), a modern form of micro-pattern detectors. It is a high-rate capable position-sensitive particle detector, first time presented by Giomataris in 1996 [Giomataris et al., 1996].
One of the first large high energy particle physics experiment, using Micromegas detectors is the COMPASS[1] experiment at the "European Organization for Nuclear Research" near Geneva (CERN). In this experiment Micromegas detectors are successfully taking data since the start of operation in 2002 [Abbon et al., 2007].
Nowadays small and medium sized Micromegas detectors with an active area up to approximately 0.2 m^2 are used in various experiments and applications. The first experiment which is going to use large scale Micromegas detectors with a size of a few square meters is the ATLAS[2] experiment at CERN [Iodice, 2015].
Due to the expected luminosity upgrade of the LHC[3] by a factor of five with respect to the design luminosity [Stelzer, 2016] the inner most muon spectrometer in the end-cap region (see figure 1.1) needs to be replaced with high rate capable detectors. "small-strip Thin Gas Chambers"[4] and Micromegas detectors are going to replace the currently used Monitored Drift Tubes (MDTs), which are incapable to reconstruct precise muon tracks with a high efficiency in a high background radiation region [Kawamoto et al., 2013]. Some of the Micromegas detectors for this upgrade, the so called SM2 modules, are developed and constructed by a German collaboration in which the LMU Munich participates. This detector is described later on in chapter 5.1.2.

[1] The "COmmon Muon Proton Apparatus for Structure and Spectroscopy" experiment at CERN studies the hadron structure and hadron spectroscopy with high intensity muon and hadron beams[Baum et al., 1996]

[2] The "A Toroidal LHC ApparatuS" experiment is a general-purpose experiment located at the LHC. It is most famous for the discovery of the Higgs boson [ATLAS, 2019].

[3] With a circumference of 27km "the Large Hadron Collider" at CERN is the particle accelerator with the highest center of mass energy worldwide. Protons are collided at the LHC [CERN, 2019a].

[4] small-strip Thin Gas Chambers (sTGC) are multi-wire proportional chambers

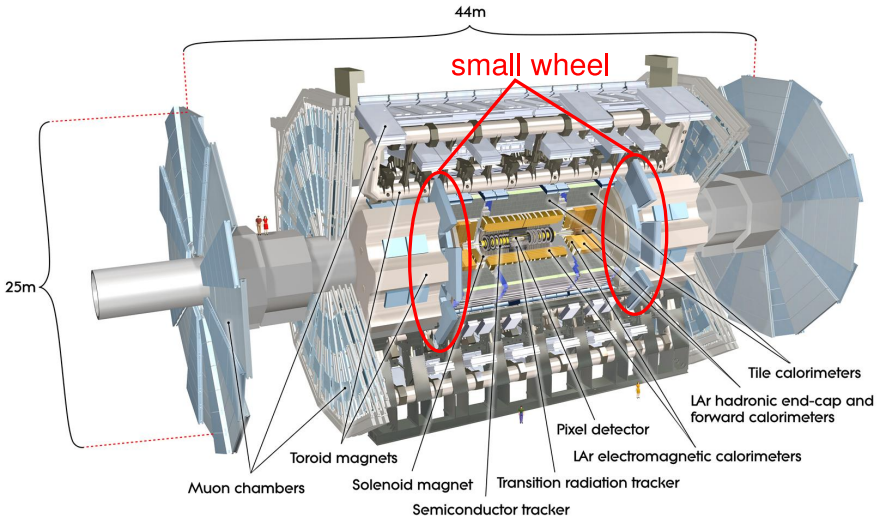

Figure 1.1: Schematic picture of the ATLAS experiment (adapted from [ATLAS, 2019]).
The outer most blueish detectors are the muon spectrometer. A part of the muon spectrometer, the small wheel is going to be replaced in the near future.

1.1 Interactions of Charged Particles with Matter

The interaction of particles with matter is the underlying process for particle detection with gaseous detectors. When a charged particle traverses a medium, it mainly interacts with the atoms via inelastic scattering [Frauenfelder and Henley, 1987]. The energy loss due to the inelastic scattering can lead to an ionization of the medium. Gaseous detectors are measuring the charge, which is created in a gaseous medium by ionizing radiation.

1.1.1 Multiple Scattering

Charged particles going through a medium are scattered by small angles multiple times. Leptons are mostly deflected due to Coulomb scattering [Tanabashi, 2018]. The distribution of the scattering angle is roughly Gaussian. The mean of the distribution is around zero. The width of the distribution is a measure for the degree of scattering. It is given by [Lynch and Dahl, 1991]:

$$\sigma = \frac{13.6MeV}{\beta cp} z \sqrt{\frac{x}{X_0}} \left[1 + 0.038 \ln\left(\frac{x}{X_0}\right)\right] \tag{1.1}$$

with βc: velocity of the incident particle, p : momentum of the incident particle, z: charge number of the incident particle, x: thickness of the scattering medium, and X_0: radiation length of the scattering medium.
As shown in equation 1.1, the width of the angular distribution shrinks with an increasing energy of the incident particle.

1.1.2 Energy Loss Described by the Bethe Bloch Equation

Heavy charged particles traversing a medium lose energy due to Coulomb interaction with bound electrons of the medium. Either the atom can be excited or ionized. With increasing energy of the traversing particle the probability for ionization increases[Frauenfelder and Henley, 1987].
The mean energy loss of heavy particles with $0.1 \lesssim \beta\gamma \lesssim 1000$ is well described by the Bethe Bloch equation [Tanabashi, 2018]:

$$\frac{dE}{dx} = 4\pi N_A r_e^2 m_e c^2 \rho \frac{Z}{A}\frac{z^2}{\beta^2}\left[\frac{1}{2}\ln\left(\frac{2m_e c^2\beta^2\gamma^2 W_{max}}{I^2}\right) - \beta^2 - \frac{\delta(\beta\gamma)}{2}\right] \tag{1.2}$$

with N_A: Avogadro's number, r_e: classical electron radius, m_e: electron mass, c: speed of light in vacuum, ρ: density, Z: atomic number of absorber, A: atomic mass of absorber, z: charge number of incident particle, v: speed of the incident particle, $\beta = \frac{v}{c}$, $\gamma = \frac{1}{\sqrt{1-\beta^2}}$, I: mean excitation energy, $W_{\max}$: energy transfer to an electron in a single collision and δ: density effect correction to ionization energy loss.
The Bethe Bloch equation loses validity if the momentum of the incident particle is in the order of the momentum of the bound electrons of the medium [Frauenfelder and Henley, 1987]. The same applies for $\beta\gamma \gtrsim 1000$ where radiative energy losses are dominant (figure 1.2). The stopping power of a positive charged muon in copper is shown in figure 1.2.
For this thesis tests were performed with 20 MeV protons, 120 GeV pions and muons with an energy larger 600 MeV. Whereas the 20 MeV protons with $\beta\gamma \approx 0.02$ have a high mean energy loss per path length, the pions ($\beta\gamma \approx 900$) and muons $\beta\gamma \geq 60$ are essentially minimum ionizing particles (MIPs). As the name indicates MIPs have a small mean energy loss which is close to the minimum of the Bethe Bloch equation (see equation 1.2).

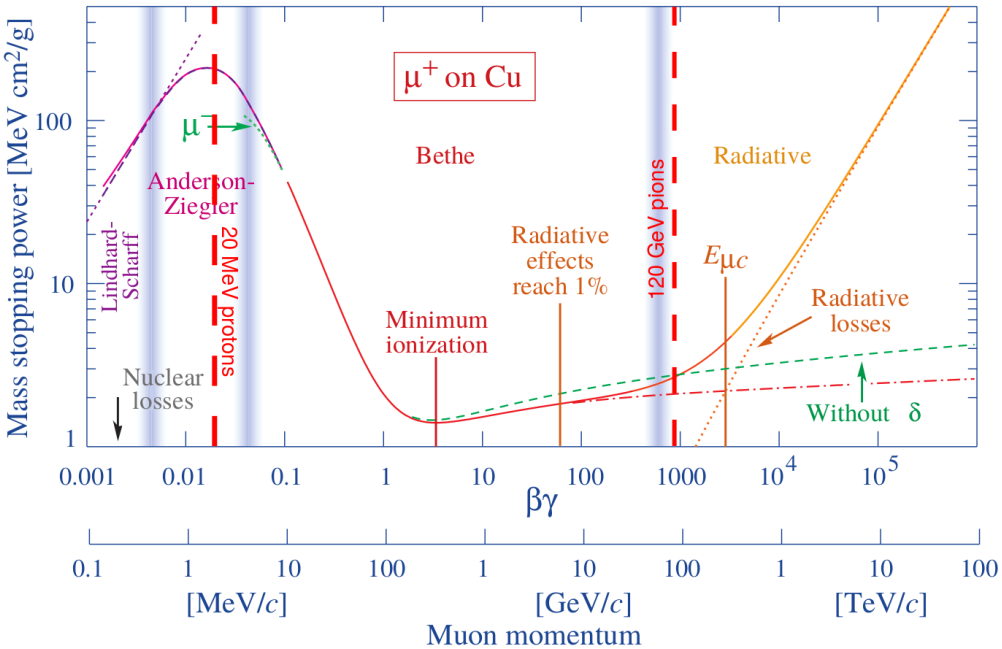

Figure 1.2: Mass stopping power of a positive charged muon in copper as a function of the momentum. Figure adapted from [Tanabashi, 2018].
The particles used for the measurements (20 MeV protons and 120 GeV pions) are marked.

1.1.3 Gas Amplification

The charge created by an ionizing particle traversing a gaseous medium is too small to be measured. Via gas amplification the charge can be multiplied. Gas amplification is one of the key processes in micro pattern gaseous detectors.
An electron inside a gas volume, which experiences an electric field ($\vec{E}$) due to a voltage between a cathode and an anode, gets accelerated towards the anode. If the electric field is large enough, the electron gains a kinetic energy higher than the ionization energy of the gas molecules. If this energy gain happens on a drift distance smaller than the mean free path length ($\lambda\left(\vec{E}\right)$), meaning between two collisions of the electron with a gas molecule, the electron can ionize the gas molecules at every collision [Kleinknecht, 2005]. Therefore the electron originating from the latest collision can ionize a gas molecule at the next collision again. Electron avalanches are created. This process can be described by following equation:

$$dN(x) = \alpha N(x)dx \tag{1.3}$$

with the first Townsend coefficient $\alpha = 1/\lambda\left(\vec{E}\right)$.
Solving this differential equation leads to a total number of existing free electrons (N(x)) after a drift distance x:

$$\begin{aligned} N(x) &= n_0 \cdot exp\left(\alpha x\right) \\ N(x) &= n_0 \cdot G \end{aligned} \tag{1.4}$$

The multiplication factor G is called gas gain. For a constant electric field, the first Townsend coefficient α depends on two constants A and B, on the gas pressure p, gas temperature T and on the electric field the electron experiences: [Townsend, 1910]

$$\begin{aligned} \alpha &= \frac{1}{\lambda\left(\vec{E}\right)} \\ \alpha &= \frac{A \cdot p}{T} \cdot exp\left(-\frac{B \cdot p}{\mid \vec{E} \mid \cdot T}\right) \end{aligned} \tag{1.5}$$

The gas gain can be calculated with equations 1.4 and 1.5:[Townsend, 1910]

$$G = exp\left[A \cdot \frac{p}{T} \cdot exp\left(-\frac{B \cdot p}{\mid \vec{E} \mid \cdot T}\right) \cdot x\right] \tag{1.6}$$

As seen in equation 1.6, the number of free electrons increases exponentially with an increasing drift distance x and increasing electric field $\vec{E}$. Therefore, also the charge of the avalanche increases.
The gas gain is limited due to space charge effects by the Raether limit at $x/\lambda \approx 20$.[Raether, 1964] When this value is exceeded a conducting plasma between the anode and the cathode can equalizes the potential between anode and cathode.
For a Micromegas detector the gas gain takes values up to 10^4 [Iodice, 2015].

1.2 Working Principle of the Micromegas Detector

For this thesis measurements were performed with a Micromegas detector. A schematic picture of a Micromegas detector is shown in figure 1.3. The Micromegas detector has a planar structure. It can be divided into two regions, a rather broad drift region (≈ 5 mm) and a much thinner (≈ 0.1 mm) amplification region.

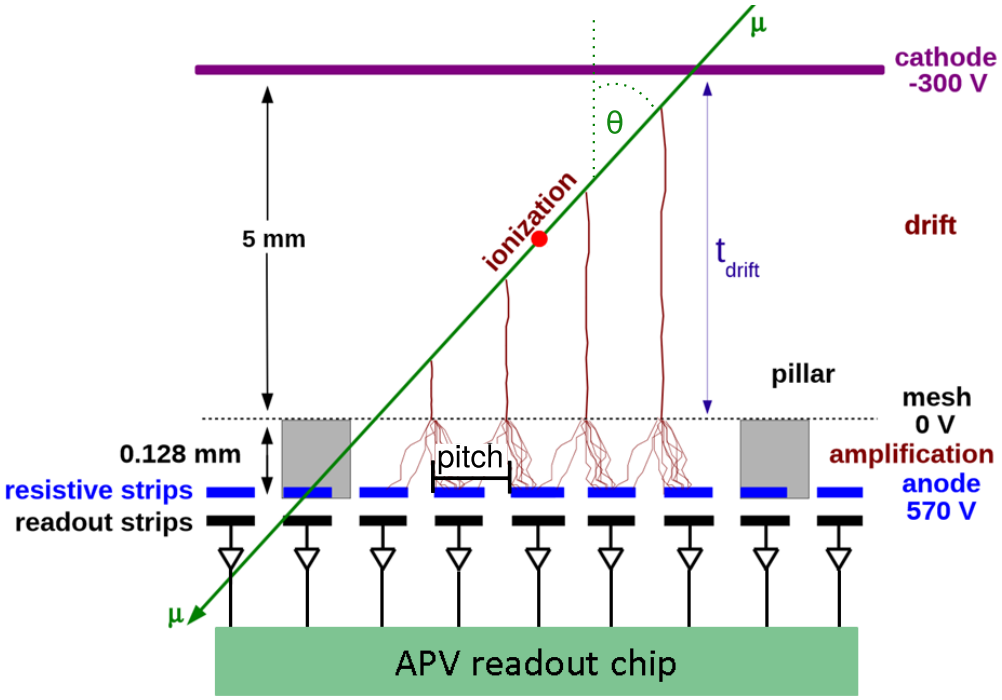

Figure 1.3: Sketch of a resistive strip Micromegas detector. A charged particle is traversing the detector and ionizing the gas along its path. Due to the high electric field between the mesh and the anode Townsend avalanches multiply the number of electrons. The electrons created by the avalanches are collected on the resistive strips and capacitively coupled to the readout strips which are connected to the readout electronics. Figure taken from [Lösel, 2017].

The drift region is confined by a cathode on the top and a stainless steel micro mesh on the bottom. Between the mesh and the cathode a potential difference causes an electric field in the order of $|\vec{E}_{\text{drift}}| = 0.5\,\text{kV/cm} - 1\,\text{kV/cm}$ [Giomataris et al., 1996].
The readout strips are located roughly 100 µm underneath the mesh and thus limiting the amplification region. With a value around $|\vec{E}_{\text{ampl}}| = 30\,\text{kV/cm} - 50\,\text{kV/cm}$ the electric field between the mesh and the readout strips is very high compared to $|\vec{E}_{\text{drift}}|$ [Giomataris et al., 1996]. For this thesis, if not otherwise stated, a gas mixture $\text{Ar} : \text{CO}_2$ 93 : 7 vol. % is flowing through the detector.
A charged particle traversing the detector is losing energy according to the Bethe Bloch equation (see equation 1.2). For a sufficient energy loss the atoms of the noble gas are ionized along the path of the particle. Due to the electric field ($\vec{E}_{\text{drift}}$) the electrons and the ions get separated. Whereas the ion drifts to the cathode, the electron is guided along the electric field lines through the mesh into the amplification region. For the correct ratio between $|\vec{E}_{\text{ampl}}|$ and $|\vec{E}_{\text{drift}}|$ the mesh is transparent to the drifting electrons (see figure 1.4).
In the amplification region the electrons are accelerated towards the readout strips due to the amplification field (E_{ampl}). Due to gas amplification, the charge of the primary signal increases exponentially (see equation 1.6) before it gets collected on the readout strips. De-

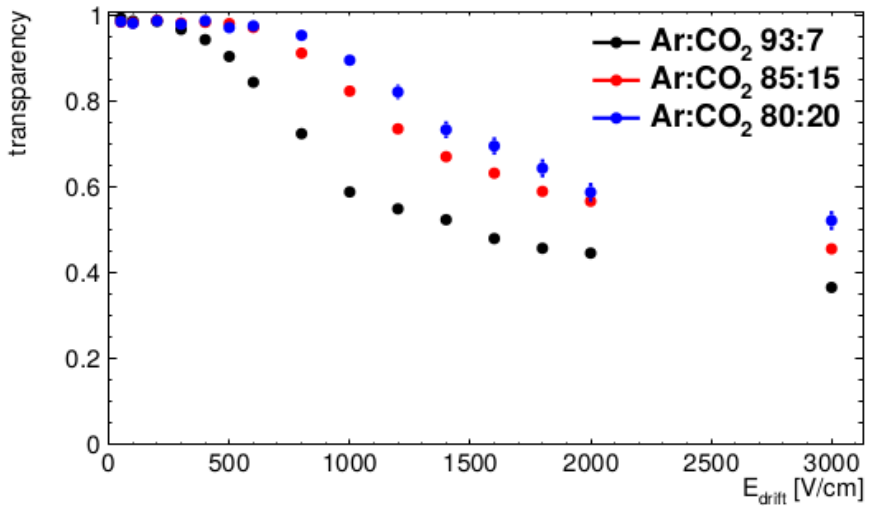

Figure 1.4: Electron transparency of the mesh as a function of the drift field for different gas mixtures. Figure taken from [Lösel, 2017].
Depending on U_{drift} the mesh becomes transparent to the drifting electrons.

pending on the periodicity of the readout strips (pitch) and the incident angle of the traversing particle the electron avalanche can be collected on multiple neighboring readout strips. The charge ($\mathcal{O}$(fC)) collected on the readout strips is read out via a front-end electronic readout chip.
If the gas amplification exceeds the Raether limit, the amplification voltage can break down due to plasma discharges (chapter 1.1.3). Until the voltage is brought up again, the detector is insensitive to traversing particles. To prevent the Micromegas detector from plasma discharges, or limit the discharge to a small area, discharge protections have to be applied [Alexopoulos et al., 2011]. This can be achieved by placing a layer of resistive strips, insulated from the readout strips, on top of the readout strips. In this case the amplification voltage is applied between the resistive strips and the mesh. Due to the resistivity of a few tens of MΩ/cm, and the thus resulting small currents[5] on the resistive strip, the electric field only drops locally.
The signal collected on the resistive strips is coupled via capacitive coupling to the readout strips. [Iodice, 2015]

[5] $I \leq \frac{U\text{ampl}}{R}$

1.3 Readout Electronics

To extract and amplify the charge signal from the detector ($\mathcal{O}$(fC)) and to digitize it, readout electronics is needed. For this thesis, the detectors are read out by a scalable readout system (SRS) using APV25 chips on hybrid boards to read out the detector (see figure 1.5) [RD51-collaboration, 2010].
The APV25 is an analoge readout chip designed for silicon strip detectors in the CMS tracker [Jones, 2001]. For limited particle fluxes and development purposes the APV25 can be used to read out Micromegas detectors. Each APV25 chip has 128 electronic channels. It integrates the charge of the readout strip signal in time interval of 25 ns [Jones, 2001]. The evolution of the collected charge on the readout strips can be observed by the APV25 every 25 ns for up to 27 samplings. The APV25 front-end board is connected to the Micromegas detector by a 130 pin Panasonic connector. Two APV25 front-end boards can be connected together. One type of front-end boards can act as a master whereas the other type acts as a slave. While the master front-end board is connected via HDMI to the Analog-to-Digital Converter (ADC) card, the slave font-end board can only be connected to the master front-end board and thereby to the ADC card.
The ADC card digitizes the analogue APV25 signal. It is possible to connect a number of 8 HDMI cables to one ADC card. Due to the master slave system the signal of up to 16 APV25 chips can be digitized by one ADC card.
The Front-End Concentrator (FEC) card is the interface between the ADC card and the data acquisition computer. When the FEC card receives a trigger signal the APV25 chips are read out. The signals of the different APVs are synchronized by the FEC card before the signals is sent via an Ethernet cable to the data acquisition computer.

In this thesis all measurements were performed with resistive strip Micromegas detectors which were read out by APV25 chips and mostly by a single FEC card.

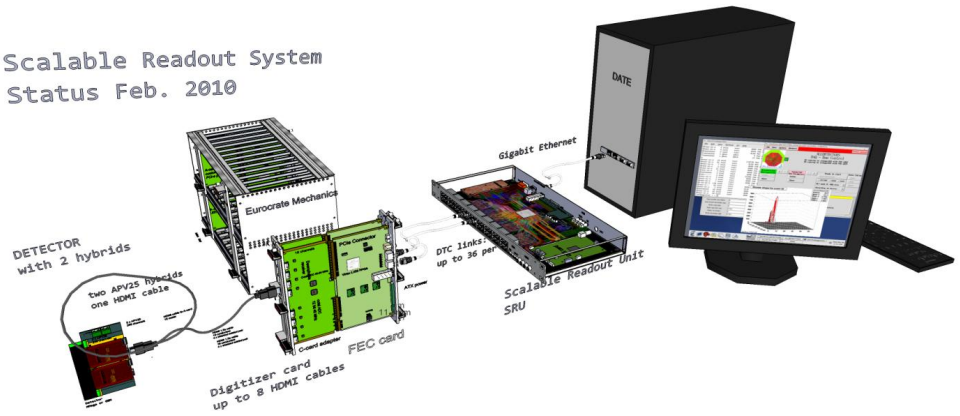

Figure 1.5: Schematic picture of the scalable readout system. Figure taken from [RD51-collaboration, 2010].
For the measurements in this thesis mostly no SRU is used. The FEC card is directly connected via Ethernet to the computer.

1.4 Motivation for the Multiplexing

Normally, for strip micromegas detectors every strip is read out by one single electronic readout channel. For small sized detectors with only a few hundred readout strips this is fine. In this case only a few APV25 front-end boards, FECs and ADC cards are needed.
In contrast to small sized Micromegas detectors large scale Micromegas detectors consist out of much more readout strips. For example a $2\,m^2$ large Micromegas detector (see figure 1.6), as it will be used for the end cap region of the ATLAS muon spectrometer, consists out of four layers of Micromegas detectors [Kawamoto et al., 2013]. Each layer has roughly 3000 readout strips. This leads to a demand of 96 APV25 front-end board chips, 6 ADC cards and 6 FEC cards to read out one module.
The large number of readout electronics for one module leads to a large amount of data, high power consumption, high heat dissipation and subsequently to high operation costs.
Due to the high acquisition costs for the readout electronics, the electronics is sufficient for only one SM2 module to be tested in the cosmic muon test stand in Munich. Respecting that only a small fraction of all readout channels carry a particle signal, a reduction of readout electronics is desirable.
One possibility to reduce the number of needed readout electronics is the so called generic multiplexing. Generic multiplexing is a readout method where multiple readout strips are mapped to one electronic readout channel in such a way that the signal can be fully reconstructed [Procureur et al., 2013].

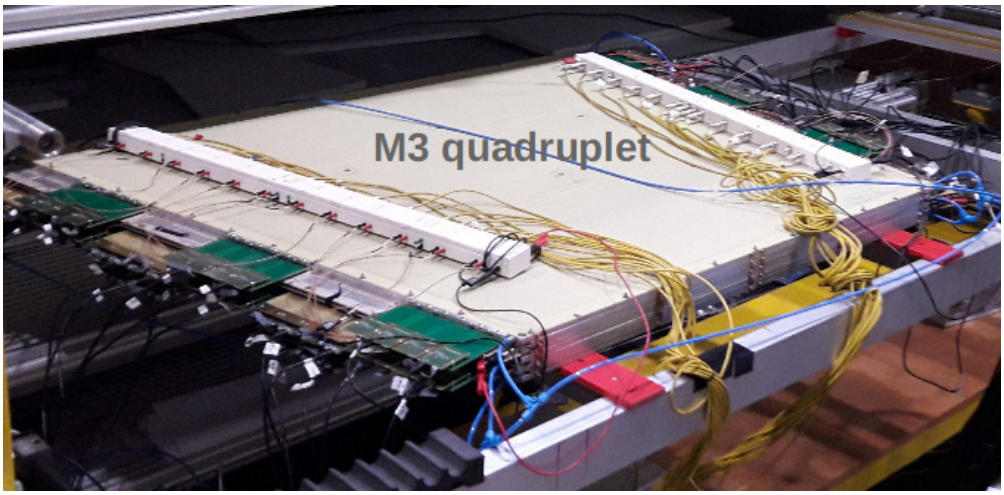

Figure 1.6: Picture of a $2\,m^2$ large SM2 detector equipped with 96 APV25 front-end boards.

Chapter 2

Signal Reconstruction Methods

A typical APV25 signal for a 20 MeV proton traversing a Micromegas detector is shown in figure 2.1. With a duration of a few hundred nano seconds, the APV signal is a fast signal. Therefore, among other things, the Micromegas detector is capable to deal with high rates. Due to the transverse diffusion of the electrons in the drift region a signal is detected on more than one strip. A group of responding strips is called cluster. Out of the signal shown in figure 2.1 a precise position where the particle traversed the detector can be reconstructed.

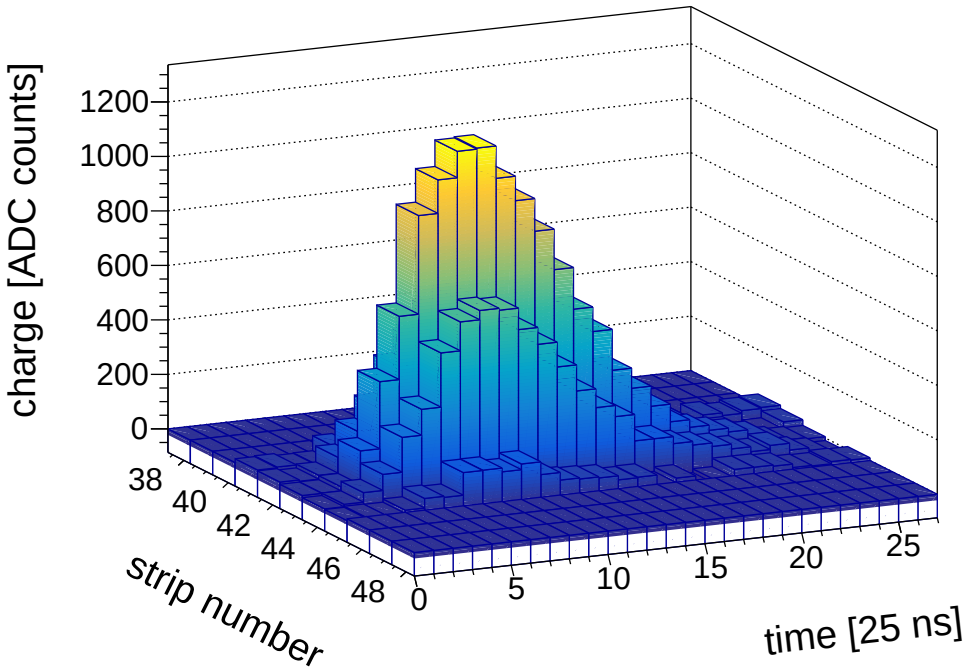

Figure 2.1: A typical APV25 signal for a 20 MeV proton traversing a Micromegas detector. A very fast charge rise and a rather slow charge decrease is clearly visible. Due to transverse diffusion of the electrons in the drift region, the signal is spread on a number of adjacent readout strips.

2.1 Hit Position Reconstruction Methods

Since the particle signal is mostly detected on more than one strip, a precise hit position can be reconstructed.
To obtain a precise time and charge information for each strip, the signal of each readout strip is fit with an inverse Fermi function (see figure 2.2):

$$q(t) = \frac{q_0}{1 + exp\left(\frac{t_0 - t}{\Delta t}\right)} + q_{offset} \tag{2.1}$$

The time at the point of inflection (t_0) is used as the signal time. The total charge which is collected on a strip is calculated as the difference between the maximum charge (q_0) and the charge offset of the APV25 (q_{offset}). In the following this difference is used as the strip charge. Δt is a measure for the signal rise time Iakovidis [2014].
It is possible that multiple clusters are reconstructed at an event in the detector. For the position and angle reconstruction the cluster with the highest charge sum (cluster charge) is used. For moderate particle fluxes this is most probable originating from a particle which traversed the detector.

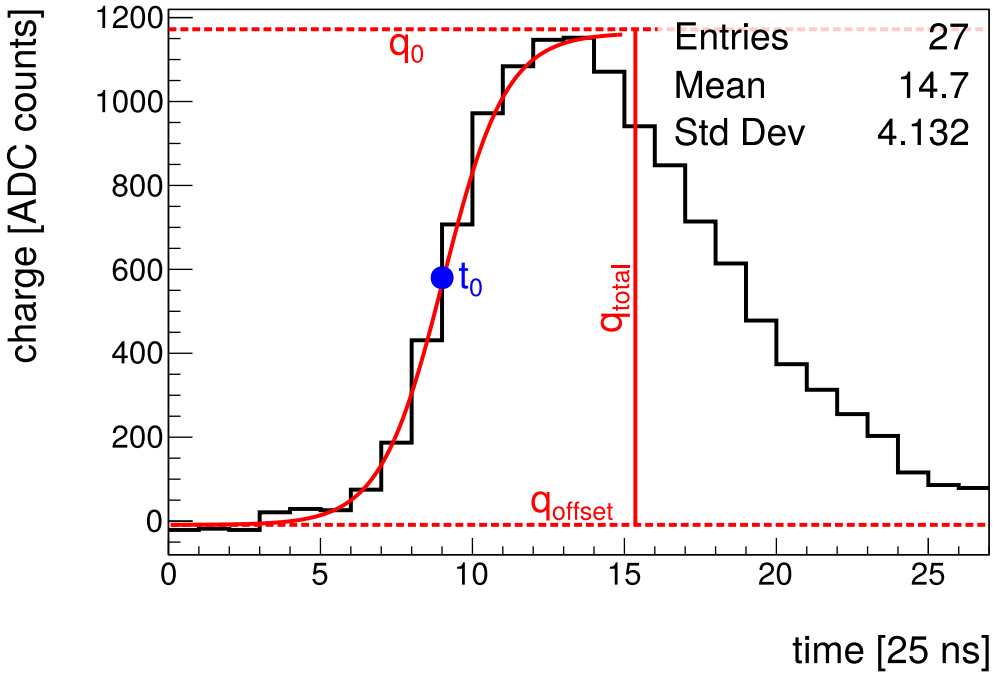

Figure 2.2: Typical APV25 signal of one single APV25 channel.
The signal originates from a 20 MeV proton traversing a Micromegas detector. The signal rise is fit with an inverse Fermi function (equation 2.1). The point of inflection (t_0) is used as the signal timing.

2.1.1 Centroid method

The charge for perpendicular tracks is Gaussian distributed on the readout strips (see figure 2.3). The charge weighted mean of this distribution can be taken as the particle position on the readout strips corresponding to the middle of the strip gap.
It can be calculated with equation 2.2.

$$x_{cen} = \frac{\sum\limits_{cluster} x_{strip} \cdot q_{strip}}{\sum\limits_{cluster} q_{strip}} \tag{2.2}$$

q_{strip} is the charge detected on the strip at the position x_{strip}.
In thin detectors, the ionization of the gas in the drift region along the particle path is inhomogeneous. For perpendicular tracks this can not be resolved in the charge distribution.
With an increasing angle of incidence the inhomogeneous ionization is resolved in the charge distribution on the readout strips (see figure 2.4). The Gaussian distribution vanishes. Therefore, there can be a mismatch between the charge weighted mean and the particle position referring to the middle of the drift gap.

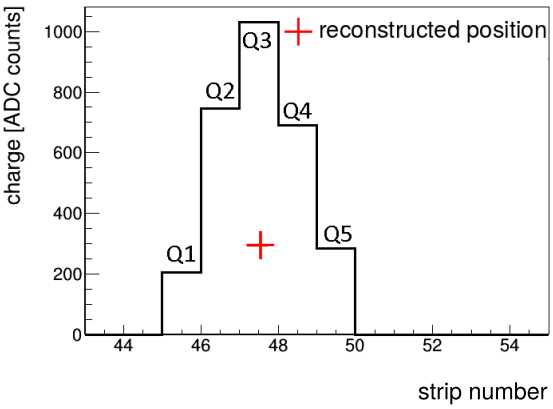

Figure 2.3: Charge distribution in a cluster of five strips for a perpendicular particle track.

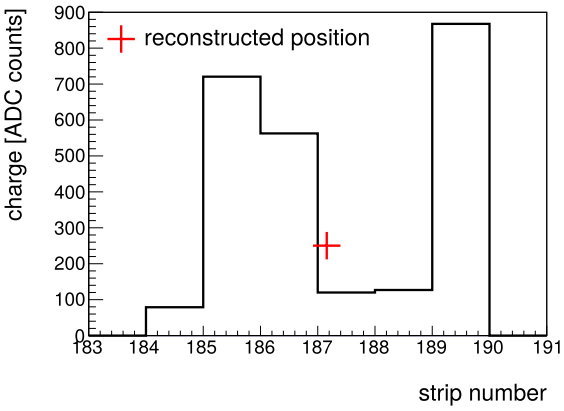

Figure 2.4: Charge distribution in a cluster of six strips for a ≈30° inclined particle track.

2.1.2 µTPC method

To reconstruct a precise particle position for inclined particle tracks, the drift time of the electrons in the drift region to the mesh is used. The reconstruction algorithm is similar to the one of a Time Projection Chamber (TPC), so this reconstruction method is called µTPC method [Iakovidis, 2014].
For the µTPC method the measured drift time of the electrons is used. Due to the longer drift distance, the signal of an electron created closer to the cathode is detected at a later time than the signal of an electron originating closer to the mesh (see figure 2.5). The exact track of the traversing particle can be reconstructed via the drift velocity as a proportional factor. The mean value of the drift velocity is constant. It is depending on the gas mixture and drift field ($\vec{E}_{\text{drift}}$).
The angle of inclination (Θ in figure 2.5) is calculated with:

$$\Theta = arctan\left(\frac{p}{slope_{track} \cdot v_{drift}}\right) \tag{2.3}$$

$slope_{\text{track}}$ is the slope of linear fit in the strip number against drift time spectrum (see figure 2.5). The drift velocity, v_{drift}, is generally known from simulations (see figure B.1 in the appendix), or can be extracted from the data [Bernhard, 2018]. p is the periodicity of the strips.
As for the centroid method (see chapter 2.1.1) the extrapolated position of the track at half of the drift space can be used as the reconstructed position.

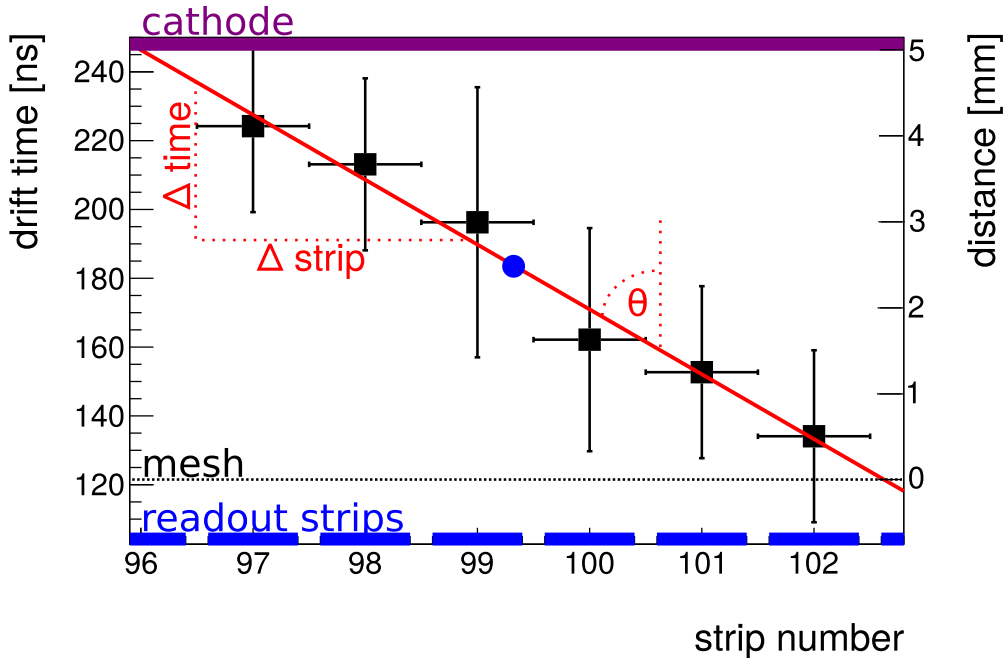

Figure 2.5: The signal timing is depending on the strip number for a particle traversing the detector under an incident angle, here: $\Theta = 20°$.
The timing is fit with a linear function. Using the drift velocity as a proportional factor, the particle track can be reconstructed.
For display reasons the cathode, mesh and readout strips of the detector are shown as well as the drift time data points. The proportionality between drift time, and distance is given by the drift velocity.

2.2 Signal Identification

To ensure that only channels which detected a signal are read out and used for the analysis an event selection is applied. During the data acquisition an online channel selection, which is called zero suppression is executed.

2.2.1 Zero Suppression

For this thesis most data were recorded with mmdaq [Byszewski, 2011]. Mmdaq is a software for data acquisition, using only one FEC card, which is directly connected to the data acquisition computer via Ethernet (see chapter 1.3).
Mmdaq processes the raw APV25 data and writes it to a root file. Only data of a hit strip is written to the root file. The signal of all other strips is rejected by the so called zero-suppression. It is executed after the charge offset (pedestal) for each APV25 is subtracted.

Due to electronic noise, every APV channel is continuously detecting signals with a low pulse height. The fluctuation of the pulse height of the readout channels, which did not detect a particle signal is observed. The variation of the pulse height (standard deviation) is a measure for the fraction of coupled noise.
The zero suppression selects the signal channels and discards the noise channels. For the zero suppression each strip is integrated over all time bins. If the Integral exceeds a threshold the signal is used (see figure 2.6) otherwise it is rejected. The standard deviation multiplied by the number of time bins is used as a threshold [RD51-collaboration, 2012].

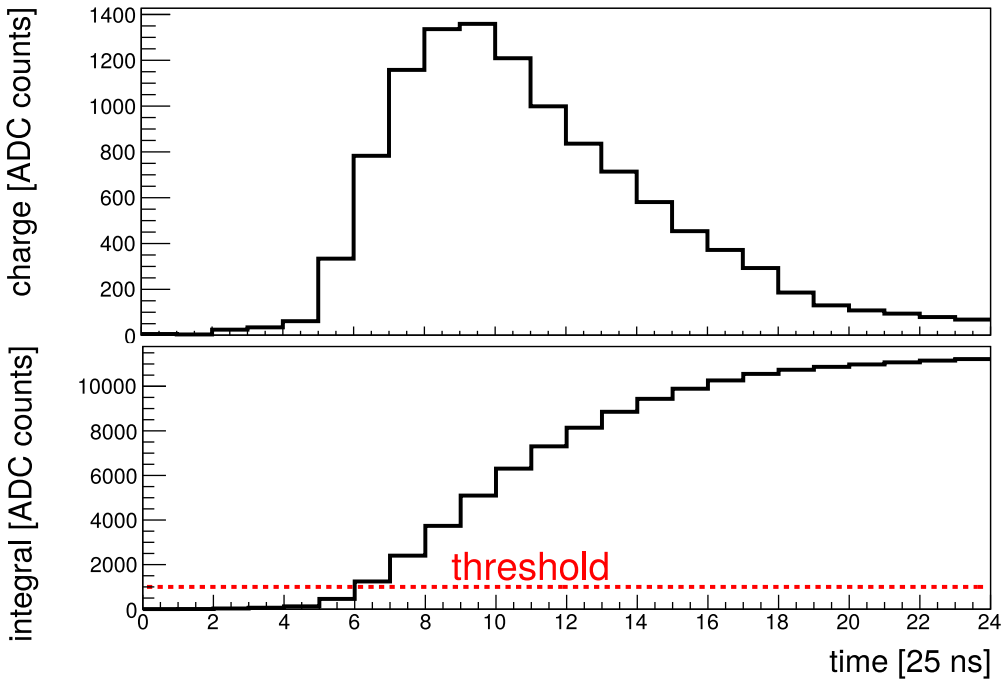

Figure 2.6: Top: Raw signal of one single APV25 channel. Bottom: Integral of the raw signal from the top.
For displaying reasons the threshold is shown at a much larger value as normally used (for the zero suppression it is at (20-60 ADC counts) . If the integral exceeds the threshold the raw pulse is taken as a signal.

2.2.2 Event Selection in the Analysis

Not all noise is canceled at the zero suppression. To filter out the remaining noise, only events are used where the fit with an inverse Fermi function showed satisfying results. Events with an unphysically large or small rise time (Δt in equation 2.1) are discarded (see figure 2.7).
Furthermore only events are taken into account with a ratio between the standard deviation of the strip charge and the maximum strip charge ($std.\ deviation_q/q_{max}$) in a certain range (see figure 2.8). If this ratio is close to one no signal is distinguishable from the fluctuations of the charge. If this ratio is too low a clear signal is only detected in few time bins. By applying these thresholds, the strip charge distribution becomes Landau shaped and the signal time is distributed more uniform (see figures 2.9 and 2.10).
The remaining strips are used for the signal position and angle reconstruction.

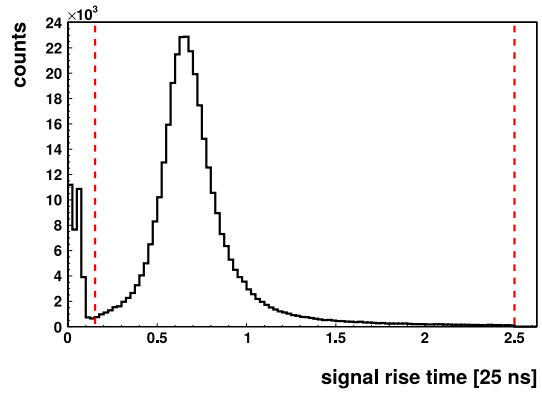

Figure 2.7: Signal rise time Δt from equation 2.1.
A cut will be applied at too fast (3.75 ns) and too slow (62.5 ns) rise times
50000 proton (20MeV) events are shown.

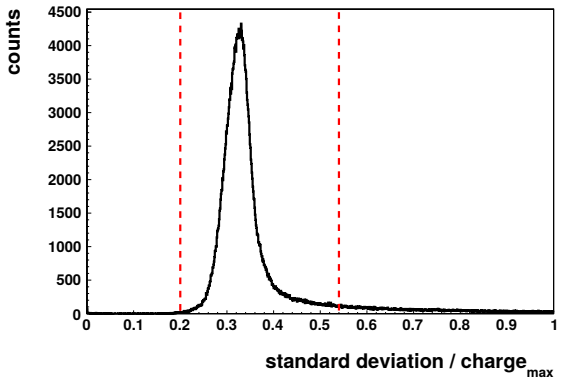

Figure 2.8: Ratio between the standard deviation of the strip charge and the maximum charge detected on this strip.
Ratios larger than 0.55 or smaller than 0.2 of the signal are rejected as noise.
50000 proton (20MeV) events are shown.

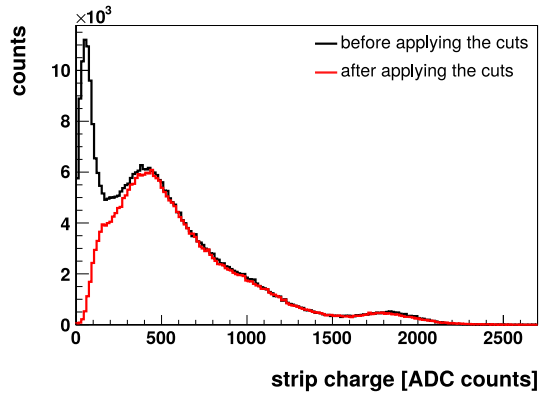

Figure 2.9: Strip charge distribution for 50000 20MeV proton events before and after application of the cuts shown in figure 2.7 and 2.8.
Noise signals at ≈ 100-200 ADC counts are rejected. The bump at ≈ 1800 ADC counts is due to saturation of the APV25 chip.

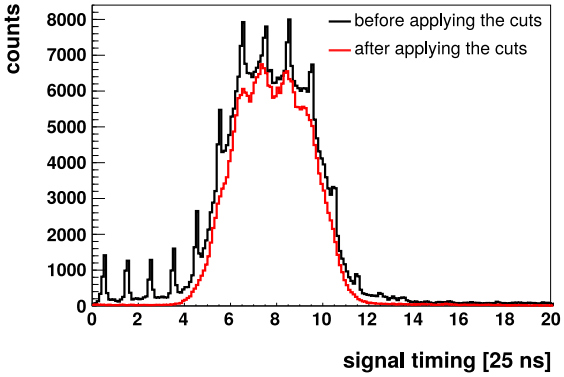

Figure 2.10: Signal timing distribution for 50000 20MeV proton events before and after application of the cuts shown in figure 2.7 and 2.8.

2.3 Capacitive Coupling Between Neighboring Strips

A fraction of the charge collected on a strip is transferred to the neighboring strips via capacitive coupling (see figure 2.11) due to the capacitance between the readout strips. Then again the neighboring strips couple to their adjacent strips. Depending on the readout strip length a fraction $\approx 23\,\% - 29\,\%$ is coupled to the adjacent strips [Lösel, 2017]. The mean of the charge distribution stays the same due to the symmetry of the capacitive coupling. Therefore the centroid position is hardly affected by the capacitive coupling. Since the signal timing is extracted from the charge signal of the APV, the reconstruction with the µTPC method is influenced by the capacitive coupling.
Since the APV25 raw signal is a time dependent charge distribution (see figure 2.1) a charge correction can be applied separately for each time bin. Assuming a charge deposit Q on one strip and a measured charge q_0 on this strip, a factor $r_0 \times q_0$ has to be subtracted from the two adjacent strips. By adding the subtracted charge to the original strip one obtains the charge $Q = (q_0)_{\text{corrected}}$.

$$\begin{aligned} (q_0)_{corrected} &= q_0 + 2r_0 \times q_0 \\ (q_{\pm 1})_{corrected} &= q_{\pm 1} - r_0 \times q_0 \end{aligned} \tag{2.4}$$

Since the neighboring strips then again couple to their neighboring strips this correction has to be applied to the next but one and next but two strips, though with a correction factor $r_{\text{n}} = (r_0)^n$ for the "next but n" neighboring strip. This charge correction is applied time bin wise for each readout strip.

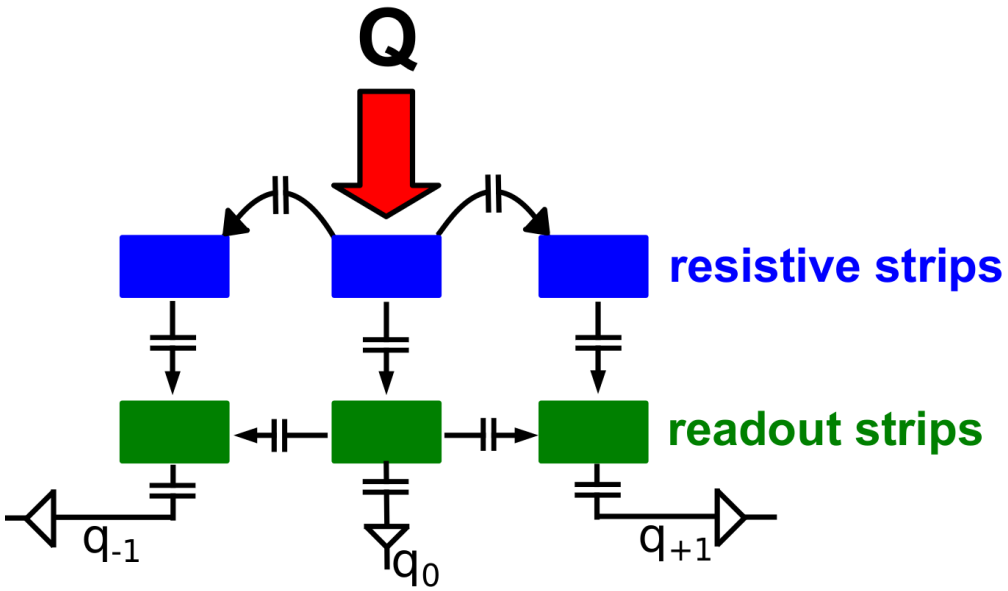

Figure 2.11: Capacitive coupling between neighboring strips of a resistive strip Micromegas (taken from [Lösel, 2017]).
A fraction of the charge Q collected on the middle resistive strip is capacitively coupled to the neighboring strips. The signal also couples to the readout strips as intended. Then again charge is capacitively coupled between the readout strips.

Chapter 3

Multiplexing

For a multiplexed readout multiple detector strips are connected to one channel of the readout chip. The mapping between the readout strips and the channels has to be performed in such a way that the detector properties are hardly influenced. In particular the fine detector resolution and efficiency should remain unchanged. Additionally the number of ambiguities for the reconstructed particle position should be limited [Procureur et al., 2013].
In the following the development of a multiplexed readout for Micromegas detectors is presented.

3.1 Working Principle of the Multiplexing

By connecting multiple readout strips and mapping it to one readout channel some information is lost. Initially it is not evident at which of the connected strips the particle traversed the detector. Ambiguities of the particle position can occur (see figure 3.1). To maintain the efficiency some redundant information has to be found to compensate the information loss.

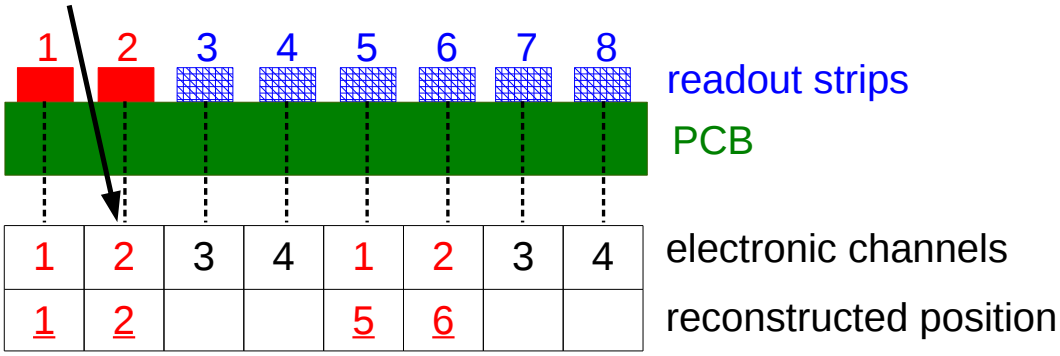

Figure 3.1: Information loss due to multiplexing. The electronic channels are mapped to the readout strips without mapping rules.
Assuming a traversing particle (↘) is creating a signal on the first two strips (indicated in red). Since the electronic channels which detected a signal ($\{1, 2\}$) are connected to a number of strips the particle position is ambiguously located at the strips $\{1, 2, 5, 6\}$.

3.1.1 Double Sided Multiplexing

A smart way to compensate the loss of information is to add a second layer of wider readout strips. The signal couples from the thinner readout strips to the wider readout strips. The

wider readout strips restrict the particle position to several thinner readout strips (see figure 3.2). With that additional information the signal can be reconstructed to a unique position [Procureur et al., 2013]. However, the electronic noise increases and the signal pulse height decreases.
Since the detector design has to be modified for this kind of multiplexing it can not be used for existing detectors. Therefore the double sided multiplexing is not discussed in detail in this thesis.

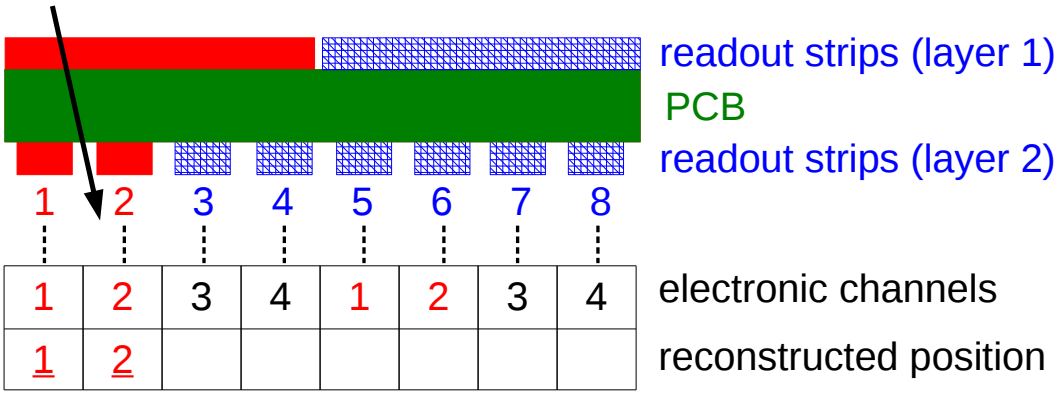

Figure 3.2: Working principle of the double sided multiplexing.
By adding a layer of wider readout strips the hit position can be restricted to several readout strips of the second layer. A signal of a traversing particle (↘) is detected on the first two strips in layer two (indicated in red). Knowing a rough position from readout strips in layer one the signal can be clearly reconstructed to the readout strips $\{\underline{1}, \underline{2}\}$.

3.1.2 Generic Multiplexing

With the knowledge that a traversing particle leaves a signal on multiple neighboring strips (see chapter 2) a redundant information already exists. This can be used to compensate the loss of information which leads to ambiguities of the particle position. For the SM2 detector (see chapter 5.1.2) with a strip periodicity of $p = 0.425\,\text{mm}$ this holds true for almost all events (see figures 3.3 and 3.4). By changing $\vec{E}_{\text{drift}}$ the transverse diffusion of the electrons in the drift region is affected and thus the number of hit strips is changed. Therefore the requirement of more than one hit strip in an event can be fulfilled by, either changing $|\,\vec{E}_{\text{drift}}\,|$ or lowering the strip pitch [Procureur et al., 2013]. The second one is not possible for a given detector design. Also, using an arbitrary small $|\,\vec{E}_{\text{drift}}\,|$ is not possible. $|\,\vec{E}_{\text{drift}}\,|$ has to be large enough to prevent the electrons and ions in the drift region from recombination. Furthermore, if drift velocity gets too small, the large drift time causes troubles in the readout electronics.
A solution to resolve these requirements is the generic multiplexing. The working principle of the generic multiplexing is shown in figure 3.5. Assuming to have a signal on two adjacent strips s_{i} and $s_{\text{i+1}}$, which are connected to the electronic channels ch_{a} and ch_{b}, the obtained information from the electronics is a signal on the electronic channels ch_{a} and ch_{b}. Since channels ch_{a} and ch_{b} are also connected to multiple other strips (e.g. $s_{\text{i-5}}$ and $s_{\text{i+3}}$) there is an ambiguity in the particle hit position. However, the particle can exactly be localized to strips s_{i} and $s_{\text{i+1}}$ with the additional information of having a signal on at least two neighboring strips. This principle can be generalized for signals on more than two neighboring strips [Procureur et al., 2013].

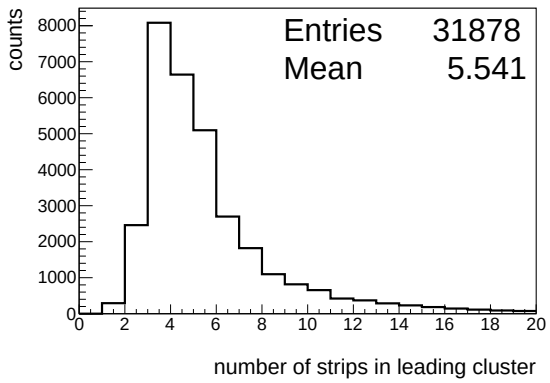

Figure 3.3: Number of strips in the signal cluster of the SM2 detector.
The detector is operated with $U_{\text{amp}} = 570\,\text{V}$ and $U_{\text{drift}} = 300\,\text{V}$. It is flushed with $\text{Ar} : \text{CO}_2$ 93 : 7 vol. %. The data were taken with 120 GeV pions (minimal ionizing particle), perpendicularly traversing the detector.

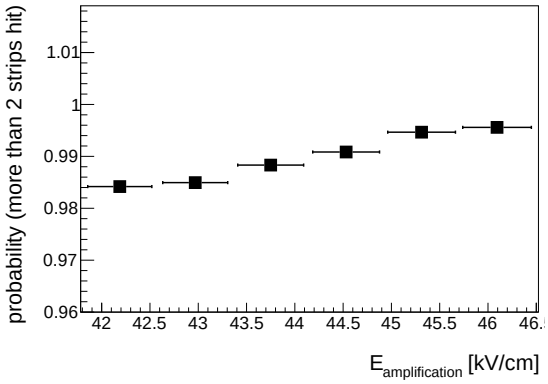

Figure 3.4: Probability of signal clusters larger than two strips in dependence of the amplification field.
A signal is detected on more than two strips in almost all events (requiring the detector is hit at all). The detector is operated with $U_{\text{drift}} = 300\,\text{V}$. The data were taken with 120 GeV pions (minimum ionizing particle), perpendicularly traversing the detector.

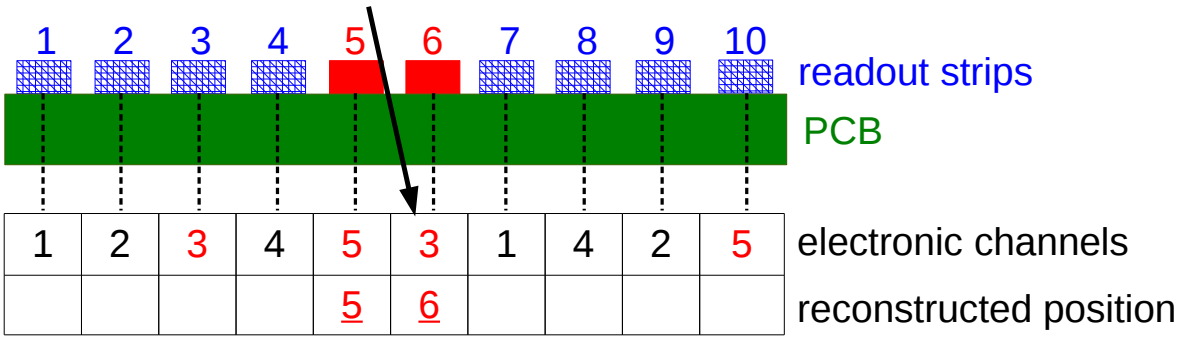

Figure 3.5: Working principle of the generic multiplexing.
The signal of a particle traversing the detector (↘) at the fifths and sixths strip is detected on the electronic channels $\{3, 5\}$. Since a traversing particle is mostly creating a signal on a number of neighboring strips, the signal position can be localized to the strips $\{\underline{5}, \underline{6}\}$. These are the only neighboring strips connected to the channels $\{3, 5\}$.

3.1.3 Mapping for the Generic Multiplexing

To be capable to reconstruct a clear particle position the mapping for the generic multiplexing has to fulfill two rules [Procureur et al., 2013]:

- Consecutive strips must not be mapped to the same channel number. This has the same effect as enlarging the pitch of readout strips (see figure 3.6). Thus the spatial resolution of the detector decreases.
- Every cluster of channels mapped to consecutive strips is allowed to appear at most once. Otherwise an ambiguity of the reconstructed particle position occurs (see figure 3.7).

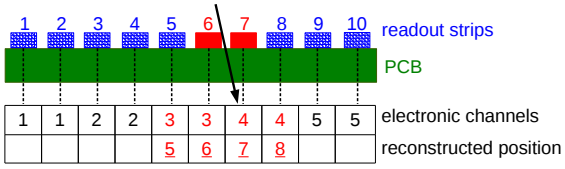

Figure 3.6: Mapping of neighboring strips to the same electronic channel number.
The strips $\{6, 7\}$ respectively the electronic channels $\{3, 4\}$ detect a signal of the traversing particle. Since strips $\{8, 5\}$ are also connected to the same channels as strips $\{6, 7\}$ the reconstructed hit position $\{5, 6, 7, 8\}$ is larger than the true hit position $\{6, 7\}$.

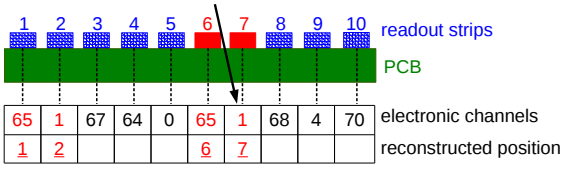

Figure 3.7: Mapping of the same cluster of channels to consecutive strips multiple times.
The strips $\{6, 7\}$ respectively the electronic channels $\{65, 1\}$ detect a signal of the traversing particle. Since the channels $\{65, 1\}$ are also connected to the neighboring strips $\{1, 2\}$ there are two possibilities for these channels to be mapped to consecutive strips. An ambiguity of the hit position occurs ($\{1, 2\}$ and $\{6, 7\}$).

Fulfilling these rules a clear hit position reconstruction for single particle events is possible. A total number of $n_{\max}$ strips can theoretically be read out by a number of p electronic channels [Procureur et al., 2013]:

$$n_{max} = \frac{p!}{k!\,(p-k)!} + (k-1) \tag{3.1}$$

k is the minimal number of consecutive strips which collect a signal of a traversing particle. For instance, if a minimal number of two consecutive signal strips is hit ($k = 2$), a number of $n_{\max} = 8128$ readout strips can be mapped to $p = 128$ electronic channels.
Though it is not desirable to connect a number of $n_{\max}$ strips to p electronic channels. For instance when a number of particles are traversing the detector simultaneously, ambiguous reconstructed particle positions are possible (see figure 3.8). The more readout strips are connected to one electronic channel, the higher the probability gets for ambiguous events. However by using other information like the signal timing (see chapter 2) multi particle events can be identified as such. Ambiguities can be suppressed (see figure 3.9) [Procureur et al., 2013].

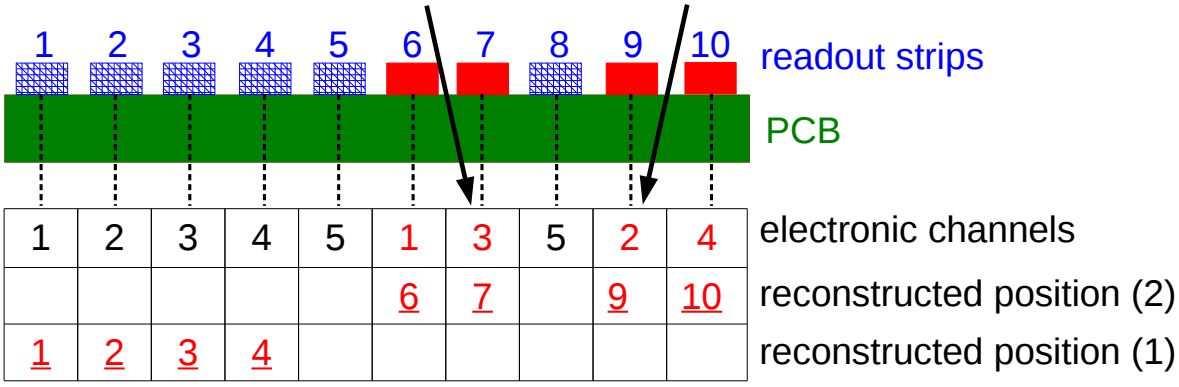

Figure 3.8: Ambiguities due to a number of particles traversing the detector.
The strips $\{6, 7\}$ and $\{9, 10\}$ respectively the electronic channels $\{1, 3\}$ and $\{2, 4\}$ detect a signal of two traversing particles. Since the electronic signal channels are also connected to the adjacent strips $\{1, 2, 3, 4\}$ the signal can also originate from one single particle traversing at this position.

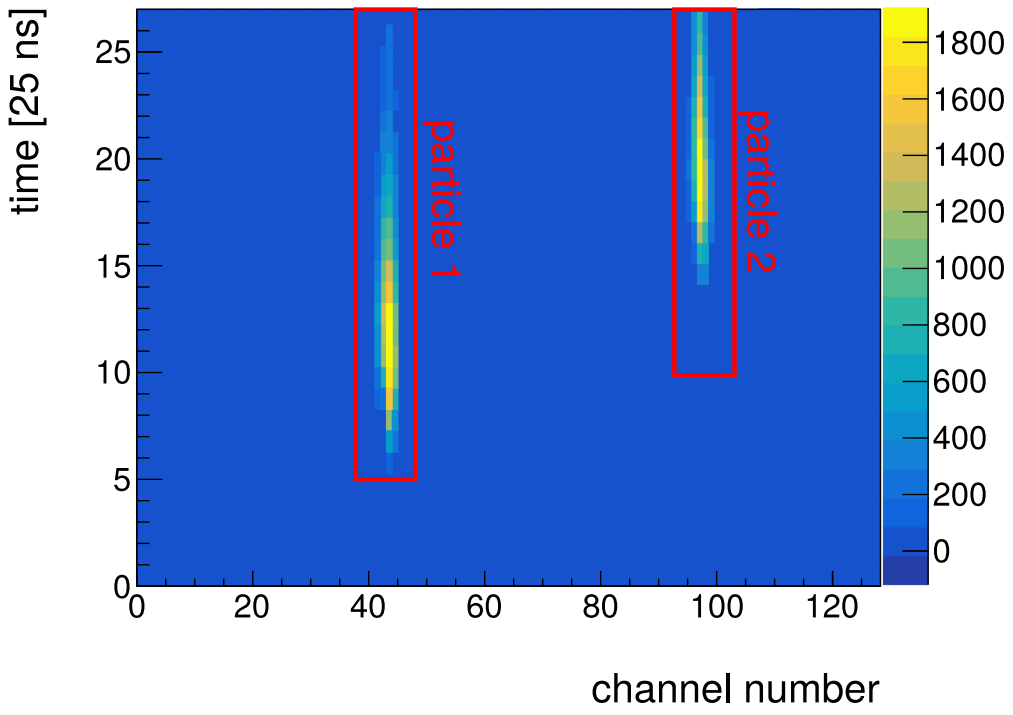

Figure 3.9: Raw signal of two particles traversing the detector during one event. With the time information one can identify the two particles.
Particle 1 traversed the detector earlier ($t_1 \approx 125\,\text{ns} - 550\,\text{ns}$) as particle 2 ($t_2 \approx 375\,\text{ns} - 625\,\text{ns}$).

3.2 Disadvantages of the Generic Multiplexing

Theoretically $n_{\max}$ strips can be connected to one electronic channel (see equation 3.1). However this number is limited even for single particle events since the signal to noise ratio (S/N ratio) as well as the extracted signal pulse height decreases with increasing n [Procureur et al., 2013].

3.2.1 Decrease of Detected Signal Pulse Height

By applying a multiplexed readout a decrease of the signal pulse height, which is decoupled from the readout strips, is expected. The charge which can be extracted from the readout strips is depending on the capacitance C_{det} which is connected to one electronic channel. For a multiplexed readout C_{det} is higher compared to a non-multiplexed readout.
For the investigation of the multiplexed Micromegas readout an APV25 readout chip is used. In the Laplace space it has an input impedance $Z_{\text{in}}(s)$, where s is defined as $s = \sigma + i\omega$. ω is the signal frequency. For a typical Micromegas readout (see figure 3.10), the signal current ($I_{\text{in}}(s)$) which is extracted by the readout electronics calculates as [Blum et al., 2008]:

$$I_{in}(s) = \frac{1}{1 + s\tau} I_{ind}(s) \quad \tau = R_{in} C_{det} \tag{3.2}$$

I_{ind} is the current on the readout strip. $R_{\text{in}} = \Re(Z_{\text{in}})$ is fixed by the chip design. Therefore the extracted signal is depending on C_{det}.
By coupling a number of readout strips to one electronic channel, C_{det} increases and therefore the charge which is decoupled from the strips decreases. For instance, C_{det} doubles by coupling two readout strips to one electronic channel. Therefore the extracted signal current $I_{\text{in}}(s)$ decreases by a factor of up to 0.5.
If the decoupled charge gets too low, it is possible that strip signals are not detected as such any more. Too small signals are more likely to be lost at the zero suppression (see chapter 2.2.1).

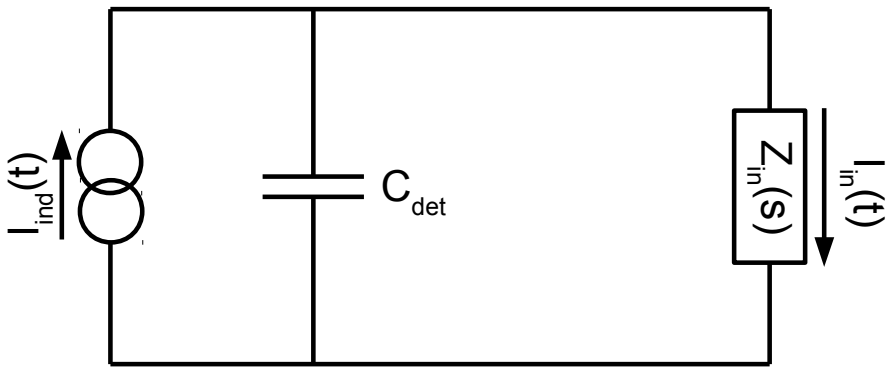

Figure 3.10: Input circuit for a typical strip readout channel according to [Blum et al., 2008].
For an induced signal current $I_{\text{ind}}(t)$ a current $I_{\text{in}}(t)$ is extracted by the readout chip. C_{det} is the capacitance of all strips coupled to one electronic channel with the impedance $Z_{\text{in}}(s)$.

3.2.2 Increase of Detected Noise Signals

With an increasing capacity due to the connection of a number of readout strips, external noise is more likely coupled on to the detector strips.
The readout strips behave like antennas for electromagnetic signals. This coupled noise is visible in the measurements. As it is measured in [Lösel, 2017], the fraction of noise coupled on to a readout strip increases with an increasing capacitance. The pulse height fluctuations (sigma) increase (see chapter 2.2.1). Therefore a higher threshold is taken to identify signals at the zero suppression. Consequently lower particle signals are wrongly identified as noise and therefore eliminated by the zero suppression.

Chapter 4

Development of a Multiplexing Adapter Board for APV25 Front-End Electronics

The multiplexed readout, developed for this thesis, should be applied to already existing detectors. Therefore, the multiplexed mapping can not directly be implemented on the readout PCB of the detector. The mapping is executed on an adapter board. It connects the readout strips on one side, and the APV25 front-end board on the other side of the adapter board in a generic multiplexed way.

4.1 Mapping for the Multiplexing Adapter Board

Due to development reasons and the expected decrease of the pulse height (see chapter 3.2.1) a multiplexing scheme is developed, which reduces the electronic channels by a factor of two. Since an APV25 has 128 channels, 256 strips are mapped to one APV25.
By iteratively trying out a mapping is developed, which fulfilled the rules presented in chapter 3.1.3. However, the mapping rules only consider the ideal case, where every strip and channel is working properly. In reality it is possible that single electronic channels do not detect a signal when the connected strip is hit (dead channels), or respectively detect a signal continuously even when the strip is not hit (noisy channels). In both cases the mapping rules still have to be fulfilled. The developed mapping is considering dead and noisy channels. It is shown in the appendix in table A.1.
A sketch of the adapter board is shown in figure 4.1. The first 128 strips are mapped in the same way as for a normal readout. The first strip is mapped to the first channel, the second strip to the second channel and so on (see table 4.1). The signal of a particle traversing the detector at the first 128 strips results in one single signal cluster of electronic channels (see figure 4.3). In the following this region is called "one to one mapped region".
The second 128 strips are mapped in such a way, that the electronic channels of neighboring strips are mostly 63 – 67 APV channels[1] apart (see table 4.2). In this thesis this region is called "multiplexed region". Two signal clusters in the electronics are expected for a particle traversing between strip 129 and 256 (see figure 4.4).
In the case the signal strip cluster is located in the "transition region"between the multiplexed and the "one to one mapped region" it is possible that the signal is split to three clusters of electronic channels. One electronic cluster originates from the signal part in the "one to one

[1]Every eight strips neighboring strips are only three electronic channels apart (see figure 4.19).

mapped region" whereas the second and third cluster originate from the signal part in the "multiplexed region".

The PCB of the adapter board, which performs the previously explained mapping is shown in figure 4.2. The adapter board is mapping two times 256 readout strips to two APV25 front-end boards[2]. The adapter board can be connected via Zebra connectors to the Micromegas detector. Via a 130 pin Panasonic connector it can be connected to the APV25 front-end board.

[2]The previous explained mapping is performed two times on the adapter board. The electronics is reduced by a factor of two

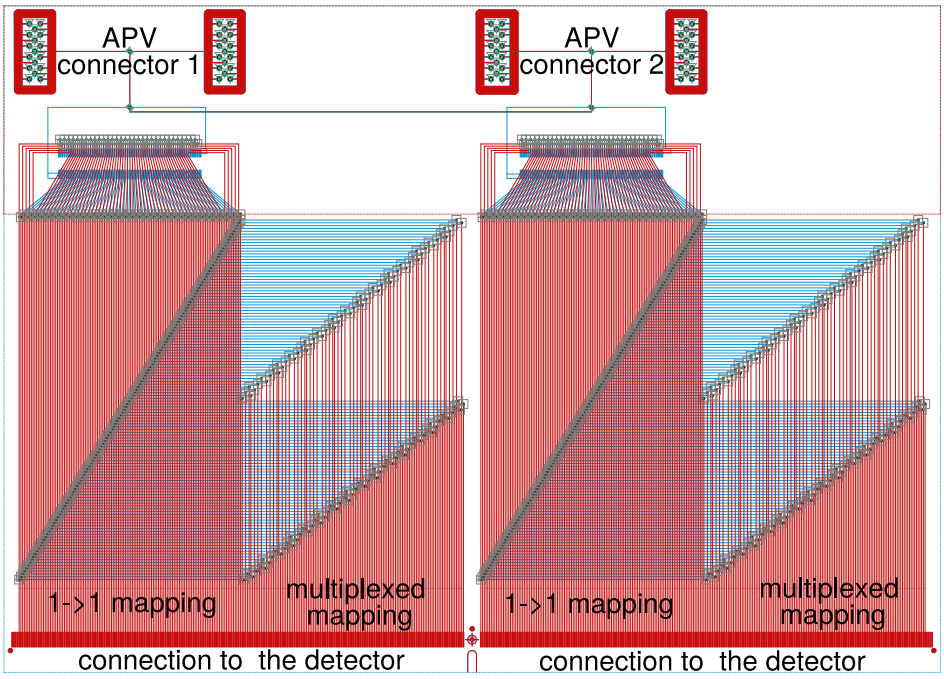

Figure 4.1: Sketch of the multiplexing adapter board.
It connects 512 readout strips (bottom) to two APV25 front-end boards (top). It can be clearly distinguished between the "one to one mapped region" and the "multiplexed region".

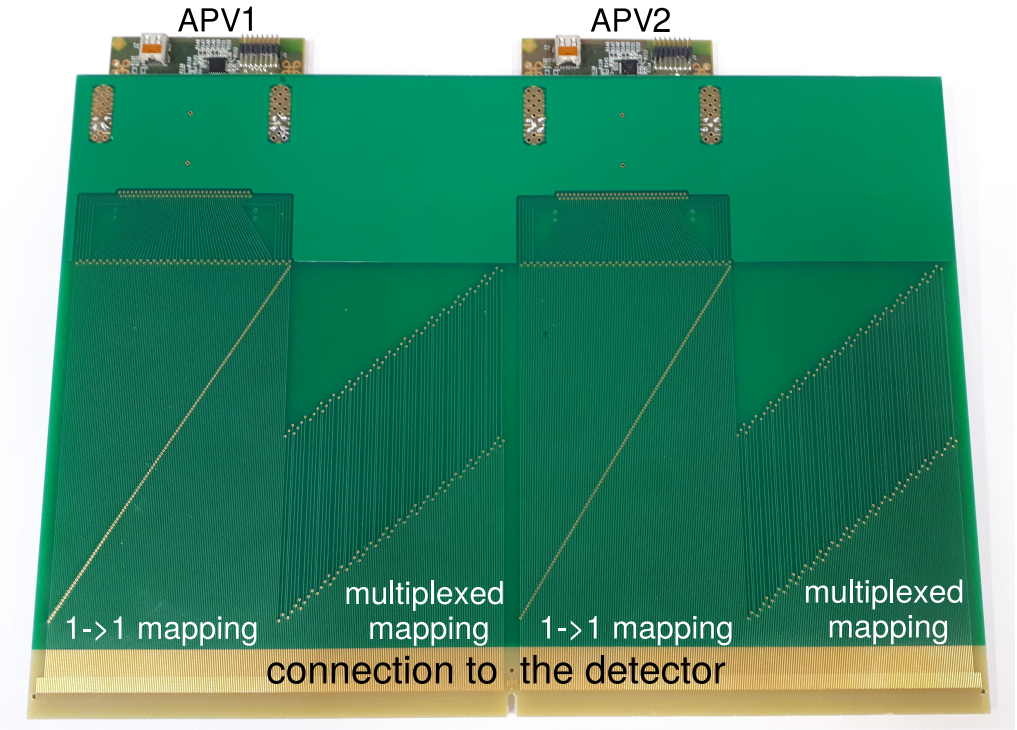

Figure 4.2: Multiplexing adapter PCB.
It connects 512 readout strips (bottom) to two APV25 front-end boards (top). It can be clearly distinguished between the "one to one mapped region" and the "multiplexed region".

Table 4.1: Section from the mapping of the first 128 strips.
The strips are mapped like for a non-multiplexed readout.

strip number	1	...	50	51	52	53	54	...	128
channel number	0	...	49	50	51	52	53	...	127

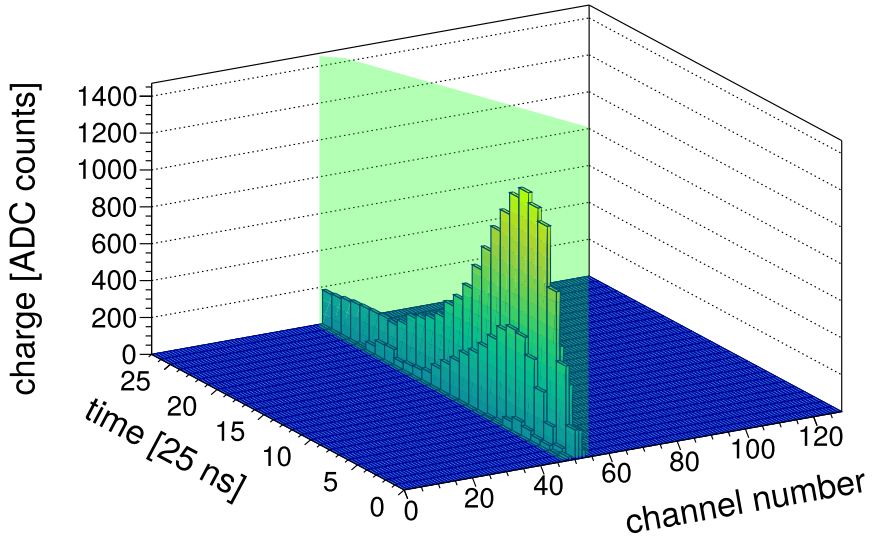

Figure 4.3: APV raw signal of a particle traversing the detector in the "one to one mapped region". Since neighboring strips are also neighboring APV channels, one signal cluster of electronic channels is detected. The shown cluster is the same as in table 4.1.

Table 4.2: Section from the mapping of the second 128 strips.
Neighboring strips are connected to channels which are mostly 63 – 67 channels apart.

strip number	...	129	...	154	155	156	157	158	159	...	256
channel number	...	65	...	78	14	11	77	13	79	...	255

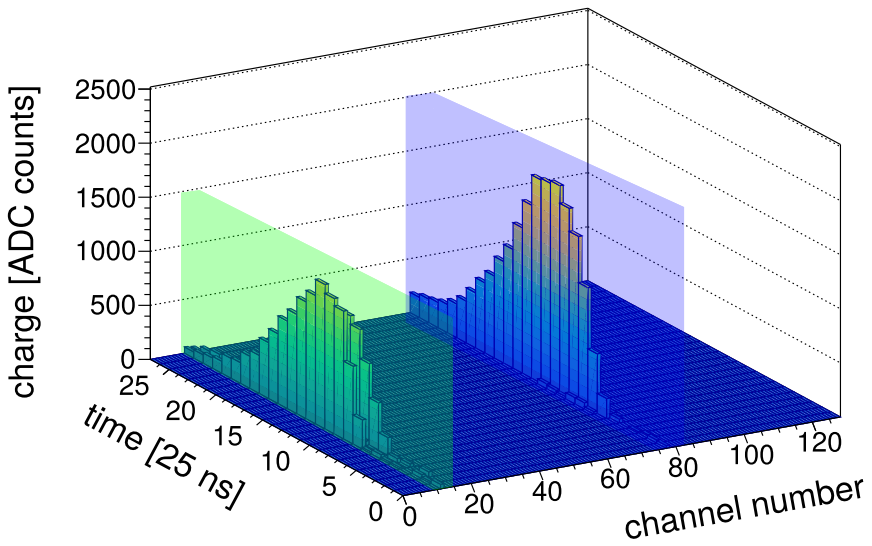

Figure 4.4: APV raw signal of a particle traversing the detector in the "multiplexed region". Since neighboring strips are mostly 63–67 strips apart, two signal clusters of electronic channels are detected. The shown clusters are the same as in table 4.2.

4.2 Signal Identification and Reconstruction

The strip charges of the signal shown in figure 4.3 can be seen in figure 4.5 (respectively for figure 4.4 in figure 4.6). It consists out of one to three clusters. In this case a cluster is defined as a number of adjacent electronic channels, which detected a signal. Due to the multiplexed mapping a gap of two electronic channels is possible. This needs to be taken into account for the cluster reconstruction.
A hit in the "one to one mapped region" (figure 4.3) is identified as such by detecting exactly one single cluster. To reconstruct the corresponding strip number just a fixed offset has to be added to the channel number.
By the detection of exactly two electronic clusters a hit in the "multiplexed region" is indicated (figure 4.6). The strip cluster can be reconstructed by looking up the strip number corresponding to the channel number.
If two or three clusters are detected and one contains channel 127 (respectively channel 0), the "transition region"is hit. The cluster which contains channel 127 respectively channel 0) corresponds to the "one to one mapped region". The other clusters belongs to the "multiplexed region" (see figure 4.9). These two clusters are reconstructed like a hit in the "multiplexed region".

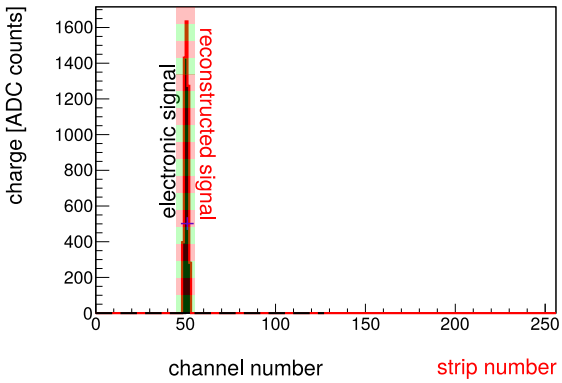

Figure 4.5: Signal of a single particle traversing the detector in the "one to one mapped region" The shown cluster belongs to the channels shown in table 4.2.

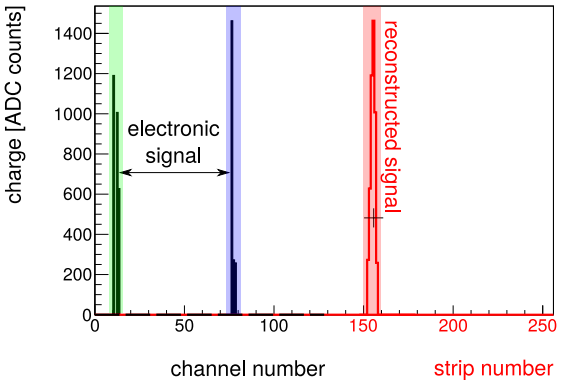

Figure 4.6: Signal of a single particle traversing the detector in the "multiplexed region" The shown clusters belong to the channels shown in table 4.2.

4.3 Noise Canceling

This demultiplexing procedure, as described before, only works for an ideal signal, which consists of a signal of one single particle without any noisy or dead channels. Whereas a second cluster, originating from noise, can wrongly associate a signal originating from the "one to one mapped region" to the "multiplexed region", dead or missing channels can lead to an extinction of the second electronic cluster of a signal in the "multiplexed region". Thus this signal is wrongly localized to the "one to one mapped region".
Therefore one of the main challenges for the signal reconstruction is to find the right balance between noise identification and dead channel identification. To ensure that no signal strips are rejected due to failing signal fits (see chapter 2.1) the previously explained noise canceling (see chapter 2.2.2) is executed only afterwards the demultiplexing procedure. To ensure the demultiplexing is hardly affected by noise signals, an event selection, which is independent of the signal fit, is executed.
If the charge of a channel is below a certain threshold, the signal of that channel is discarded. The threshold is depending on the mean charge collected by all electronic channels. This filters out noisy channels with a collected charge relatively low compared to the particle signal (see figure 4.7). The charge threshold level must not be set to too high values since in this case parts of the particle signal get discarded, though if it is set too low, the demultiplexing is influenced by the noise.
After applying the charge threshold, the position of the remaining electronic signals is considered. By construction of the adapter board, the distance of 63–67 APV channels between neighboring strips is given. The electronic channel cluster with the highest cluster charge is assumed to be a signal cluster. Only the region of electronic channels within a distance of 63–67 APV channels from the first cluster is taken into consideration to contain a signal cluster. Every strip which is not within the two selected clusters is discarded as noise (see figure 4.8).
The only exception for allowing more than two clusters in the electronic channels is, if the "transition region"is hit (see figure 4.9). In this case three electronic clusters are detected. Only the electronic clusters located near channels $ch = 0$, $ch = 63$, and $ch = 127$ are particle signal clusters. All other signals are discarded as noise. The noise canceling in this case needs to be applied with care. The electronic cluster sizes in the multiplexed region are smaller than in the case of non transition region hits located in the "multiplexed region" only. As it is shown in figure 4.9, it is possible that one of the three electronic signal clusters just consists out of one strip. Identifying one of the signal channels as noise leads to a wrong reconstructed strip position and thus to a bad resolution in the transition region.

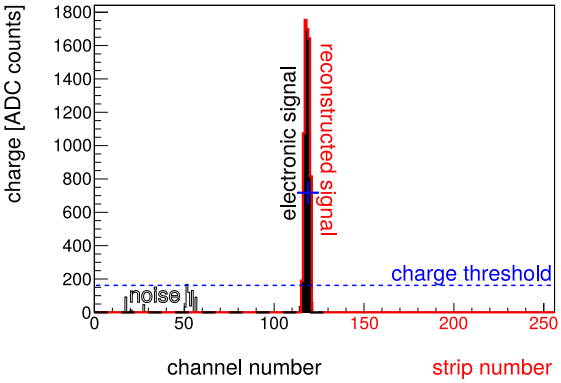

Figure 4.7: Signal of a particle traversing the detector in the "one to one mapped region".
Due to a charge threshold strips with a relatively low charge compared to the maximum strip charge are rejected as noise. Only one electronic cluster remains. The strip position can be reconstructed in the "one to one mapped region".

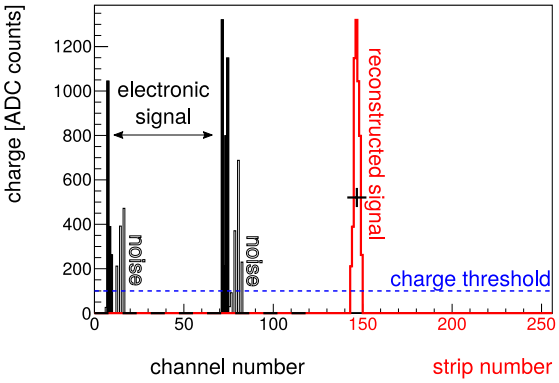

Figure 4.8: Signal of a particle traversing the detector in the "multiplexed region".
Only the two electronic clusters with the highest charge are used as signal clusters. All the other clusters are discarded as noise or second particle signals. The strip position can be reconstructed in the "multiplexed region".

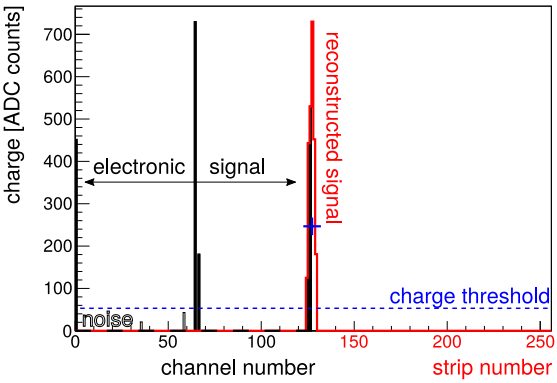

Figure 4.9: Signal of a particle traversing the detector in the transition region.
This is the only case where three cluster are allowed. In this example the electronic channels $\{1, 65, 67, 125, 126, 127\}$ are hit. All of these electronic clusters have to have a distance between 63 – 67 strips to the next cluster. All the other clusters are discarded as noise. The strip position can be reconstructed in the "transition region".

4.4 Capacitive Coupling due to the Multiplexing

Capacitive coupling for a non-multiplexed readout were already explained in chapter 2.3. However, with the multiplexed readout it is not that straight forward anymore. Adjacent strips are not adjacent channels anymore. Furthermore, coupling between neighboring strip lines on the adapter board can occur. However, the coupling on the board can be neglected if the capacitances of the readout strips are much larger than the capacitances of the board lines. All couplings to the neighboring strips, respectively neighboring strip lines on the adapter board, are shown in figure 4.10.
All the readout strips and lines on the adapter board are made out of copper. The signal collected on strip a spreads almost simultaneously over all readout strips and strip lines on the adapter board, which are connected to one electronic channel. Therefore, the signal couples to the neighboring strips $\{a_{-1}; a_{+1}\}$ of the readout strip a, where the signal is initially collected (see example in figure 4.10). It couples as well to the neighboring strips $\{b_{-1}; b_{+1}\}$ of strip b, which is also connected to the same electronic channel (see figure 4.10). Since neighboring strips in the "multiplexed region" are 63–67 electronic channels apart from each other, the signal is also collected on strips $\{c_{-1}; c_{+1}\}$, which are connected to the same electronic channels as the strips $\{b_{-1}; b_{+1}\}$. These strips are not connected to the neighboring strips of the initial signal strip a.
For the signal of a particle traversing the detector in the "one to one mapped region" this results in the existence of a second cluster 63–67 channels apart from the original cluster (see figure 4.11). By dividing the charge of the coupled cluster by the charge of the signal cluster, a rough coupling ratio is calculated (see figure 4.12). The second cluster is in the proper distance that the signal is wrongly identified as the signal of a particle traversing the detector in the "multiplexed region". In this case, the second cluster can be neglected by a high enough charge threshold. Though this can only be applied if the hit position is restricted to the "one to one mapped region". For a 20 MeV proton beam the Gaussian beam profile is nicely reconstructed for different amplification voltages (see figures 4.13 and figure 4.14). With increasing amplification voltage the frequency of wrongly reconstructed positions increases slightly (see figure 4.14).
For the signal of a particle traversing the detector in the "multiplexed region", the coupling to non-neighboring strips results in the existence of an additional cluster of electronic channels as well. Unfortunately, the capacitively coupled cluster is in a distance of 63–67 channels from the signal cluster. Hence it superimposes with the position of the other electronic signal cluster. Therefore, the coupling is not as clearly visible in an single event as for a signal in the "one to one mapped region". The effects of the charge coupling can be seen in the reconstruction of the hit position. Whereas a smooth Gaussian beam profile can be reconstructed for smaller amplification voltages (figure 4.15), periodic spikes in the beam profile occur for higher amplification voltages (figure 4.16). The distance of the spikes (eight channels) fits to the periodicity of the multiplexing scheme. The coupling results in a shift of the centroid of the reconstructed cluster to some favored positions.
To get rid of these charge coupling effects a new charge correction needs to be applied for the multiplexed readout.

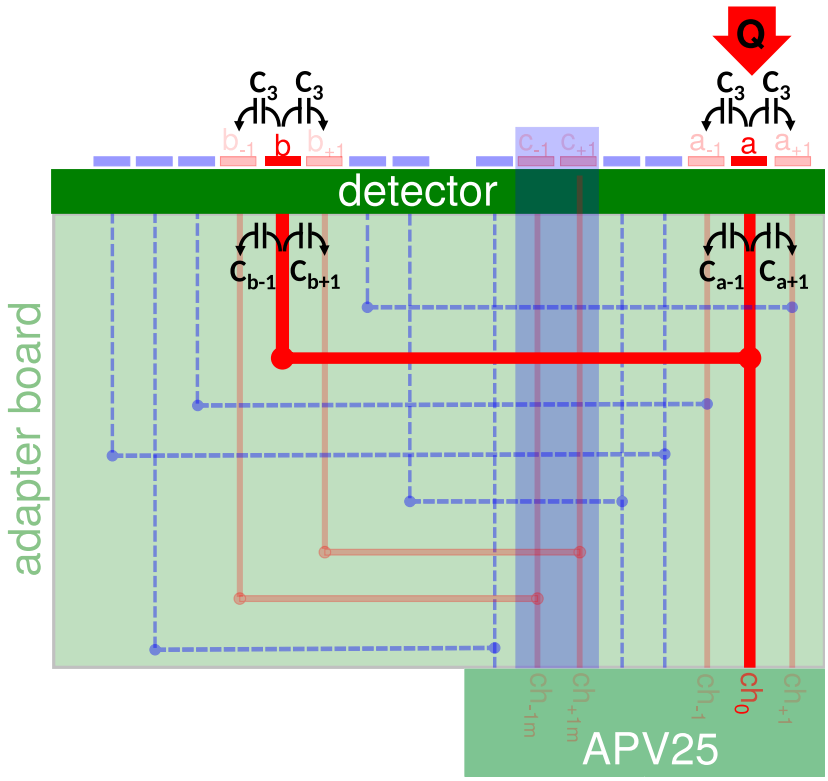

Figure 4.10: Sketch of couplings that can occur for a multiplexed readout. Only couplings to the next readout strips / strip lines on the adapter board are shown.
A charge Q is deposited on strip a. Due to the copper lines on the adapter board respectively the copper readout strips, the charge spreads almost simultaneously to strip b. Due to the capacitances C_3 between neighboring strips in the detector and $C_{a,b\pm1}$ between neighboring strip lines on the adapter board the charge couples to the neighboring strips a_{-1} and a_{+1} which are also adjacent channels ("one to one mapped region"). Strip b also couples to its neighboring strips b_{-1} and b_{+1} in the detector with the capacitance C_3 and on the board with the capacitance $C_{b\pm1}$. Due to this coupling a charge is detected on the APV channels connected to strips c_{-1} and c_{+1}. The marked signal channels are the reason for the marked cluster in figure 4.11.
The electronic channel ch_0 which is connected to strip a measures a charge q_{ch_0}. Due to the capacitive couplings this charge differs from the charge Q, which is deposited on strip a.

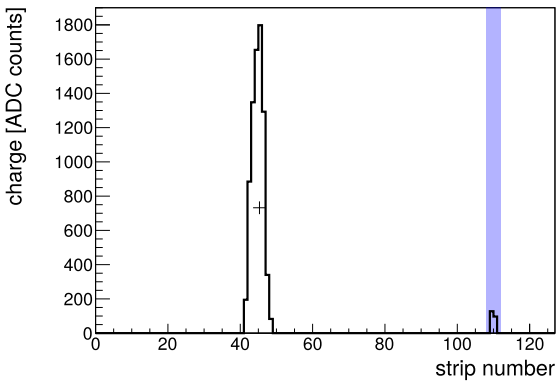

Figure 4.11: Signal of a particle traversing the TZ detector (see chapter 5.1.1) in the "one to one mapped region".
The marked cluster originates from the coupling to non-neighboring strips (same coupling as for the marked signal channels in figure 4.10). The detector was operated with U_{ampl} = 480 V.

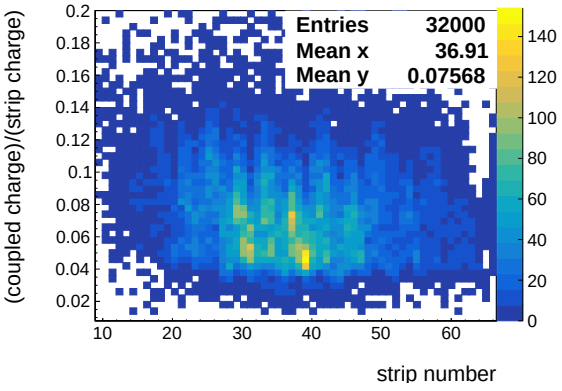

Figure 4.12: Ratio between the coupled cluster (marked cluster in figure 4.11) and the signal cluster.
The ratio is depending on the strip number. It takes values in the range 4 % – 12 %. Data were taken with a TZ detector (see chapter 5.1.1) operated with U_{ampl} = 480 V.

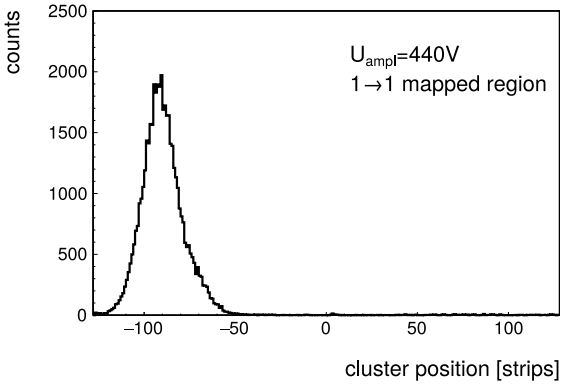

Figure 4.13: Centroid position distribution for a 20MeV proton beam traversing the TZ detector (see chapter 5.1.1) in the "one to one mapped region".
For U_{ampl} = 440 V the Gaussian beam profile can nicely be reconstructed.

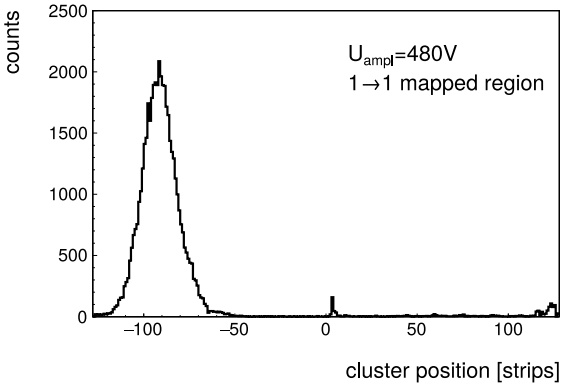

Figure 4.14: Centroid position distribution for a 20MeV proton beam traversing the TZ detector (see chapter 5.1.1) in the "one to one mapped region".
For U_{ampl} = 480 V the Gaussian beam profile can nicely be reconstructed. However some signals were wrongly reconstructed to the "multiplexed region".

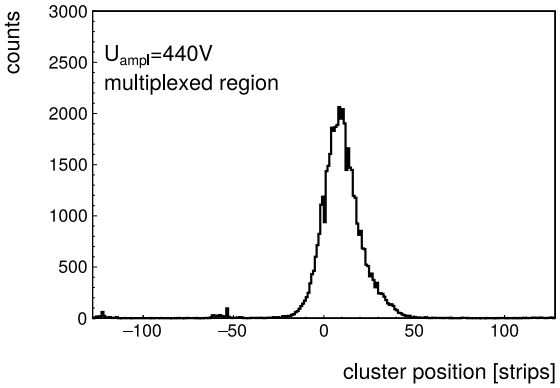

Figure 4.15: Centroid position distribution for a 20MeV proton beam traversing the detector in the "multiplexed region".
For U_{ampl} = 440 V the Gaussian beam profile can nicely be reconstructed.

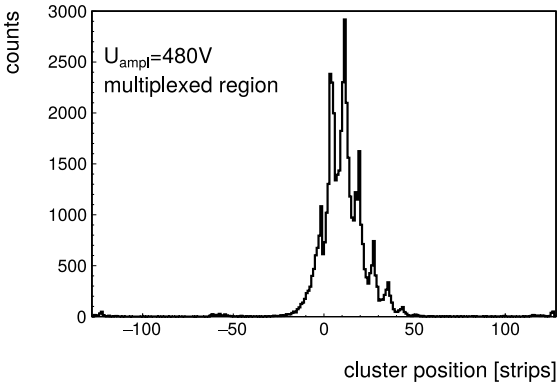

Figure 4.16: Centroid position distribution for a 20MeV proton beam traversing the detector in the "multiplexed region".
For U_{ampl} = 480 V spikes of preferred positions occur every eight strips.

4.4.1 Applied Charge Correction

The charge correction is applied in a similar way as for a non-multiplexed readout (see 2.3). However instead of only the coupling to the adjacent strips all three couplings shown in figure 4.10 must be considered. The coupling correction factor is different than for a non-multiplexed readout. For every event a correction for the strips in the "multiplexed region" as well as for the strips in the "one to one mapped region" needs to be applied separately. A ratio r_{k} of the charge of the neighboring strips is subtracted from the neighboring strips and added to the signal strip.
With the assumption of having a mapping between strips and channels as it is shown in figure 4.10, a charge correction can be applied for each strip and time bin with following equation:

$$\begin{aligned} q_{ch_0}^{cor} &= q_{ch_0} + \sum_{k \in N} (r_k \cdot q_{ch_0}) \\ q_k^{cor} &= q_k - r_k \cdot q_{ch_0} \qquad\qquad \forall k \in N \\ N &= \{ch_{\pm 1}; ch_{\pm 1m}\} \end{aligned} \tag{4.1}$$

The labeling is the same as shown in figure 4.10. The charge correction is executed before the position reconstruction. Therefore it is applied to the electronic channels. ch_0 is connected to the strip a which detected the signal. With the knowledge of the multiplexed mapping a fraction of the charge q_{ch_0} is subtracted from the channels $ch_{\pm 1}$ and added to the channel ch_0. This corrects the coupling for neighboring strips in the "one to one mapped region". For the coupling to neighboring strips in the multiplexed region, a fraction of the charge q_{ch_0} is subtracted from the channels $ch_{\pm 1\mathrm{m}}$ and added to the channel ch_0. The channels $ch_{\pm 1\mathrm{m}}$ are connected to the neighboring strips $b_{\pm 1}$ in the multiplexed region.
When the capacitance of the APV25 chip is neglected, $q_{\mathrm{ch_0}}^{\mathrm{cor}}$ is the same as the charge Q, which is collected on strip a.
Attention must be paid to the charge correction factors r_{k}. They don't need to be equal for the multiplexed and "one to one mapped region". Furthermore they can be slightly different for each channel. The determination of the correction factor is explained in chapter 4.4.2. r_{k} describes the coupling between channel ch_0 and ch_{k}. As for the non-multiplexed readout the correction is also applied to the next but one and next but two neighboring strips.
By applying the charge correction the second cluster of a signal in the "one to one mapped region" vanishes and the signal cluster gets higher and sharper (see figure 4.17). The same effect happens for a signal in the "multiplexed region". Due to the superposition of the coupled electronic clusters and the electronic signal clusters, the charge correction is not as clearly visible in an event as for a signal in the "one to one mapped region". Nevertheless the charges between the two to three electronic clusters are shifted in such a way that the centroid of the reconstructed signal is moved. No strips are favored above others anymore. The spikes in the hit position distribution disappear (see figure 4.18).

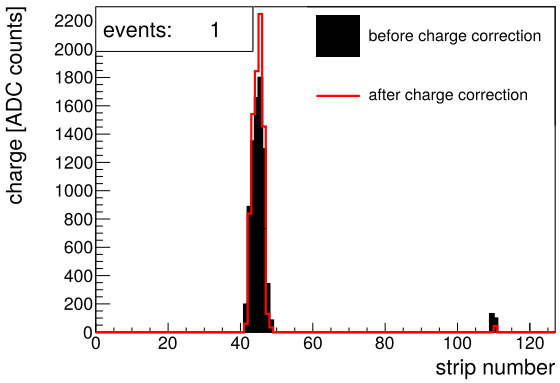

Figure 4.17: Charge correction of a signal created by a particle traversing the detector in the "one to one mapped region" (same event as in figure 4.11).
By applying the charge correction the second cluster is almost removed whereas the pulse height for the signal cluster increases. The detector is operated with $U_{\mathrm{ampl}} = 480\,\mathrm{V}$.

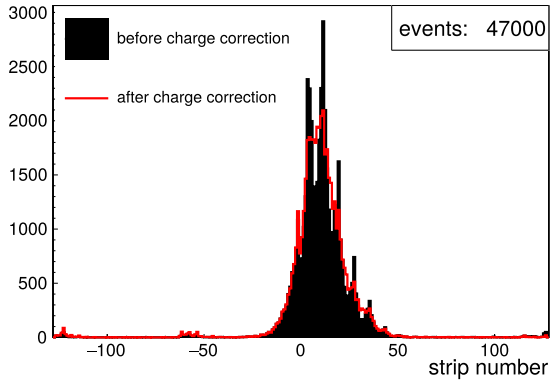

Figure 4.18: Impact of the charge correction on the centroid hit position distribution for a number of particles traversing the detector in the "multiplexed region".
By applying the charge correction the spikes in the hit position distribution vanish. The detector is operated with $U_{\mathrm{ampl}} = 480\,\mathrm{V}$.

4.4.2 Determination of the Charge Coupling Factor

To determine the correction factors, the coupling on the adapter board is required to be understood. This becomes obvious when the hit position distribution and the board geometry are compared (see figure 4.19). It is conspicuous that the spikes in figure 4.16 are located at the position where neighboring strips are only three electronic channels apart from each other.
To comprehend that, the capacitances between neighboring strips (up to the next but two neighboring strips) on the adapter board ($C_{\mathrm{a}_{\pm1}}$ and $C_{\mathrm{b}_{\pm1}}$ in figure 4.10) were measured with a LCR-meter[3]. The capacitances ($\mathcal{O}\,(\mathrm{pF})$) were measured with a precision of 0.1 pF. The total capacitance, which is connected to one electronic channel (ch_0), can be calculated as the sum of the capacitances to all neighboring strips. However the capacitance of strips further apart than the next two adjacent strips are negligible small. Therefore only the capacitances up to the next but two neighboring strips in the "one to one mapped region" ($C_{\mathrm{a_k}}$) as well as in the "multiplexed region" ($C_{\mathrm{b_k}}$) are considered. If the adapter board is connected to the detector, the capacitances of the two readout strips connected to the electronic channel ch_0 need to be added (C_{det}). The total capacitance which is connected to channel ch_0 is:

$$C_{ch_0} = \sum_{k\in\{\pm1;\pm2\}} (C_{a_k} + C_{b_k}) + 2 \cdot C_{det} \tag{4.2}$$

A fraction f of the charge Q deposited on strip a couples to each neighboring strip. With the knowledge of the capacitances C_{i} to the neighboring strips, and the total capacitance connected to one channel C_{ch_0}, f can be calculated:

[3]The used LCR meter is "Model 878B" from B&K Precision Corporation [B&K-Precision-Corporation].

$$f_i = \frac{C_i}{C_{ch_0}} \qquad \forall i \in \{a_{\pm 1}; b_{\pm 1}\} \tag{4.3}$$

Since the coupling factor r_i in equation 4.1 refers to the charge q, which is collected by the electronics, and not to the charge Q which is deposited on strip a, f_i needs to be transformed to r_i:

$$r_i = \frac{f_i}{1 - \sum\limits_{j \in \{a_{\pm 1}; b_{\pm 1}\}} f_j} \qquad \forall i \in \{a_{\pm 1}; b_{\pm 1}\} \tag{4.4}$$

To apply this factor for the charge correction $r_{\mathrm{a}_{\pm 1}}$ is used as $r_{\mathrm{ch}_{\pm 1}}$ and $r_{\mathrm{b}_{\pm 1}}$ is used as $r_{\mathrm{ch}_{\pm 1\mathrm{m}}}$ in equation 4.1.
The calculated coupling ratios for the board which is not connected to the detector are shown in figure 4.20.

Among other things, the length where two neighboring readout strips / strip lines are running parallel to each other is decisive for the capacitance between two strips. Therefore, a distinction between the coupling factor for the "multiplexed region" ($r_{\mathrm{ch}_{\pm 1\mathrm{m}}}$), and for the "one to one mapped region" ($r_{\mathrm{ch}_{\pm 1}}$) is clearly visible. In the "one to one mapped region" neighboring strip lines have approximately the same length. Therefore the coupling is almost independent of the channel number.
The coupling factor in the "multiplexed region" is strongly depending on the board geometry. The coupling between neighboring strips, which are only three electronic channels apart from each other (marked strips in figure 4.19) is much stronger as if the distance is 63-67 electronic channels.
For the "one to one mapped region" and "multiplexed region" there is a step in the coupling factor, between channel 63 and 64. This is created by the geometry of the two groups of strip lines (see figure 4.2), connecting the strip in the "one to one mapped region" and the strip in the "multiplexed region". The coupling strength depends on the length of two neighboring strips running parallel to each other on the adapter board. For instance the coupling between the marked strip lines in figure 4.19 is stronger for the first 64 channels as for the channels 64 – 128. In the channels 64 – 128 the parallel length is smaller as for the first 64 channels.

Generally the dependence of the coupling ratio on the spatial distance between the strip lines on the board and the length of the strip lines is shown in figure 4.20.
By connecting the board to the detector the impact of the geometry of the board gets smaller. If the capacitance connected to one strip on the adapter board is much larger than the capacitances on the adapter board, the impact of the board geometry is almost negligible. (see figure 4.21).

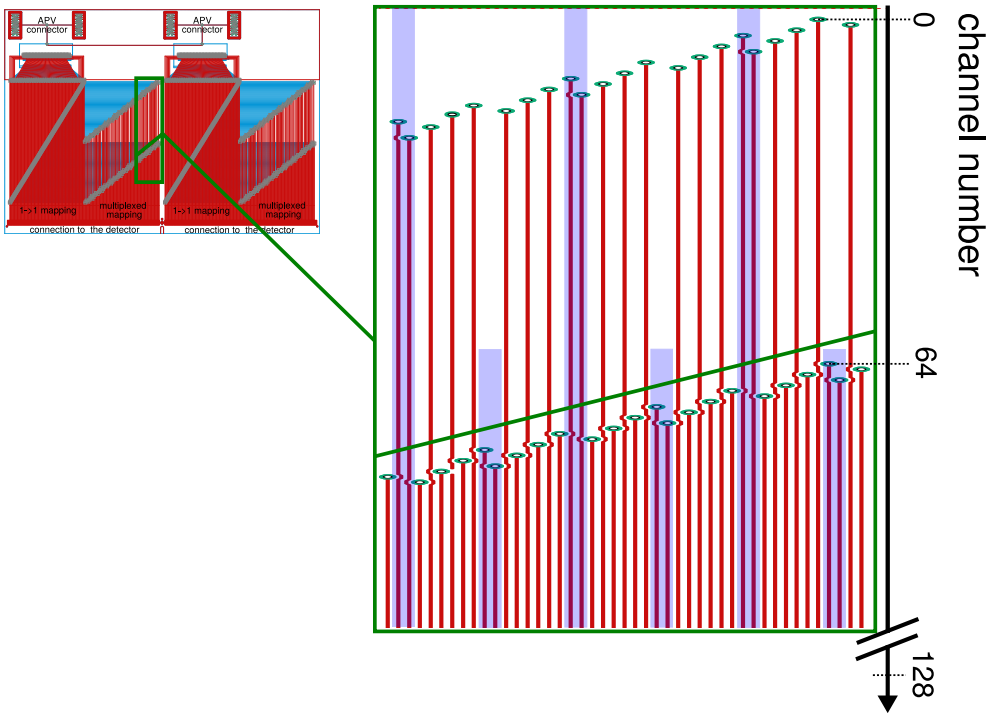

Figure 4.19: Section of the strip lines on the adapter board which were connected to the strips which detected the signals in figure 4.16.
The marked strip lines refer to the position of the spikes. The beginning of the lines (—●) shows the channel number, to which the strip is connected.

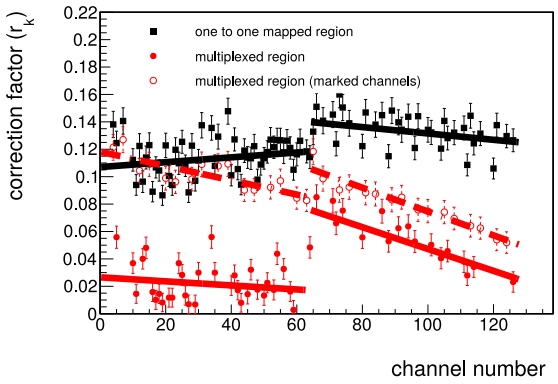

Figure 4.20: Coupling ratio to the neighboring strips in dependence of the channel number.
The shown values are the correction factors for the adapter board without a connected detector. Straight line fits are superimposed.

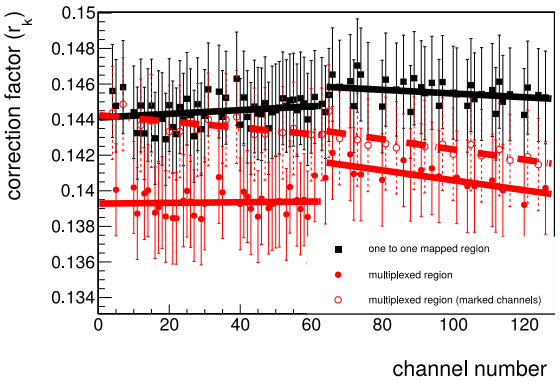

Figure 4.21: Coupling ratio to the neighboring strips in dependence of the channel number.
A detector with 1,5 m long readout strips (SM2 detector) is connected to the adapter board. The coupling ratio is almost independent of the geometry of the board (geometry dependency $\approx 1\,\%$). Straight line fits are superimposed.

Chapter 5

Measurements at the SPS at CERN

To investigate the impact of the increased capacity on the pulse height, measurements were performed at Super Proton Synchrotron (SPS) at CERN. The SPS accelerates protons up to an energy of E_{SPS} = 450 GeV [CERN, 2019b]. Either this 450GeV protons are injected into the LHC, or they are used for experiments like the COMPASS experiment [Abbon et al., 2007], and for detector testing at some for this purpose set up beam lines.

5.1 Experimental Setup

For this thesis measurements were performed at the H8 beam line in the CERN northern area, using 120 GeV pions. The pions were created from the protons accelerated by the SPS. 120 GeV pions are almost minimum ionizing particles with $\beta\gamma \approx 860$ (see figure 1.2). Since the mean energy loss is very low for minimum ionizing particles, a pion is most likely not stopped by the experimental setup. Due to the high energy of the pions the impact of multiple scattering is negligibly small (see equation 1.1). Therefore, one may not worry about the material budget of the detectors in the beam.
The experimental setup can be seen in figure 5.1. The scintillators, the SM2 detector and the TZ detectors were used for the measurement. Scintillators were used for triggering.

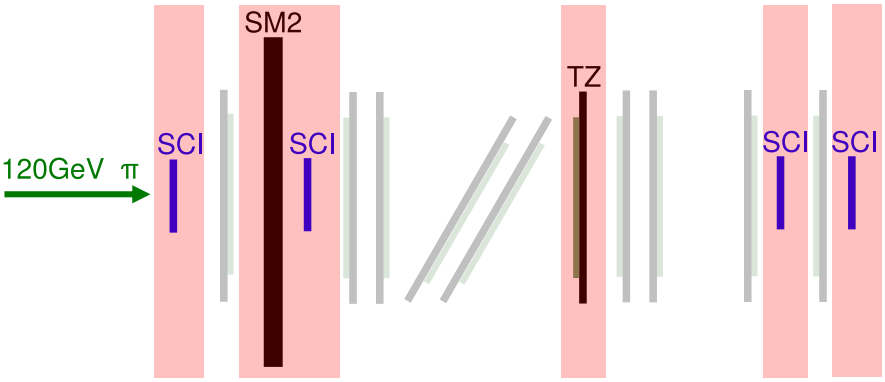

Figure 5.1: Setup for the test beam at the H8 beam line at SPS. Only data from the marked detectors are actually used for this thesis.
The scintillators (SCI) were used for triggering. TZ and SM2 were both read out using a multiplexed adapter board and an adapter board which combines two neighboring readout strips to one electronic channel.

5.1.1 TZ Detector

The TZ detector is a 10×10 cm^2 large resistive strip Micromegas detector with a one dimensional readout. The used detector has 256 readout strips with a strip periodicity of $p = 400\,\mu$m. The TZ is a bulk type Micromegas detector, meaning a Micromegas detector with a mesh integrated on the PCB. It is laminated on top of the pillars in a fixed distance from the readout strips [Giomataris et al., 2006]. The height of the amplification gap is estimated to be around $h_{\text{ampl}} = 100\,\mu$m. The height of the drift region is measured to be $h_{\text{drift}} = 5\ mm$.
Since the exact measures are not known only the voltages U_{drift} and U_{ampl} are used in the following instead of electric fields E_{drift} and E_{ampl}.
For the presented measurements, the TZ detector was flushed with $\text{Ar} : \text{CO}_2$ 93 : 7 vol. %.

5.1.2 SM2 Detector

The SM2 detector is an approximately 2 m^2 large resistive strip Micromegas detector with an one dimensional micro pattern readout. The readout consists of 12288 parallel readout strips on four active layers. Each layer has roughly 3000 readout strips. The detector is trapezoidally shaped (see figure 5.2). Therefore the readout strip length varies between 110 cm and 160 cm. The strip periodicity is 425 μm. In contrast to the TZ detector the SM2 module is not a bulk Micromegas detector. The mesh lies on top of pillars with a height of $h_{\text{ampl}} = 128\,\mu$m. The drift region has a height of $h_{\text{drift}} = 5$ mm. For more details of the detector see [ATLAS-Muon-Collaboration, 2014].
For the presented measurements, the SM2 detector was flushed with $\text{Ar} : \text{CO}_2$ 93 : 7 vol. % as well.

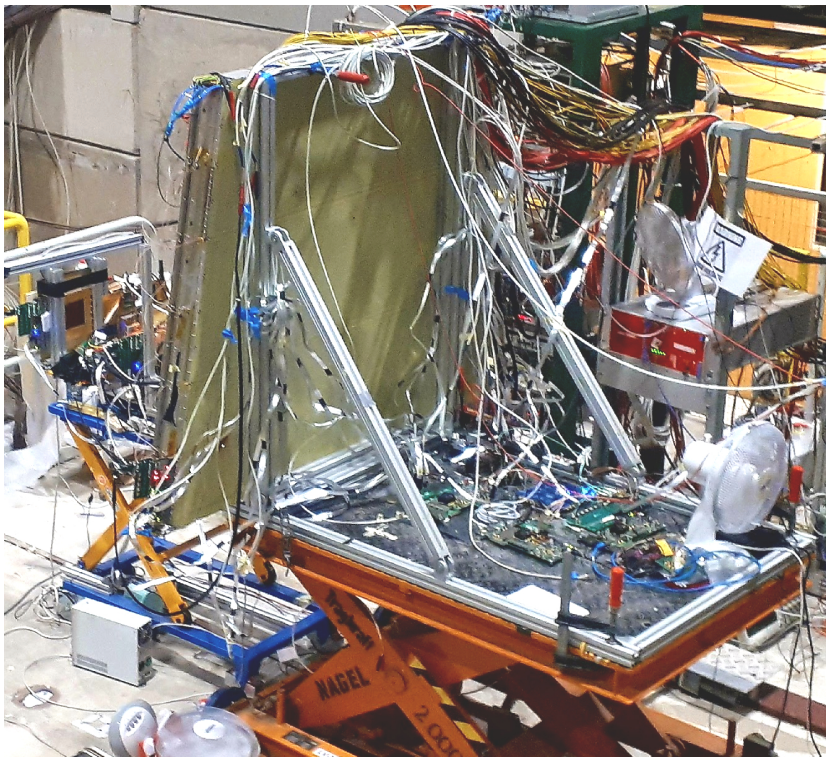

Figure 5.2: Picture of the 2 m^2 large SM2 detector, placed in the setup at the H8 beam line.

5.2 Performed Measurements

The TZ detector and SM2 detector were alternately read out with a non-multiplexed readout adapter board and with an adapter board which combines two neighboring strips to one electronic channel. In this chapter this readout is called coupled readout. This readout is not fulfilling the mapping rules presented in chapter 3.1.3. It doubles the strip pitch of the detector as shown in figure 3.6. Therefore, the spatial resolution of the detector obtained with this readout decreases. The spatial resolution is not determined at this measurements. Only the pulse height (cluster charge) created by a pion traversing the detector is measured and compared for both readouts. The total capacitance connected to an electronic channel is approximately the same for the coupled readout adapter board as for the previous explained multiplexing adapter board. Therefore, the impact of the multiplexing adapter board on the pulse height can be observed. The pulse height is expected to be lower for coupled readout as for the non-multiplexed readout.
The cluster charge, $\sum_{\text{cluster}} q_{\text{strip}}$ is used for this measurements as the pulse height. It is the amplified signal originating from a traversing particle. It represents the energy loss of a particle traversing the detector. For a number of particles which traverse a thin medium (i.e. the gas mixture inside the detector) the energy loss is Landau distributed. Therefore, the pulse height distribution for a number of events is Landau distributed as well (see figure 5.3). To compare the pulse height for different readouts, the most probable value of the distribution is used, which is determined by a fit with a Landau function.

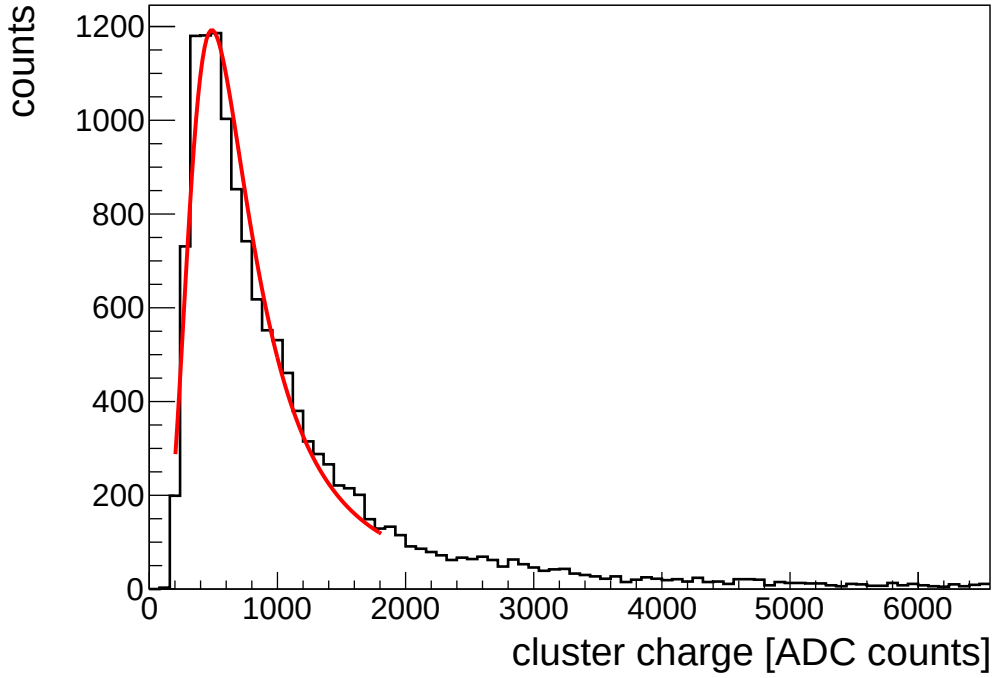

Figure 5.3: Landau distributed cluster charge for 13000 events.
In the following, the most probable value of the Landau fit is used as the cluster charge for a measurement. Data are taken with the SM2 with $U_{\text{ampl}} = 560\,\text{V}$, which is irradiated with 120 GeV pions.

5.3 Results

As explained in chapter 3.2.1 the signal pulse height of a traversing particle is expected to decrease with an increasing capacitance connected to one electronic channel. For a 120 GeV pion beam this is nicely shown in figure 5.4. The cluster charge of the signal cluster (pulse height) for the TZ detector with a readout strip length $l_{\mathrm{TZ}} = 10\,\mathrm{cm}$ is much higher compared to the SM2 detector with a readout strip length $l_{\mathrm{SM2}} > 110\,\mathrm{cm}$. By increasing the capacitance by a factor ≈ 2 the signal pulse height decreases by a factor $\approx 20\,\% - 30\,\%$.
The connection of more than two readout strips to one electronic channel would lead to an even more significant decrease of the pulse height. In particular the signal of the SM2 detector can become indistinguishable from noise and gets lost in the zero-suppression (see chapter 2.2.1).
One can compensate this effect by increasing the amplification voltage. However this is limited due to plasma discharges in the amplification region (see chapter 1.1.3).

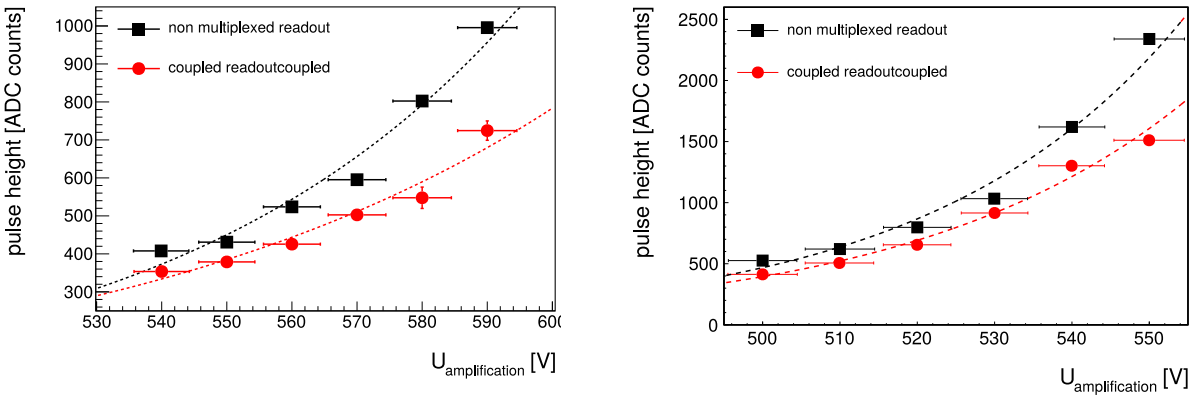

Figure 5.4: Signal pulse height of the SM2 detector (left) and the TZ detector (right). The detectors were read out with a non-multiplexed readout and with a readout where two neighboring readout strips were connected to one electronic channel. The data were taken with 120 GeV Pions. The shown points are the most probable values for about 15000 events.

Chapter 6

Measurements at the Tandem Accelerator in Garching

To verify the functionality of the multiplexing adapter board, measurements are performed at the Tandem-van de Graaff accelerator of the Maier-Leibtnitz-Laboratorium in Garching [Maier-Leibnitz-Laboratorium, 2014]. The readout is tested with a high intensity 20 MeV proton beam. 20 MeV protons with $\beta\gamma \approx 0.02$ are strongly ionizing particles (see figure 1.2). The mass stopping power for 20 MeV protons is much higher as for 120GeV pions, which are used for the measurements at the SPS. The protons are more likely to be stopped by the experimental setup. Furthermore, a particle with a lower momentum is more likely be scattered, by all the material in the beam (see equation 1.1). Therefore, it is indispensable that as little material as possible is located in the proton beam. Absorbers in the accelerator limit the particle flux to values between $0.9\,\mathrm{kHz/cm^2}$ and $1.8\,\mathrm{kHz/cm^2}$.

6.1 Experimental Setup

The experimental setup is shown in figure 6.1. A $10\times10\,\mathrm{cm^2}$ large GEM detector [Sauli, 1997] is used as a reference detector as well as for triggering. The TZ detector is read out with a non-multiplexed readout adapter board, and with the developed multiplexed adapter board (see chapter 4.1). This measurements can not be performed with the SM2 detector, since the material budget, the proton has to pass through to reach the drift region, is too high.
The TZ detector can be tilted to investigate the behavior of the detector for inclined particle tracks. The hit position in the detector can be adjusted by changing the height Δh of the table the setup is mounted on.
For the measurements at the tandem accelerator the same $10 \times 10\,\mathrm{cm^2}$ TZ detector is used as for the measurements at the SPS at CERN (see chapter 5.1.1). The TZ detector has only 256 readout strips. Since both, the multiplexed adapter board, and the non-multiplexed adapter board have 512 strip lines, only the middle 256 strip lines of the adapter board can be connected to the detector due to the layout of the Zebra connector and its holder (see figure 6.2).
Whereas this is irrelevant for the non-multiplexed readout, this has to be considered for the multiplexed readout. When the multiplexed adapter board is used, the first 128 strips are connected by the "one to one mapping" to the first APV. The second 128 strips are connected by the "multiplexed mapping" to the second APV25 front-end board. All the other strip lines on the adapter board are not connected. Thus each electronic channel is connected to one strip only.
Admittedly, this setup does not lead to a reduction of the readout electronics. However, by

only using the APV channel number without the APV ID, the signal of both APVs can be merged to a signal, which looks like a multiplexed signal of one single APV25. Therefore, it is not possible to draw conclusions about the impact of the multiplexed readout on the pulse height[1]. Though it is possible to observe the couplings between the strip lines on the adapter board, as described in chapter 4.4, and to test the signal reconstruction.
Furthermore, the fluctuation of the pulse height (see chapter 2.2.1) is investigated for both readouts. It is measured, when the detector is not irradiated. Therefore, by replacing the TZ detector with the SM2 detector, the fluctuation can also be determined for the SM2 detector.

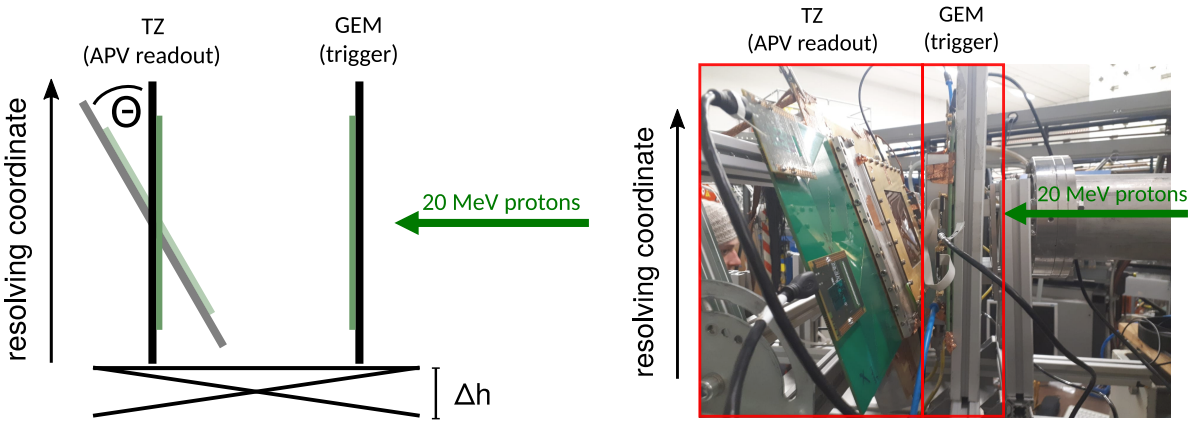

Figure 6.1: Setup for the Tandem test beam. Whereas the schematic setup is shown on the left, a picture of the used setup is shown on the right.
The GEM detector is used for triggering and as a reference detector. The detectors are read out with APV25 front-end boards. The TZ detector is read out with a non-multiplexed readout adapter board at first, and later on with the multiplexed adapter board. TZ can be tilted by an angle Θ to change the angle of incidence of the proton beam. By adjusting the height (Δh) of the setup table the hit position along the precision coordinate can be changed.

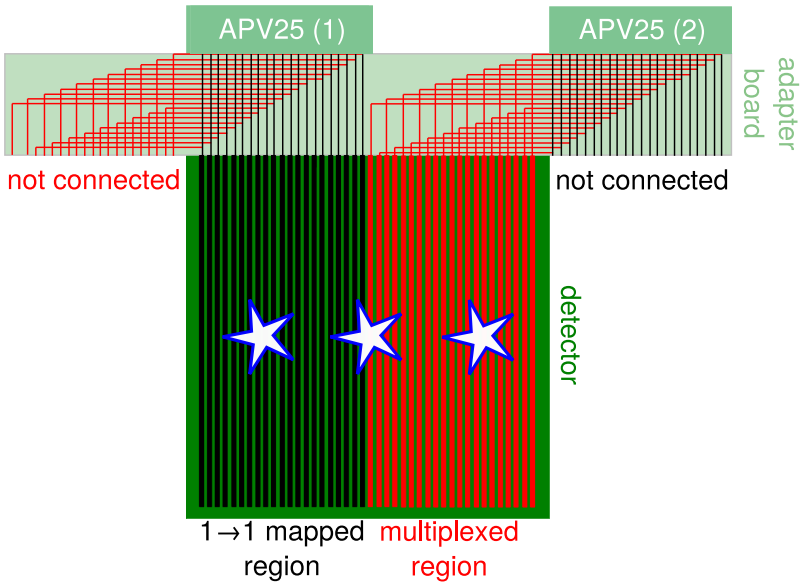

Figure 6.2: Setup of the TZ detector.
The detector is connected in such a way, that one APV is connected either only to the "one to one mapped region" or only to the "multiplexed region". The remaining strips on the multiplexing adapter board were not connected to the detector. In Black the strips connected to the "one to one mapped region" are shown. The red strips are the strips referring to the "multiplexed region". The different positions which were irradiated are indicated by the stars.

[1]The impact of the multiplexed readout on the pulse height is studied in chapter 5.2

6.2 Performed Measurements

The TZ detector was irradiated at three different positions. To probe the functionality of the signal reconstruction according to chapter 4.2, the detector is irradiated separately in the "one to one mapped region" and later on in the "multiplexed region" (see figure 6.2). Knowing how the signal looks like for these two positions (see figure 4.5 and figure 4.6), the charge correction and noise canceling was improved.
To investigate the multiplexed readout, the transition region between the multiplexed, and "one to one mapped region" is irradiated.
Even though the GEM detector is a low material budget detector the total scattering of the protons is too large to determine a comparable hit position in both detectors (see figure 6.3). Whereas it is possible to reconstruct the absorber position with the GEM detector, the protons at the TZ detector are already scattered that often that only a Gaussian beam profile is reconstructed at position of the TZ detector. Comparing the beam width at the GEM detector and at the TZ detector and knowing the distance Δz between the two detectors a rough measure for the multiple scattering angle can be estimated:

$$\Phi = arctan\left(\frac{\sigma_{TZ} - \sigma_{GEM}}{\Delta z}\right) \tag{6.1}$$

With an average distance of $\Delta z = 15\,\text{cm}$ the maximum mean scattering angle is between $\Phi \approx -3.4°$ and $\Phi \approx 3.4°$.
Therefore, the measured spatial detector resolution in the order of ($\mathcal{O}(mm)$) at the Tandem accelerator (see figure 6.5) is significantly above the demanded detector resolution for the TZ detector ($\mathcal{O}(50 - 100\ \mu m)$). Thus it is not possible to investigate the impact of the multiplexed readout on the detector resolution. It is only tested if the Gaussian beam profile can be reconstructed with the multiplexed adapter board. Therefore the demultiplexing efficiency is determined.
By tilting the detector, the angle of incidence of the proton beam is varied. The reconstructed angle, as well as the angular resolution is measured and compared for both readouts.
Furthermore, the fluctuation of the pulse height (see chapter 2.2.1) for the TZ detector and the SM2 detector is measured and compared for both readouts.
For most measurements, the drift voltage (U_{drift}) is chosen in such a way that the drift velocity of the electrons (v_{drift}) gets maximum, whereas the amplification voltage (U_{ampl}) is varied. For $Ar : CO_2$ 93 : 7 vol. % this is fulfilled for $U_{\text{drift}} = 0.5\,\text{kV/cm}$ (see figure B.1 in the appendix).

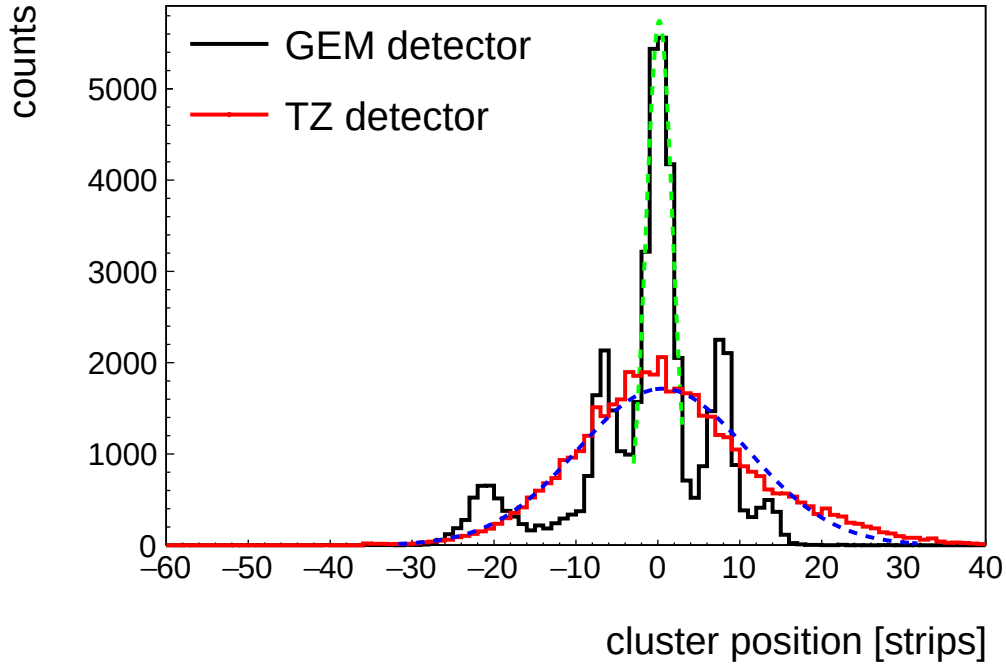

Figure 6.3: Comparison of the measured hit position distribution between the GEM detector and TZ detector for $U_{\mathrm{ampl}} = 450\,\mathrm{V}$.
To determine the size of the beam spot each distribution is fit with a Gaussian function. The width at the GEM detector is: $\sigma_{\mathrm{GEM}} = 1.6\,\mathrm{strips}$. At the TZ detector it is $\sigma_{\mathrm{TZ}} = 10.5\,\mathrm{strips}$. The spikes at the GEM detector are resulting from the absorbers in the beam line. Due to multiple scattering this spiky beam profile is washed out. The hit distribution is wider at the position of the TZ detector. Both distributions show 46 740 entries.

6.2.1 Efficiency Determination

To determine the efficiency, the residual of the hit position in TZ (x_{TZ}) has to be calculated. The residual (Δx) is the difference between the predicted hit position in TZ and the measured hit position (see figure 6.4). With the assumption of having straight and perpendicular particle tracks through the GEM detector, the hit position in the GEM detector (x_{GEM}) is used as a reference particle position.
In this case the residual calculates as:

$$\Delta x = x_{GEM} - x_{TZ} \tag{6.2}$$

After the alignment of the detectors, the mean value of the residual distribution ($mean$) for a number of events is centered at zero (see figure 6.5). Since only a single reference detector is used for the reconstruction of a reference track, the residual is strongly influenced by the resolution of the GEM detector and the misalignment of the setup. In comparison to the multiple scattering this is negligibly small.
To obtain a measure for the resolution, the residual is fit with a double Gaussian function:

$$\begin{aligned} f(\Delta x) &= G_{small}(x) + G_{large}(x) \\ f(\Delta x) &= p_0 \cdot exp\left(-0.5\left(\frac{\Delta x - \Delta x_{MPV}}{\sigma_{small}}\right)^2\right) + p_1 \cdot exp\left(-0.5\left(\frac{\Delta x - \Delta x_{MPV}}{\sigma_{large}}\right)^2\right) \end{aligned} \tag{6.3}$$

Most events close to the mean are within the core Gaussian function (G_{small}). The tail of the distribution towards larger residuals is considered by the large Gaussian (G_{large}) function. It is created by delta electrons and non-correctable misalignment of the setup, as for the correction two-dimensional detectors would be necessary. The width of the distribution (σ) is a measure for the resolution of the detector. It is determined by weighting σ_{small} and σ_{large} with the integral of the corresponding single Gaussian function.

$$\sigma = \frac{\sigma_{small} \cdot \int G_{small}(x)\,\mathrm{d}x + \sigma_{large} \cdot \int G_{large}(x)\,\mathrm{d}x}{\int G_{small}(x)\,\mathrm{d}x + \int G_{large}(x)\,\mathrm{d}x} \tag{6.4}$$

The sigma is needed to determine the detection efficiencies. But, due to the strong multiple scattering, the width of the distribution is too large to draw conclusions about the detector resolution.
It is assumed that all events in an acceptance range $[\mathrm{mean} - 25\,\mathrm{mm}; \mathrm{mean} + 25\,\mathrm{mm}]$ are correctly demultiplexed. This means an event in the "one to one mapped region" is reconstructed to the "one to one mapped region", respectively an event from the "multiplexed region" is reconstructed to the "multiplexed region". The signal reconstruction efficiency is defined as:

$$efficiency = \frac{\#events_{accepted}}{\#trigger} \tag{6.5}$$

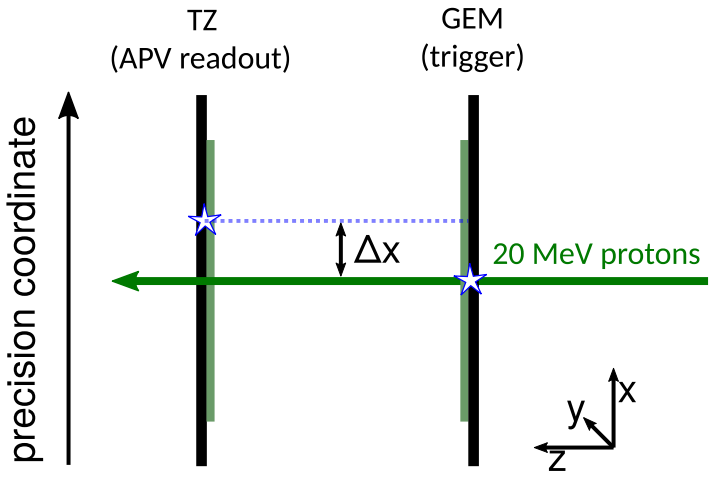

Figure 6.4: Sketch of the residual determination.
The star indicates the measured hit position in each detector. The angle of incidence at the reference detector (GEM) is assumed to be perpendicular. The GEM has a good spatial resolution so that the reference track is defined by the hit position in the GEM detector. The distance Δx between the two hit positions is called residual in x direction.

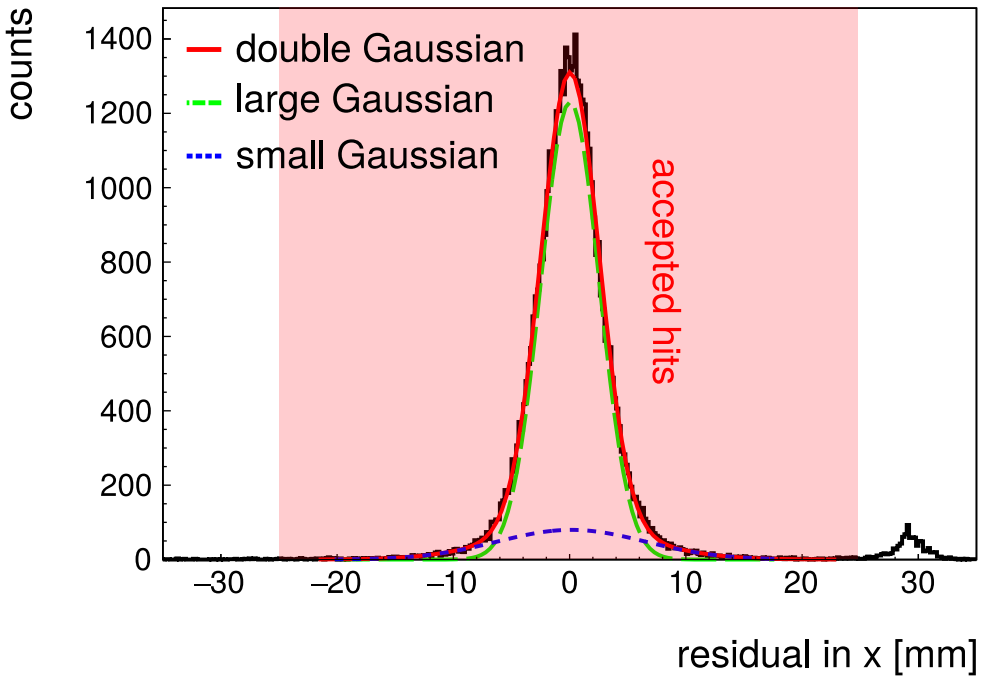

Figure 6.5: Residual distribution for the TZ detector with a multiplexed readout.
The peak at 30 mm results from a wrongly reconstructed position due to multiplexing. Events in the red marked acceptance range are considered as correctly demultiplexed.

6.2.2 Determination of the Angular Properties

The angle of incidence is reconstructed via the µTPC method (see chapter 2.1.2). At least three strips have to detect a signal. Otherwise the linear fit of the timing for the different strips is too strongly influenced by the uncertainties of the strip timing. To avoid systematic errors, the reconstructed angle is filled in a histogram with a variable binning (see figure 6.6) [Bortfeldt, 2014]. The most probable value is used as the reconstructed angle for the measurement. Since the mean value for the multiple scattering is centered at zero (see chapter 1.1.1), the most probable reconstructed angle is independent of the multiple scattering.
The tail towards $|\Theta| = 90°$ in the angular distribution (see figure 6.6) originates from not fully corrected capacitive coupling.
To determine an angular resolution, the distribution is fit with two Gaussian functions with the width $\sigma_>$ and $\sigma_<$ according to [Bortfeldt, 2014]:

$$\begin{aligned} f_<(\Theta) &= p_0 \cdot exp\left(-0.5\left(\frac{\Theta - \Theta_{MPV}}{\sigma_<}\right)^2\right) \quad \forall|\Theta| \leqslant |\Theta_{MPV}| \\ f_>(\Theta) &= p_0 \cdot exp\left(-0.5\left(\frac{\Theta - \Theta_{MPV}}{\sigma_>}\right)^2\right) \quad \forall|\Theta| > |\Theta_{MPV}| \end{aligned} \tag{6.6}$$

The widths σ of these two functions are a measure for the angular resolution. However the width of the distribution is enlarged due to multiple scattering.
Similar to the position reconstruction efficiency an angle reconstruction efficiency is calculated. The number of events in a certain range (for this thesis $\Theta_{\mathrm{MPV}} \pm 2\sigma$) is compared with the number of triggers:

$$efficiency = \frac{\#events_{\Theta_{MPV} \pm 2\sigma}}{\#trigger} \tag{6.7}$$

The angle reconstruction is investigated for three different angles of inclination ($\Theta \in \{20°, 30°, 40°\}$). The detector is irradiated at the transition region of the multiplexing adapter board.

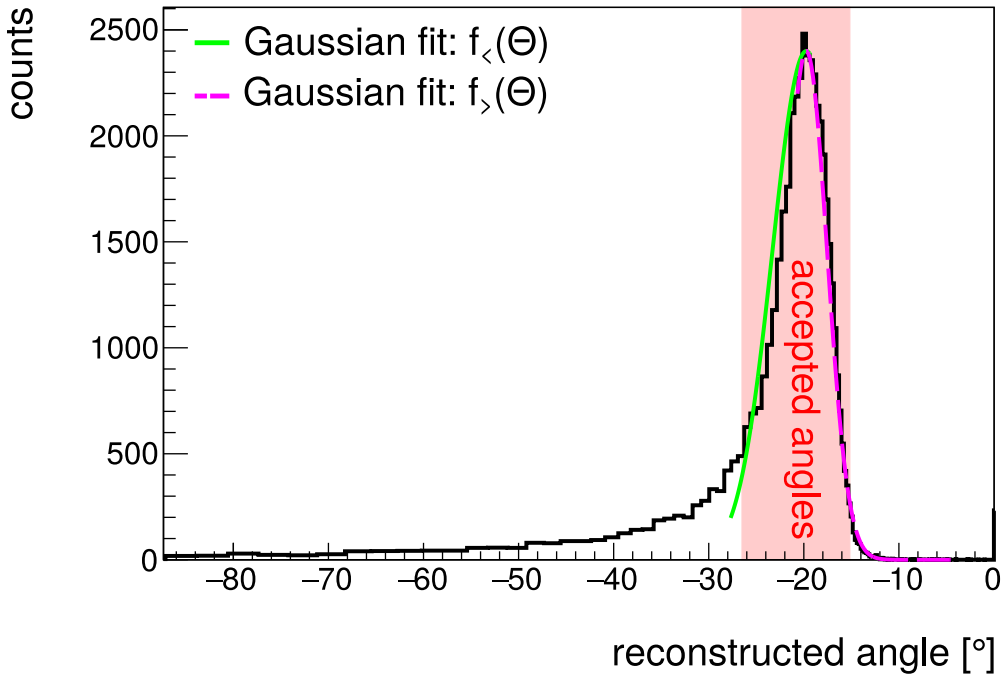

Figure 6.6: Distribution of the reconstructed angle for 47500 events. The detector is tilted by an angle $\Theta \approx 20°$
The most probable value of this distribution is used as the reconstructed angle whereas the widths of the two fit Gaussian functions is used as a measure for the angular resolution. The width is obtained by a fit with an asymmetric Gaussian function (see equation 6.6).

6.3 Results

In the following, the results for the previously described measurements are presented.

6.3.1 Noise Coupling

As described in chapter 3.2.2 the ratio of coupled noise is expected to increase for a multiplexed readout. Since no irradiation of the detector is needed for this measurement, the noise level of the detector was determined at the Tandem accelerator for the TZ detector and for the SM2 detector. The results are shown in figure 6.7. In both cases, the noise level increases when the multiplexed readout is used. For the TZ detector, where only one readout strip is connected to one electronic channel (see figure 6.2), the noise level increases only slightly. This means the impact of the board itself to the noise coupling is rather low. For the SM2 detector, the increase of the noise level, by applying the multiplexed readout, is obvious. Combined with the lower signal pulse height (see chapter 4.2) this leads to a decrease of the signal to noise ratio. Thus a signal is more likely lost at the zero-suppression (see chapter 2.2.1). It is very important for the demultiplexing of a signal in the "multiplexed region" that every electronic signal cluster exists. Therefore a decrease of the signal to noise ratio can easily lead to a wrong reconstructed cluster position.

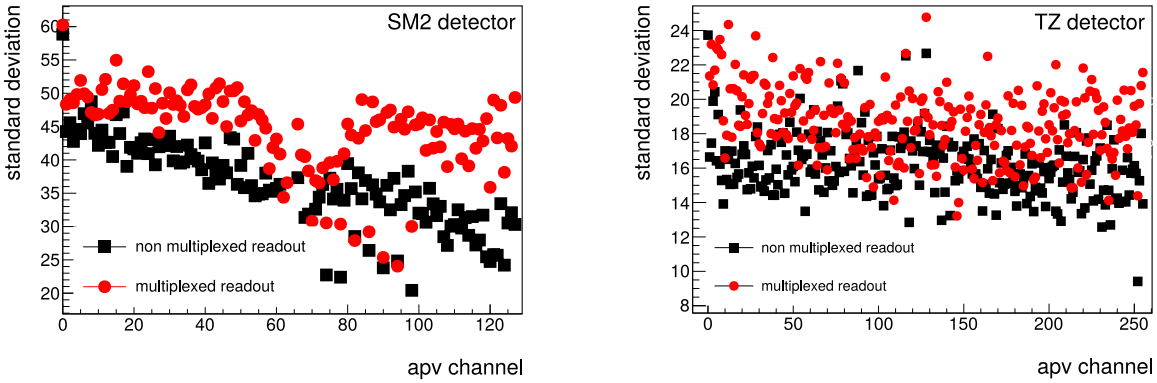

Figure 6.7: Fluctuations of the pulse height for events without a particle signal (see chapter 2.2.1). On the left the fluctuation of the pulse height for the SM2 detector are shown, and on the right data for the TZ detector are shown. The fluctuation of the pulse height is a measure for the coupled noise.

6.3.2 Position Reconstruction

The functionality of the multiplexing adapter board is shown in the reconstructed hit position. If the position reconstruction efficiency is the same for the non-multiplexed readout as for the multiplexed readout, the functionality of the multiplexing adapter board is proven. The position reconstruction efficiency of TZ for both readouts is displayed in figure 6.8. For high enough amplification voltages ($U_{\text{ampl}} \geqslant 400\,\text{V}$) it is about the same. The difference in the efficiency of up to 1 % originates from the mechanical movement of the setup during the exchange of the adapter board. Either the angle of incidence, or the hit position in the detector can slightly be different and contributing to this mismatch.
The drop of the efficiency for the multiplexed readout at lower amplification voltages is due to the more frequent loss of the second electronic cluster of the signal in the "multiplexed region". The cluster can either be lost at the zero-suppression (see chapter 2.2.1), or during the noise canceling in the analysis (see chapter 4.3). Such an event is shown in figure 6.9. In this example a part of the second cluster in the electronics is lost during the noise canceling in the analysis, the second part is already lost during the zero-suppression. With only one cluster in the electronics remaining, the signal is falsely reconstructed to the "one to one mapped region".
Overall, the signal is reconstructed to the correct position range for high enough amplification voltages. A precise resolution was not determined due to the strong multiple scattering.

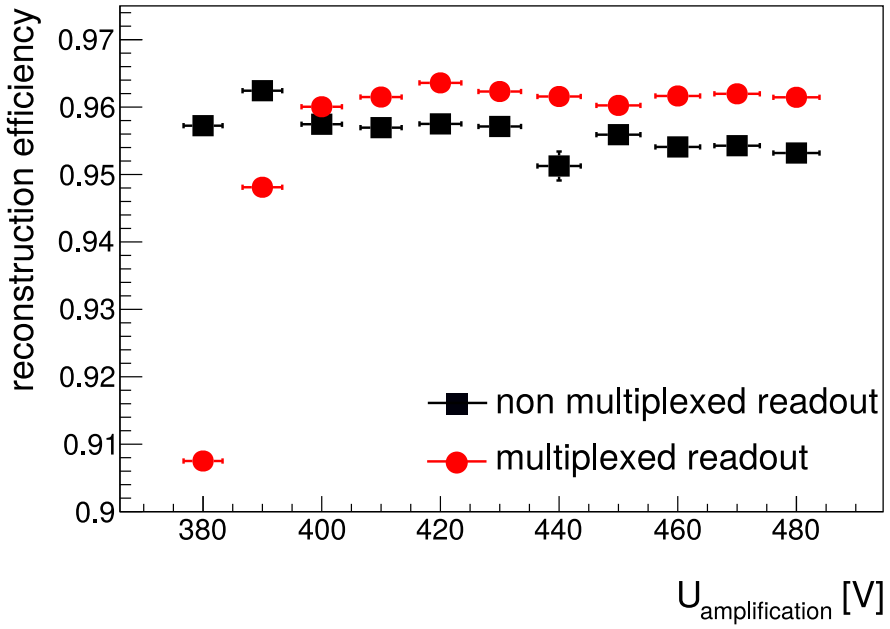

Figure 6.8: Position reconstruction efficiency of the TZ detector for the multiplexed and non-multiplexed readout.
The detector is irradiated with 20MeV protons. The efficiency is determined with equation 6.5. The drop of the efficiency for lower amplification voltages for the multiplexed readout is due to the loss of the second electronic cluster in the "multiplexed region". The multiplexed efficiency might be slightly higher than the non-multiplexed efficiency due to the mechanical movement of the setup in between the two measurements.

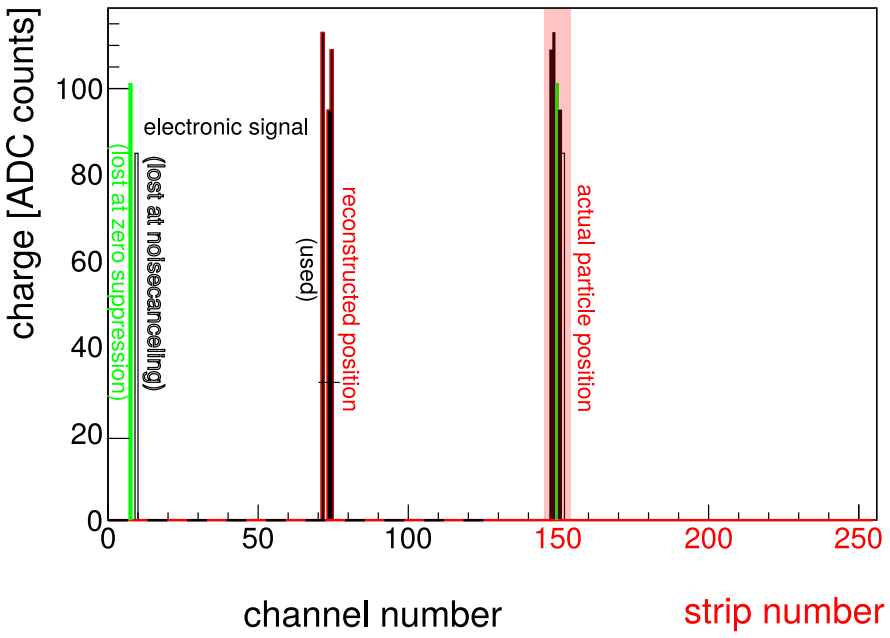

Figure 6.9: Wrong reconstructed position of a particle which traversed the detector in the "multiplexed region".
Due to missing a missing second electronic cluster the cluster is reconstructed to the "one to one mapped region".

6.3.3 Angle reconstruction

The reconstructed angle is expected to be approximately the same for the multiplexed and for the non-multiplexed readout. To verify that, the most probable reconstructed angle is compared for both readouts.
In figure 6.10 the reconstructed angle for 20MeV protons traversing the TZ detector under an angle of incidence of $\Theta = 20°$ is shown. The reconstructed angle is approximately the same for the non-multiplexed readout as for the multiplexed readout, taking an accuracy of $\pm 1°$ for the tilt angle of the detector into account. For both readouts, towards lower amplification voltages, the reconstructed angle gets much lower than the uncertainty range of the angle setting of the detector. This is due to the lower signal pulse heights. The accuracy of the signal fit (see chapter 2) decreases for too low pulse heights and thus the uncertainty of the timing increases.
The discrepancy of the reconstructed angle between the two readouts is approximately the same for all amplification voltages. This can either result from a slight change of the twist of the detector when the adapter boards were exchanged or from a not perfectly determined drift velocity of the electrons (see chapter 2.1.2). Actually the simulated drift velocity (see figure B.1) differed from the measured drift velocity which is an indicator for a pollution of the gas mixture.
If the amplification voltages are high enough (e.g. $U_{\text{ampl}} = 440\,\text{V}$) the angle reconstruction works for the multiplexed readout (see figure 6.11).

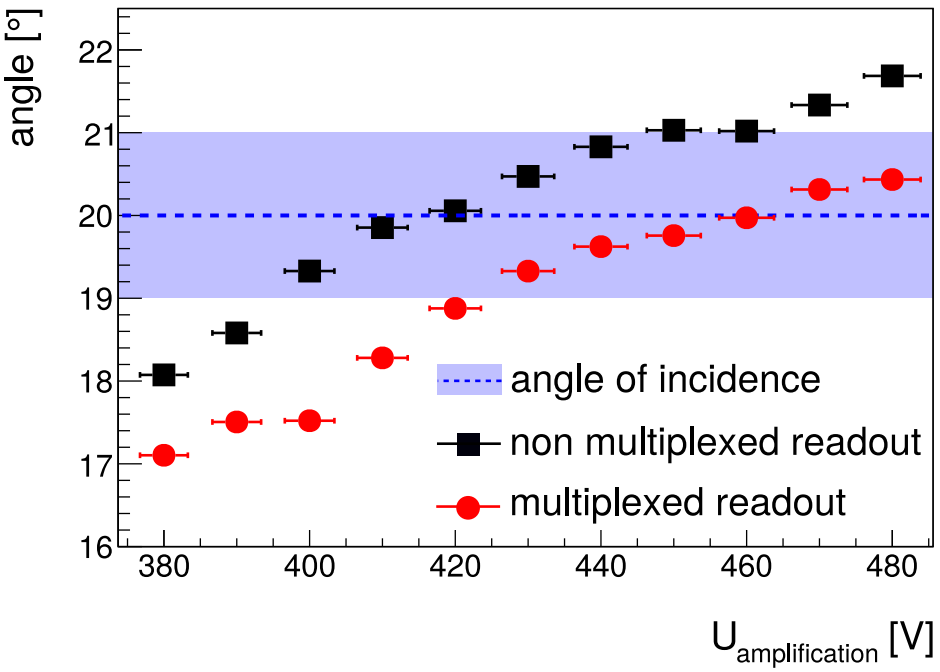

Figure 6.10: Reconstructed angle for 20MeV protons traversing the TZ detector in dependence of the amplification voltage.
The detector is tilted by an angle of $\Theta \approx 20°$. The reconstructed angle differs for every amplification voltage by an constant angle of $\approx 1°$. This is due to a not perfectly adjusted twist of the detector. The increase of the angle for the non-multiplexed readout at $U_{\text{ampl}} \geqslant 460\,\text{V}$ is due to saturation effects of the APV.

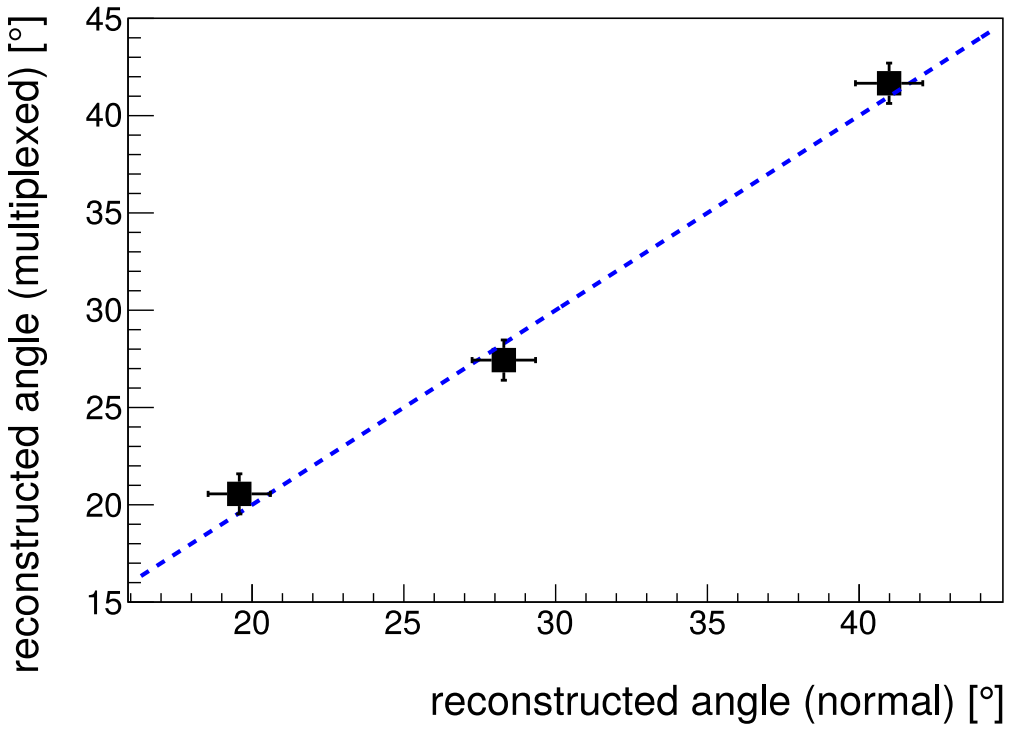

Figure 6.11: Reconstructed angle with the multiplexed readout plotted against the reconstructed angle with the non-multiplexed readout for different angles of incidence ($\Theta \in \{20°, 30°, 40°\}$).
The error of the tilted angle of the detector $\Delta\Theta = \pm 1°$ is considered within the error bars. The ideal case where the reconstructed angle with the multiplexed readout is equal to the reconstructed angle with the non-multiplexed readout is indicated as well. The plot is showing results for the TZ detector with $U_{\mathrm{ampl}} = 440\,\mathrm{V}$.

Angular Resolution

The angular resolution is determined as described in chapter 6.2.2 for particles traversing the detector at an angle of incidence $\Theta = 20°$. The resolution for $|\Theta| < 20°$ is nearly the same for both readouts. A slight increase of the discrepancy between both readouts is visible for $U_{\text{ampl}} < 420\,\text{V}$.
Even though figure 6.12 shows best reached resolutions for both readouts, there is a discrepancy in the resolution towards $|\Theta| > 20°$. This means that the capacitive couplings for the multiplexed readout is not perfectly corrected. It is more complex as assumed in chapter 4.4. However the angular resolution improved quite a lot by applying the charge correction (see figure 6.13).

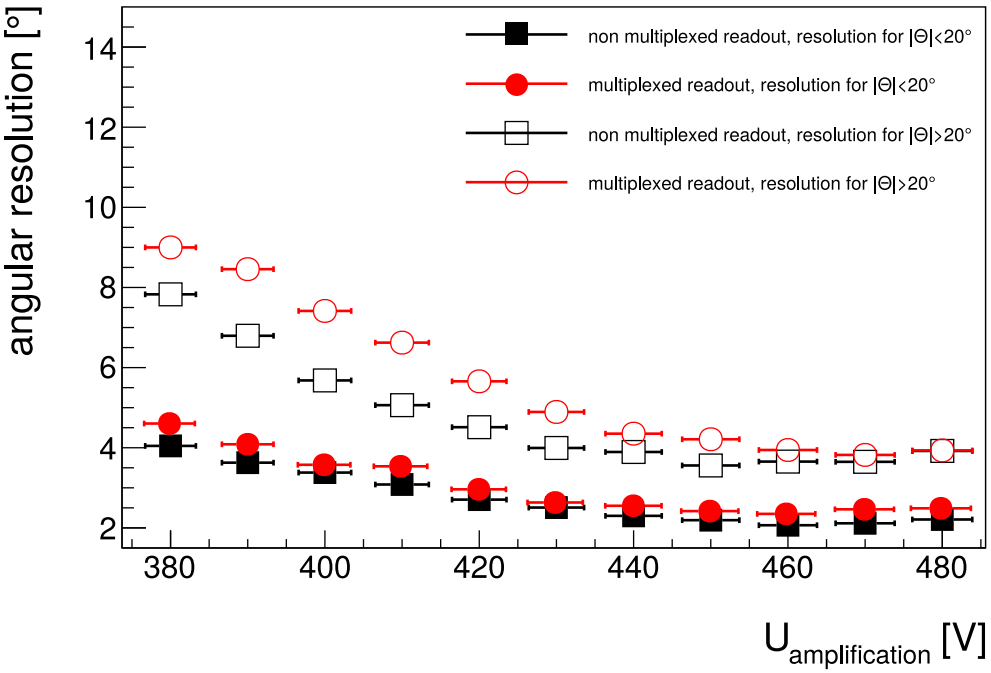

Figure 6.12: Angular resolution using the TZ detector for both readouts in dependence of the amplification voltage.
The detector is tilted by an angle of $\Theta = 20°$. The values are the width of both Gaussian fits, as shown in figure 6.6. The resolution towards $|\Theta| < 20°$ is approximately the same for both readouts. Due to a not perfectly corrected capacitive coupling, the resolution towards $|\Theta| > 20°$ differs for both types of readout. The error of the resolution is smaller as the marker size.

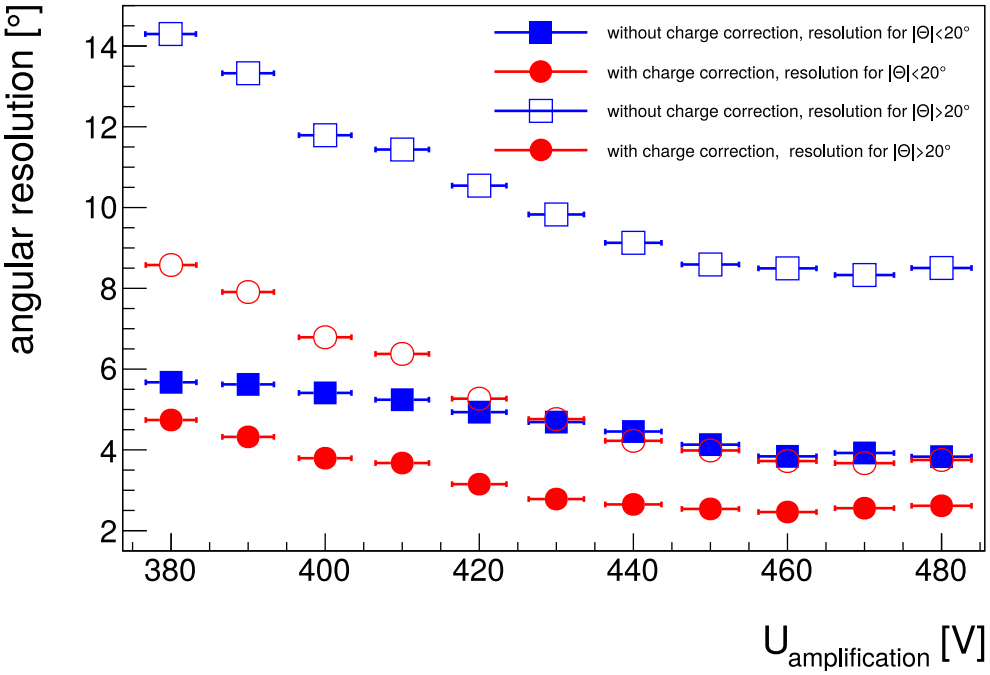

Figure 6.13: Angular resolution using the TZ detector in dependence of the amplification voltage for the multiplexed readout, before and after the charge correction is applied.
The detector is tilted by and angle of $\Theta = 20°$. The angular resolution for $|\Theta| < 20°$ and $|\Theta| > 20°$ improved significantly by applying the charge correction, which is explained in chapter 4.4.1. The error of the angular resolution is smaller as the marker size.

Angle Reconstruction Efficiency

The impact of the lower pulse height and the not properly corrected capacitive coupling is shown in the angle reconstruction efficiency (see figure 6.14). The efficiency is calculated as described in chapter 6.2.2. It is a measure for the functionality of the multiplexing adapter board.
The decrease of the efficiency for lower amplification voltages is due to the lower pulse heights, and the consequently increased probability for signal strips being rejected by the noise canceling algorithms. If the whole second cluster of electronic channels is lost the efficiency gets lower due to the false demultiplexing. Thus a wrong angle is reconstructed.
The fact that at least two strips have to be hit to reconstruct a proper angle lowers the efficiency for the multiplexed readout even if the signal is correctly demultiplexed. This and a not properly corrected capacitive coupling leads to a discrepancy between the efficiency of the multiplexed readout and the non-multiplexed readout for amplification voltages below $U_{\mathrm{ampl}} = 420\,\mathrm{V}$. For $U_{\mathrm{ampl}} \geq 420\,\mathrm{V}$ both readouts show the same angle reconstruction efficiency.

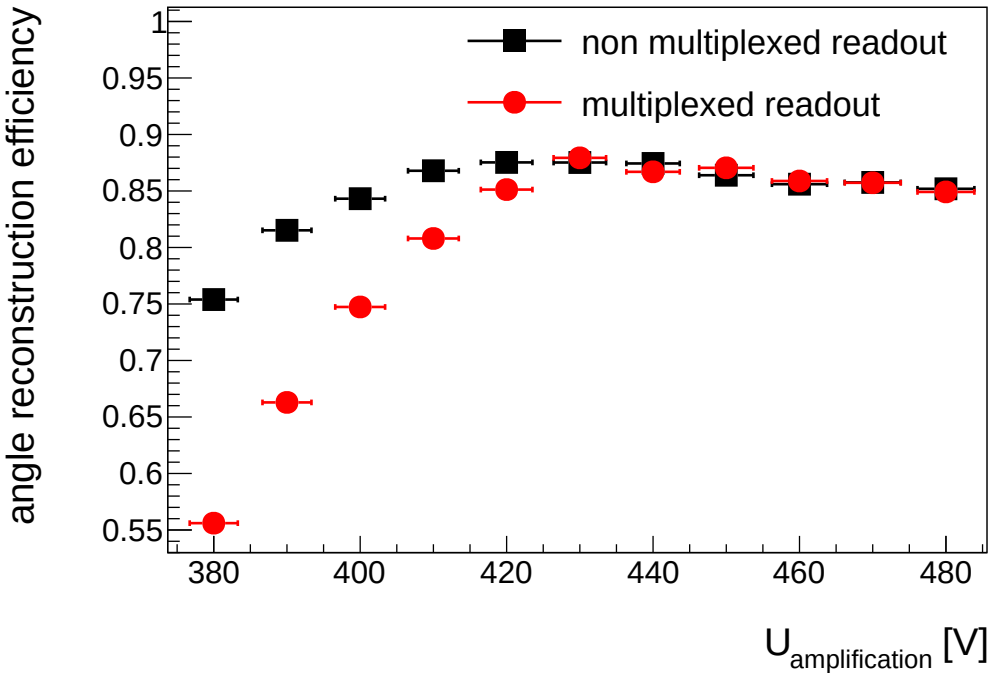

Figure 6.14: Angle reconstruction efficiency in dependence of the amplification voltage for both readouts.
The discrepancy between both readouts for lower amplification voltages originates from a combination of lost electronic clusters due to the lower pulse height, and the not totally corrected capacitive coupling.

Chapter 7

Measurements with Cosmic Muons

So far measurements were performed with a small sized detector, which was irradiated with a particle beam. To verify the functionality of the developed multiplexing adapter board with large scale detectors, measurements were performed with cosmic muon radiation in the Cosmic Ray Facility in Garching (CRF). The multiplexing adapter board was connected to the new small wheel SM2 detectors.

7.1 Cosmic Ray Facility

The Cosmic Ray Facility (CRF) consists out of two layers of BOS[1] Monitored Drift Tube (MDT) chambers (see figure 7.1). These MDT chambers are the same as the ones, used in the barrel of the ATLAS muon spectrometer (BOS) (see figure 1.1). One chamber consists out of 432 drift tubes which are split to 6 layers. Between two MDT chambers a detector can be placed for performance testing purposes. The MDT chambers allow for a high precision track reconstruction in two dimensions. For triggering 10 cm broad scintillator panels are placed on top and underneath the MDT chambers. The longitudinal axis of the scintillator bars are orientated perpendicular to the MDTs. Knowing which scintillator bar is hit, a rough particle position along the tubes is provided. A 34 cm thick iron absorber between the lower MDT chamber and the lower scintillators ensures that only muons with an energy $E_{\text{muon}} > 600\,\text{MeV}$ are selected for the measurements [Lösel, 2017]. Cosmic muons with $E_{\text{muon}} > 600\,\text{MeV}$ are minimum ionizing particles (see figure 1.2), which are hardly scattered in contrast to the 20 MeV protons, which were used for previous measurements (see equation 1.1). However a small multiple scattering can be taken into account by equation 1.1. The slopes of the muon track in both MDT chambers allow cuts to eliminate it in the analysis.

[1] BOS: Barrel Outer Small of the muon spectrometer.

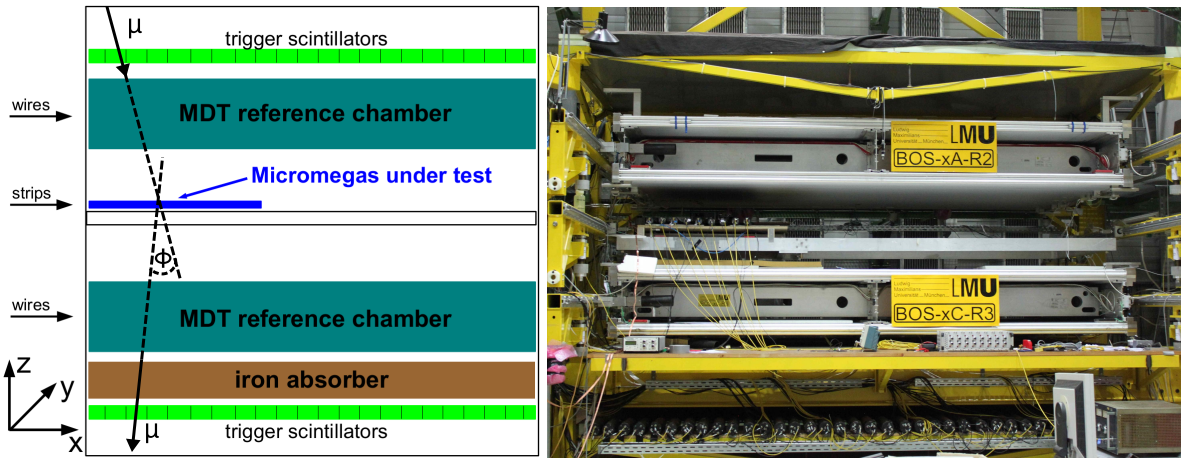

Figure 7.1: Picture (right) and schematic picture (left) of the Cosmic Ray Facility. Figures adapted from [Lösel, 2017].
A particle track is reconstructed by each MDT reference chamber. Due to multiple scattering both tracks given by each MDT chamber can differ by an angle $\Delta\Theta$. By selecting tracks with a relatively small difference $\Delta\Theta$ in the MDT tracks, multiple scattering is excluded in the tracking analysis. Furthermore the incident angle of the particles is determined via the MDT tracks.

7.2 Performed Measurements

The measurements are performed with similar detector as the previously explained SM2 detector (see chapter 5.1.2). The detector used for the cosmic measurements consists only out of two active layers. It is flushed with the gas mixture $Ar : CO_2$ 85 : 15 vol. %. Most of the readout strips are read out, using a non-multiplexed readout adapter board. On one layer 512 strips were read out by using a multiplexing adapter board (see figure 7.2). The second layer of the SM2 detector is used to determine a reference position. Therefore, the measurement is not influenced by misalignment with respect to the MDT reference track. The reference track given by the CRF is used for selection of the slope of the particle track only. To neglect multiple scattered events, the slope given by both MDT chambers needs to be about the same ($\Delta m_{\mathrm{MDT}} < 0.004$).

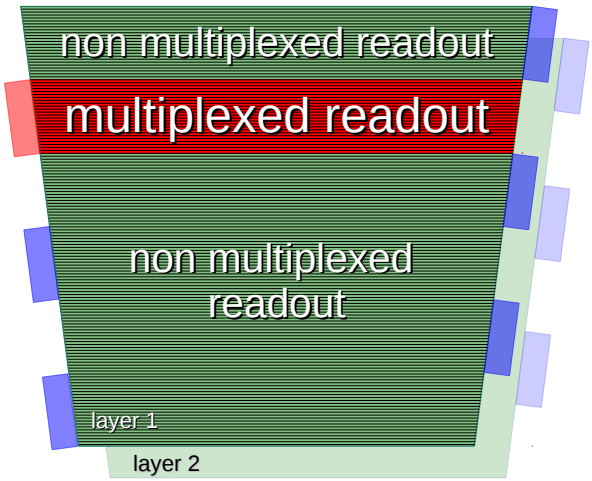

Figure 7.2: SM2 detector with two active layers.
Except of 512 readout strips on layer one, every other strip is read out with a non-multiplexed readout. 512 strips on layer two were read out with the multiplexed readout.
Layer two is used to determine a reference position.

Since only one detector is used as a reference detector the analysis procedure for the measurements is the same as for the measurements at the tandem accelerator (see chapter 6). The position reconstruction with the centroid method (see chapter 2.1.1) for the normal and the multiplexed readout are compared.
The efficiency is determined with equation 6.5. The acceptance range $[-25\,\text{mm}, 25\,\text{mm}]$ is the same as for the test beam measurements. Due to the design of the adapter board, not correctly reconstructed events are not within that range (marked events in figure 7.4).

7.3 Results

In the non-multiplexed region, the residual distribution seems to be roughly independent of the hit position (see figure 7.3). For the non-multiplexed read out detector strips, the residual is centered at zero and has roughly the same width for all hit positions. However having a closer look at the residual distribution a position dependence of the residual is visible [Herrmann, 2019]. The position of the multiplexing adapter board can clearly be identified without demultiplexing the signal. The difference between the "one to one mapped region" and the "multiplexed region", where two electronic clusters are detected, is clearly visible as well[2].
After demultiplexing the residual distribution is centered at zero. It has roughly the same width as for the non-multiplexed readout detector strips. No difference between the multiplexed and non-multiplexed region is visible for the correctly demultiplexed events.
However, $\approx 12\,\% - 18\,\%$ of all events are not correctly reconstructed. A cluster lost at the zero-suppression in the "multiplexed region", is leading into a wrong position reconstruction to the "one to one mapped region" (see figure 6.9). These are the signals with $\Delta x > 25\,\text{mm}$ in figure 7.4. Furthermore, for signals in the "one to one mapped region", a not perfectly corrected capacitive coupling and hence resulting second cluster leads to a wrong position reconstruction to the "multiplexed region" ($\Delta x < -25\,\text{mm}$ in figure 7.4).

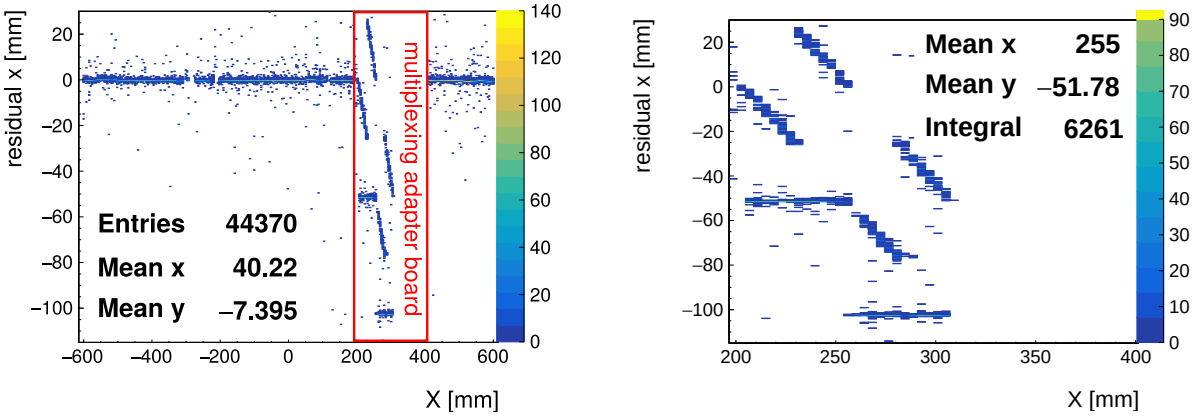

Figure 7.3: Residual distribution for all readout strips of the SM2 detector and a not demultiplexed signal.
The position of the multiplexing adapter board (red box in the left figure) is enlarged in the right figure. The two horizontal distribution originates from hits in the "one to one mapped region". The four diagonal like distributions originate from a hit in the "multiplexed region".
The measurement is taken with cosmic muons perpendicularly traversing the detector. The detector is operated with $U_{\text{ampl}} = 630\,\text{V}$ and $U_{\text{drift}} = 300\,\text{V}$

[2] In figure 7.3 the horizontal residual distribution with $res \approx -110\,\text{mm}$ and $res \approx -55\,\text{mm}$ originates from a hit in the "one to one mapped region". The four diagonal like residual distributions originate from hits in the multiplexed region.

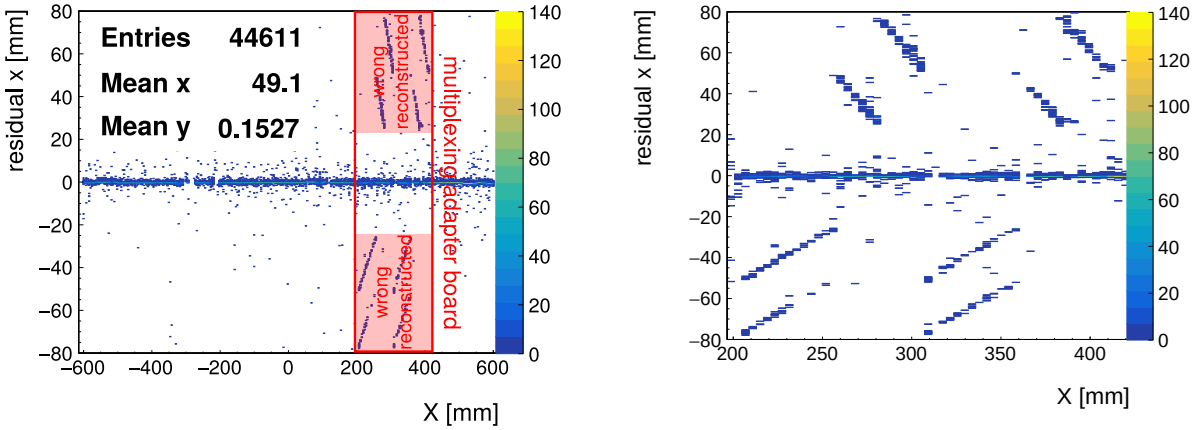

Figure 7.4: Residual distribution for all readout strips of the SM2 detector for a demultiplexed detector signal.
The position of the multiplexing adapter board (red box in the left figure) is enlarged in the right figure. Roughly 17 % of all events are demultiplexed falsely.
The measurement is taken with cosmic muons perpendicularly traversing the detector. The detector is operated with $U_{\text{ampl}} = 630\,\text{V}$ and $U_{\text{drift}} = 300\,\text{V}$

To investigate these results the demultiplexing algorithm is modified. For the previous measurements a signal is reconstructed to the "one to one mapped region", if only one cluster in the electronic channels is detected (see chapter 4.2). However, if the number of hit strips in that electronic cluster is below-average, it is a strong indication that the signal originates from a particle, traversing the detector in the "multiplexed region". In this case the second electronic cluster is lost. Therefore, the signal is falsely reconstructed to the "one to one mapped region". This is shown by the residuals above 25 mm for smaller cluster sizes (see figure 7.5). Single electronic cluster signals with a cluster size below three strips needs to be reconstructed to the "multiplexed region".
However, a fraction of these signals were already reconstructed correctly. To ensure that these signals are not wrongly reconstructed to the "multiplexed region", the charge distribution within the electronic cluster is investigated. Only if the ratio between highest strip charge and the cluster charge $(max\,(q_{\text{strip}})\,/\,\sum_{\text{cluster}} q_{\text{strip}})$ is above a threshold, the signal is reconstructed to the "multiplexed region" and not to the "one to one mapped region" (see figure 7.6). This also holds true if three strips were hit in a single electronic cluster.

The impact of the wrongly demultiplexed signals is shown in the reconstruction efficiency (see figure 7.7). For $U_{\text{ampl}} = 630\,\text{V}$ and $U_{\text{ampl}} = 640\,\text{V}$ the efficiency is approximately the same and reaches values up to $\approx 89\,\% - 91\,\%$. Due to the lower signal pulse height, and thus resulting higher probability for a signal to be wrongly discarded at the zero-suppression, the efficiency for $U_{\text{ampl}} = 620\,\text{V}$ only reaches values up to $\approx 89\,\%$.
With an increasing angle of incidence (up to $\mid \Theta \mid = 10°$), the signal is spread on a larger number of adjacent strips. The impact of missing strip signals on the demultiplexing decreases and therefore the demultiplexing efficiency increases slightly (see figure 7.7). For incident angles $\mid \Theta \mid > 10°$ the efficiency decreases again. Inhomogeneous ionization along the particle path (see figure 2.4) and a lower average strip charge are the reason for that. Signal strips are more likely rejected at the zero-suppression (see chapter 2.2.1).

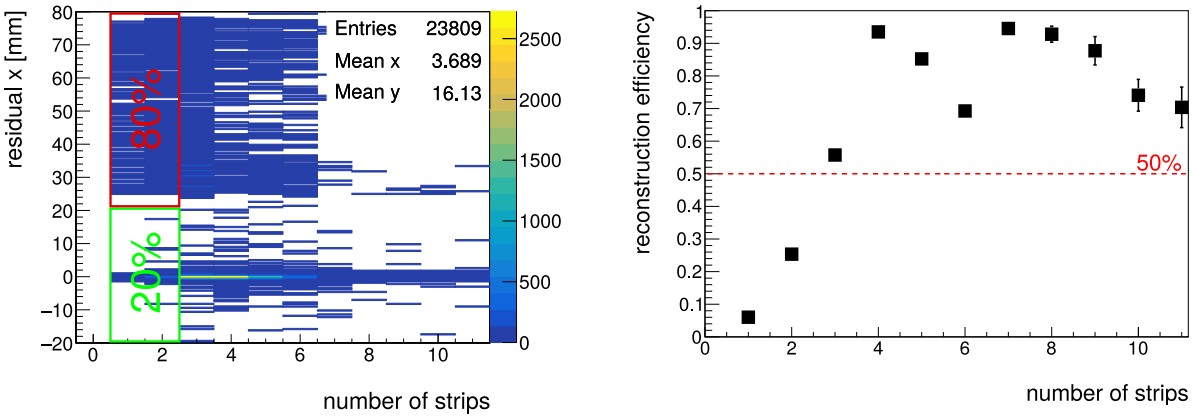

Figure 7.5: Residual distribution (left) and reconstruction efficiency (right) in dependence of the number of strips which detected a signal.
Only events with one signal cluster in the APV channels are shown. These events were all reconstructed to the "one to one mapped region". If the residual is above 25 mm the signal originates from a particle traversing the detector in the "multiplexed region". The second electronic cluster is lost. Therefore the signal is reconstructed to the "one to one mapped region".
If less than three strips are hit it is more probable that a signal originates from a particle which traversed the detector in the "multiplexed region".
The detector is operated with $U_{\text{ampl}} = 630\,\text{V}$ and $U_{\text{drift}} = 300\,\text{V}$

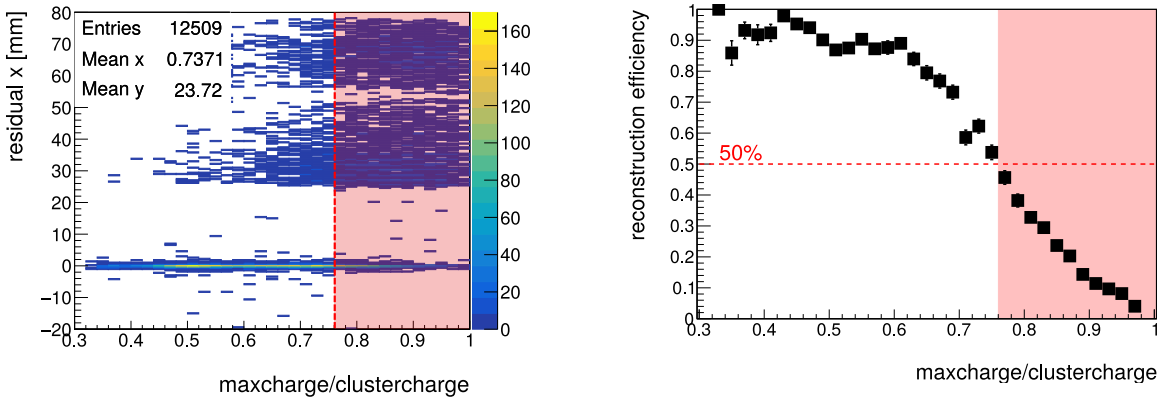

Figure 7.6: Residual distribution (left) and reconstruction efficiency (right) in dependence of the ratio $(max\,(q_{\text{strip}})/\sum_{cluster} q_{strip})$.
Only events are shown with one electronic signal cluster, and not more than four strips hit. These events were all reconstructed to the 1 to 1 mapped region. If the residual is above 25 mm the signal originates from a particle traversing the detector in the "multiplexed region". The second electronic cluster is lost and therefore the signal is reconstructed to the "one to one mapped region".
The fraction of correctly reconstructed events in dependence of the ratio $(max\,(q_{strip})\,/\,\sum_{cluster} q_{strip})$ is shown in the right figure. If this ratio exceeds 0.76 it is more probable that a signal originates from a particle which traversed the detector in the "multiplexed region".
The detector is operated with $U_{\text{ampl}} = 630\,\text{V}$ and $U_{\text{drift}} = 300\,\text{V}$

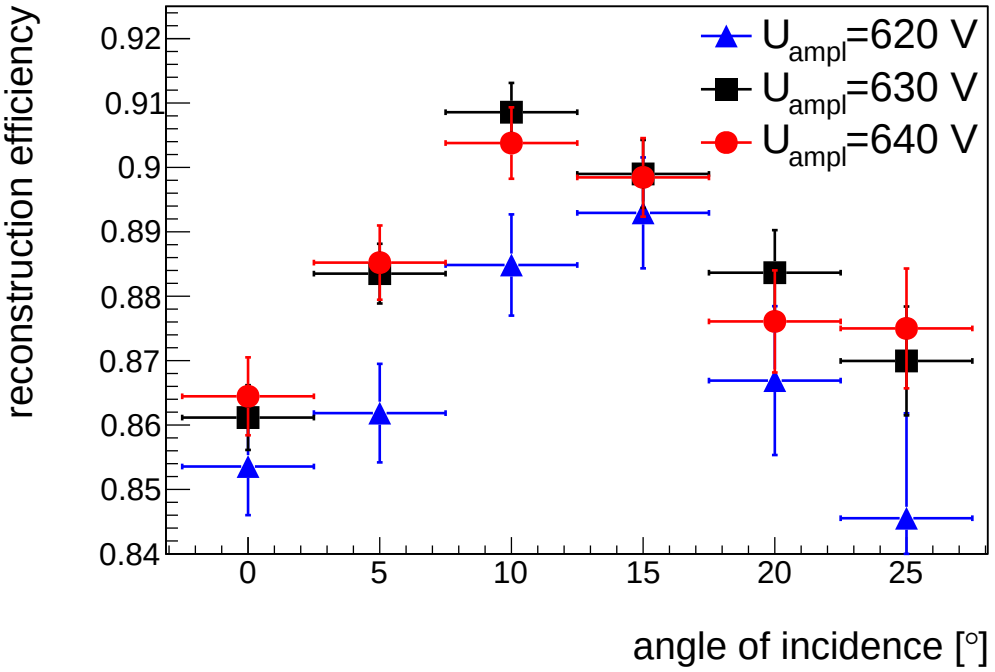

Figure 7.7: Demultiplexing efficiency for different angles of incidence and different amplification voltages.
The efficiency is calculated with equation 6.5. Hits with a residuum in the range $[-25\,\text{mm}, 25\,\text{mm}]$ are considered as correctly reconstructed events. The efficiencies are below the expected efficiency for a non-multiplexed readout, which is $\approx 96\,\%$.

Compared to the measurements at the Tandem accelerator with a small 10×10 cm^2 large Micromegas detector (see figure 6.8) the demultiplexing efficiency for the cosmic muon measurements with the SM2 detector is much smaller.
Besides the much larger capacitances of the SM2 detector and the resulting higher noise level of the detector (see figure 6.7), the different type of particle radiation used for the measurements can explain this. At the Tandem accelerator the detector is irradiated with strongly ionizing protons, which lose a large contribution of their kinetic energy inside the detector volume. The inhomogeneous ionization for protons is not as clearly pronounced as for muons. Whereas mmdaq[3] is used for the data acquisition and zero-suppression at the Tandem accelerator, the data acquisition at the CRF is done, using a program specially designed for the readout of large scale Micromegas detectors with an increased number of readout channels. The applied zero-suppression is slightly different to the zero-suppression applied in mmdaq. Due to some issues with the zero-suppression many signals were lost, even for the non-multiplexed readout detector strips. The measurement conditions can also lead to a lower demultiplexing efficiency.
However, the increased capacitance with respect to the TZ detector together with the lower primary ionization of the cosmic muons, is assumed to be the most dominant reason for the efficiency decrease. More noise can be coupled to the readout strips. The extracted charge is lower.

If the signal is reconstructed to the correct region (i.e. if a signal in the "one to one mapped region" is reconstructed to the "one to one mapped region", respectively a signal in the "mul-

[3]Mmdaq is a software used for data acquisition. Mmdaq processes the raw APV25 data and writes it to a root file [Byszewski, 2011].

tiplexed region" to the "multiplexed region"), the detector resolution using the multiplexed readout is approximately the same as for a non-multiplexed read out (see figure 7.8). Actually, the resolution of the multiplexed readout is slightly worse due to the smaller signal pulse heights. With the assumption of both detector layers showing the same resolution, $\sigma_{\text{residual distribution}}$ has to be divided by $\sqrt{2}$ to obtain the actual detector resolution, which is independent of the reference detector resolution.
Since the particle position is determined via the centroid method (see chapter 2.1.1), the resolution towards larger incident angles gets worse, as it is known from small detectors. The impact of inhomogeneous ionization along the particle path (see figure 2.4) is responsible for that.
In conclusion, the obtained resolution with the multiplexed readout is approximately the same as for the non-multiplexed readout. However detector efficiency for the multiplexed readout is clearly below the detector efficiency for the non-multiplexed readout.

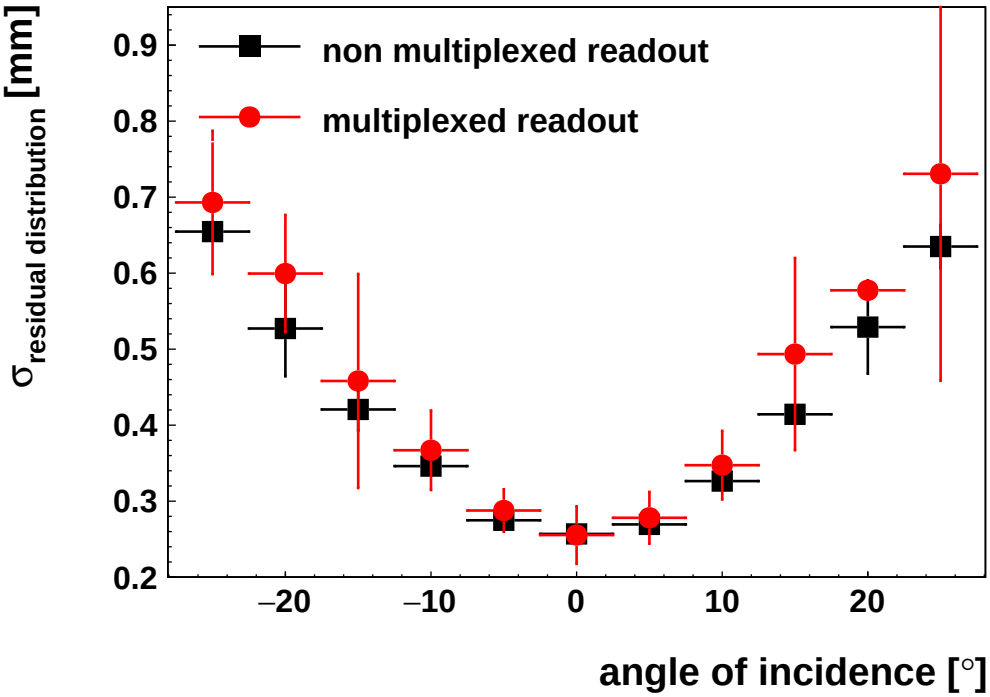

Figure 7.8: Width of the residual distribution.
A residual distribution as shown in figure 6.5 is determined for each angle ($\Theta \pm 2.5°$) and fitted with a double Gaussian function (see equation 6.3). The combined width of the double Gaussian function (see equation 6.4) is used as $\sigma_{\text{residual distribution}}$. It is a measure for the detector resolution. The uncertainty for $\sigma_{\text{residual distribution}}$ of the multiplexed readout is larger as for the normal readout due to lower statistics. Only 16 % of all readout strips were read out using the multiplexing adapter board. Due to the lower signal pulse height, the resolution for the multiplexed readout is slightly worse as for the non-multiplexed readout. The detector is operated with $U_{\text{ampl}} = 630\,\text{V}$ and $U_{\text{dirft}} = 300\,\text{V}$. For other amplification voltages see figure C.1 in the appendix.

Chapter 8

Summary and Outlook

For this thesis a multiplexed readout for strip Micromegas detectors was developed and tested. The multiplexing is executed on an adapter board. Two strips are hereby combined to one electronic readout channel. For an unambiguous position determination the distance between strips connected to the same electronic channel has to vary. An iterative algorithm has been developed to define the sequence of the multiplexing scheme. The adapter board combines the APV25 readout chip on one side with the Micromegas detector on the other side.
With a number of combined strips, the capacitance connected to one electronic channel increases. Therefore, the signal pulse height, which is extracted from the readout strips, decreases. This is shown by measurements performed at the SPS at CERN (see figure 5.4). To minimize the decrease in pulse height it was decided to develop a multiplexing scheme, which reduces the electronics by a factor of two only.

Due to the complex capacitive coupling on the adapter board (see figure 4.10), some reconstructed positions are favored above others (see figure 4.16). By measuring the capacitances between the strip lines on the board a charge correction for the multiplexed readout was developed.

The multiplexing adapter board was tested in two steps, using a small and a large detector. Its fundamental properties were tested at the Tandem accelerator in Garching using a Micromegas detector with a readout strip length of 10 cm only, neglecting the influence of the increased detector capacitance. A 20 MeV proton beam was used with an intensity of several kHz/cm^2. By applying the charge correction, a smooth Gaussian beam profile is reconstructed (see figure 4.18). For large enough amplification voltages ($U_{\text{ampl}} \geq 400\,\text{V}$), the multiplexed signal is mostly reconstructed to the correct region of the detector. The position reconstruction efficiency is approximately the same for the multiplexed and for the non-multiplexed detector readout (see figure 6.8).

The angle reconstruction using the µTPC method was studied at the Tandem accelerator as well. The reconstructed angle shows the same behavior for both readouts. For high enough amplification voltages ($U_{\text{ampl}} \geq 400\,\text{V}$), the reconstructed angle is within the error range of the incident angle (see figure 6.10). The angular resolution (see figure 6.12), as well as the angle reconstruction efficiency is about the same for these voltages (see figure 6.14). A not perfectly corrected capacitive coupling results in a worse angular resolution and a worse angle reconstruction efficiency for lower amplification voltages. This is also favored by the decrease of the signal pulse height and the associated strip signal loss due to the zero-suppression(see chapter 2.2.1).

The multiplexed readout for large scale Micromegas detectors was tested with cosmic muons. The detector resolution is about the same for the multiplexed readout and the non-multiplexed readout (see figure 7.8). However, the detector efficiency, determined with equation 6.7 ($\approx 85\,\% - 91\,\%$), is below the expected efficiency ($\approx 96\,\%$) (see figure 7.7). In a number of events only two or one strips are hit, due to the loss of electronic channels at the zero-suppression. Thus, the signal is often reconstructed to the wrong region of the detector. Some issues with the zero-suppression algorithm can be responsible for that. To apply the multiplexed readout to the large scale Micromegas detectors, an improvement of the zero-suppression, as well as an improvement of the charge correction is needed.

Another, more simple option, might be the modification of the double sided multiplexing (see chapter 3.1.1). Since the developed multiplexed readout should be applied to a Micromegas detector with four active detector layers, one detector layer can be used instead of the second readout strip layer (see figure 8.1). This detector layer must be read out with a non-multiplexed readout. All the other detector layers are read out using a readout which connects multiple readout strips to one electronic channel. For example the first 128 readout strips are mapped to 128 electronic channels. The second 128 readout strips are than again mapped in the same order to the same 128 electronic channels. Since neighboring strips are mostly connected to neighboring channels, the centroid position (see chapter 2.1.1) is not affected by the capacitive coupling. No favored positions, as shown in figure 4.16, are expected. A more simple charge correction, similar to chapter 2.3 can be applied. Furthermore, since mostly only one electronic cluster is expected, missing strips do not lead to a wrong position reconstruction as it is shown in figure 6.9.

In conclusion, for high enough amplification voltages, the developed multiplexed readout works for small sized detectors. For a detector with a readout strip length of 10 cm this is shown. For large scale detectors either the capacitive coupling and zero-suppression needs to be improved, or a different, more simple multiplexing scheme needs to be applied.

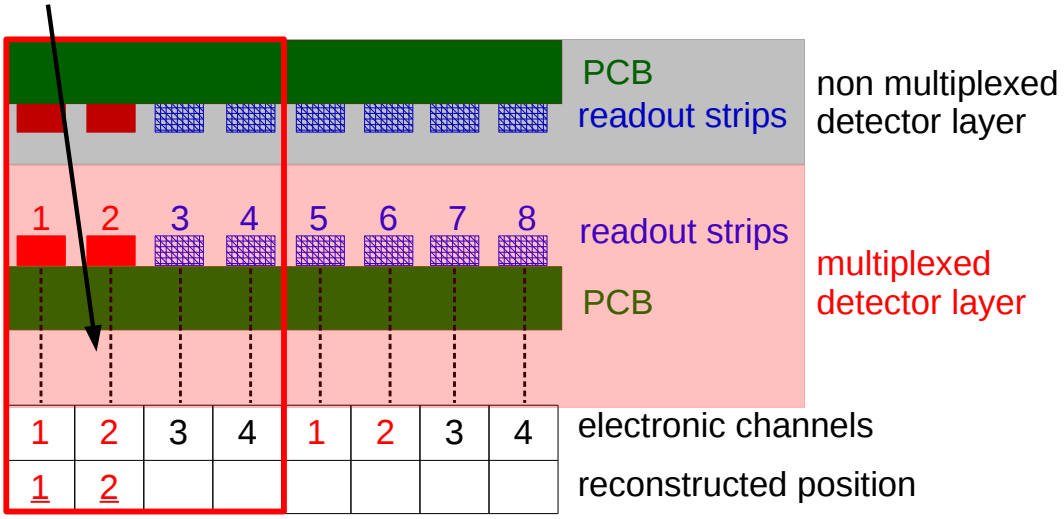

Figure 8.1: Working principle of the double sided multiplexing for a multi layer Micromegas detector (in this example a double layer Micromegas detector is shown).
One of the detector layers must be read out with a non-multiplexed readout. All the other detector layers are read out with a multiplexed readout. Neighboring strips are connected to neighboring channels. The mapping is repeated periodically (in this example every four strips).
Assuming a particle (↘) traversing the detector at the first two strips (indicated in red). A precise particle position is determined via the non-multiplexed detector layer. This limits the particle position to one multiplexing period, or even more precise (red box). The particle position is reconstructed to the strips $\{\underline{1}, \underline{2}\}$, which are connected to the electronic signal channels $\{1, 2\}$. Strips $\{5, 6\}$ which are also connected to the same electronic signal channels, can be excluded as signal strips. These strips are outside of the expectation range (red box).

Bibliography

[Abbon et al.(2007)] Ph Abbon, E Albrecht, V Yu Alexakhin, Yu Alexandrov, GD Alexeev, MG Alekseev, Antonio Amoroso, H Angerer, VA Anosov, B Badełek, et al. The COMPASS experiment at CERN. *Nuclear Instruments and Methods in Physics Research Section A: Accelerators, Spectrometers, Detectors and Associated Equipment*, 577(3):455–518, 2007. doi:10.1016/j.nima.2007.03.026.

[Alexopoulos et al.(2011)] T. Alexopoulos, J. Burnens, R. de Oliveira, G. Glonti, O. Pizzirusso, V. Polychronakos, G. Sekhniaidze, G. Tsipolitis, and J. Wotschack. A spark-resistant bulk-micromegas chamber for high-rate applications. *Nuclear Instruments and Methods in Physics Research A*, 640:110–118, June 2011. doi:10.1016/j.nima.2011.03.025.

[ATLAS(2019)] ATLAS. Detector & technology — ATLAS experiment at CERN. website, May 2019. URL `http://atlas.cern/discover/detector`.

[ATLAS-Muon-Collaboration(2014)] ATLAS-Muon-Collaboration. Micromegas construction manual. July 2014. URL `https://edms.cern.ch/document/1400217/1`.

[Baum et al.(1996)] Guenter Baum et al. COMPASS: A Proposal for a Common Muon and Proton Apparatus for Structure and Spectroscopy. 1996.

[Bernhard(2018)] Flierl Bernhard. *Particle Tracking with Micro-Pattern Gaseous Detectors*. PhD thesis, Ludwig-Maximilians-Universität München, 2018. URL `https://nbn-resolving.org/urn:nbn:de:bvb:19-221980`.

[B&K-Precision-Corporation()] B&K-Precision-Corporation. *Model 878B, 879B, Dual Display LCR Meter Instruction Manual*. URL `https://bkpmedia.s3.amazonaws.com/downloads/manuals/en-us/87xB_manual.pdf`.

[Blum et al.(2008)] Walter Blum, Werner Riegler, and Luigi Rolandi. *Particle detection with drift chambers; 2nd ed.* Springer, Berlin, 2008. URL `https://cds.cern.ch/record/1105920`.

[Bortfeldt(2014)] Jonathan Bortfeldt. *Development of Floating Strip Micromegas Detectors*. PhD thesis, Ludwig-Maximilians-Universität München, 2014. URL `https://nbn-resolving.org/urn:nbn:de:bvb:19-169727`.

[Byszewski(2011)] Marcin Byszewski. mmdaq. CERN, 2011. URL `https://indico.cern.ch/event/132080/contributions/1356987/attachments/98068/139968/byszewski_rd51mtng_mamma_daq.pdf`.

[CERN(2019a)] CERN. The large hadron collider. website, June 2019a. URL `https://home.cern/science/accelerators/large-hadron-collider`.

[CERN(2019b)] CERN. The super proton synchrotron. website, April 2019b. URL `https://home.cern/science/accelerators/super-proton-synchrotron`.

[Frauenfelder and Henley(1987)] H. Frauenfelder and E.M. Henley. *Teilchen und Kerne*. Oldenbourg Verlag GmbH, 1987.

[Giomataris et al.(2006)] I. Giomataris, R. De Oliveira, S. Andriamonje, S. Aune, G. Charpak, P. Colas, A. Giganon, Ph. Rebourgeard, and P. Salin. Micromegas in a bulk. *Nucl. Instrum. Meth.*, A560:405–408, 2006. doi:10.1016/j.nima.2005.12.222.

[Giomataris et al.(1996)] Ioanis Giomataris, P C Rebourgeard, J P Robert, and Georges Charpak. Micromegas: A high-granularity position-sensitive gaseous detector for high particle-flux environments. *Nuclear Instruments and Methods in Physics Research Section A Accelerators Spectrometers Detectors and Associated Equipment*, 376, 06 1996. doi:10.1016/0168-9002(96)00175-1.

[Herrmann(2019)] Maximilian Herrmann. *PHD thesis in process*. PhD thesis, LMU Munich, 2019.

[Iakovidis(2014)] Georgios A. Iakovidis. *Research and Development in Micromegas Detector for the ATLAS Upgrade*. PhD thesis, National Technical University of Athens, 2014. URL `https://inspirehep.net/record/1339824`.

[Iodice(2015)] M. Iodice. Micromegas detectors for the muon spectrometer upgrade of the atlas experiment. *JINST*, 10(02):C02026, 2015. doi:10.1088/1748-0221/10/02/C02026.

[Jones(2001)] L. Jones. *APV25-S1 User Guide*, September 2001. URL `https://cds.cern.ch/record/1069892/files/cer-002725643.pdf`.

[Kawamoto et al.(2013)] T. Kawamoto et al. New small wheel technical design report. 2013. URL `https://inspirehep.net/record/1614083`.

[Kleinknecht(2005)] Konrad Kleinknecht. *Detektoren für Teilchenstrahlung*. Teubner Studienbücher. Teubner, Stuttgart, 4. edition, 2005.

[Lynch and Dahl(1991)] Gerald R. Lynch and Orin I. Dahl. Approximations to multiple Coulomb scattering. *Nucl. Instrum. Meth.*, B58:6–10, 1991. doi:10.1016/0168-583X(91)95671-Y.

[Lösel(2017)] Philipp Lösel. *Precision Calibration of Large Area Micro Pattern Gaseous Detectors*. PhD thesis, LMU Munich, 2017. URL `https://nbn-resolving.org/html/urn:nbn:de:bvb:19-212513`.

[Maier-Leibnitz-Laboratorium(2014)] Maier-Leibnitz-Laboratorium. Broschüre für besucher. January 2014. URL `https://www.mll-muenchen.de/tandem/besucherinfo/besucherinfo.pdf`.

[Procureur et al.(2013)] S. Procureur, R. Dupré, and S. Aune. Genetic multiplexing and first results with a 50x50cm^2 Micromegas. *Nucl. Instrum. Meth.*, A729:888–894, 2013. doi:10.1016/j.nima.2013.08.071.

[Raether(1964)] H Raether. *Electron avalanches and breakdown in gases*. Butterworths advanced physics series. Butterworths, London, 1964. URL `https://cds.cern.ch/record/102989`.

[RD51-collaboration(2010)] RD51-collaboration. *Scalable Readout System (SRS)*, 2010. URL `http://rd51-public.web.cern.ch/RD51-Public/Activities/Documents/WG5SRS.pdf`.

[RD51-collaboration(2012)] RD51-collaboration. Srs - short user guide. April 2012. URL `https://espace.cern.ch/rd51-wg5/srs/Documentation/SRS_Short_User_Guide.pdf`.

[Sauli(1997)] F Sauli. Gem: A new concept for electron amplification in gas detectors. *Nuclear Instruments Methods in Physics Research Section A*, 386:531–534, 02 1997. doi:10.1016/S0168-9002(96)01172-2.

[Stelzer(2016)] Bernd Stelzer. The new small wheel upgrade project of the atlas experiment. *Nucl. Part. Phys. Proc.*, 273-275:1160–1165, 2016. doi:10.1016/j.nuclphysbps.2015.09.182.

[Tanabashi(2018)] M. et al. Tanabashi. Review of Particle Physics. *Phys. Rev.*, D98(3):030001, 2018. doi:10.1103/PhysRevD.98.030001.

[Townsend(1910)] Sir Townsend, John. *The theory of ionization of gases by collision.* London, Constable & Company, ltd., 1910.

Appendix A

Multiplex mapping

Table A.1: Used mapping for the presented multiplexing. For each strip number the connected channel number is shown.

strip number	channel number	strip number	channel number	strip number	channel number	strip number	channel number
1	0	65	64	129	65	193	97
2	1	66	65	130	1	194	33
3	2	67	66	131	67	195	99
4	3	68	67	132	64	196	96
5	4	69	68	133	0	197	32
6	5	70	69	134	66	198	98
7	6	71	70	135	2	199	34
8	7	72	71	136	68	200	100
9	8	73	72	137	4	201	36
10	9	74	73	138	70	202	102
11	10	75	74	139	6	203	38
12	11	76	75	140	3	204	35
13	12	77	76	141	69	205	101
14	13	78	77	142	5	206	37
15	14	79	78	143	71	207	103
16	15	80	79	144	7	208	39
17	16	81	80	145	73	209	105
18	17	82	81	146	9	210	41
19	18	83	82	147	75	211	107
20	19	84	83	148	72	212	104
21	20	85	84	149	8	213	40
22	21	86	85	150	74	214	106
23	22	87	86	151	10	215	42
24	23	88	87	152	76	216	108
25	24	89	88	153	12	217	44
26	25	90	89	154	78	218	110
27	26	91	90	155	14	219	46
28	27	92	91	156	11	220	43
29	28	93	92	157	77	221	109
30	29	94	93	158	13	222	45
31	30	95	94	159	79	223	111
32	31	96	95	160	15	224	47
33	32	97	96	161	81	225	113
34	33	98	97	162	17	226	49
35	34	99	98	163	83	227	115
36	35	100	99	164	80	228	112
37	36	101	100	165	16	229	48
38	37	102	101	166	82	230	114
39	38	103	102	167	18	231	50
40	39	104	103	168	84	232	116
41	40	105	104	169	20	233	52
42	41	106	105	170	86	234	118
43	42	107	106	171	22	235	54
44	43	108	107	172	19	236	51
45	44	109	108	173	85	237	117
46	45	110	109	174	21	238	53
47	46	111	110	175	87	239	119
48	47	112	111	176	23	240	55
49	48	113	112	177	89	241	121
50	49	114	113	178	25	242	57
51	50	115	114	179	91	243	123
52	51	116	115	180	88	244	120
53	52	117	116	181	24	245	56
54	53	118	117	182	90	246	122
55	54	119	118	183	26	247	58
56	55	120	119	184	92	248	124
57	56	121	120	185	28	249	60
58	57	122	121	186	94	250	126
59	58	123	122	187	30	251	62
60	59	124	123	188	27	252	59
61	60	125	124	189	93	253	125
62	61	126	125	190	29	254	61
63	62	127	126	191	95	255	127
64	63	128	127	192	31	256	63

Appendix B

Simulated Drift Velocity

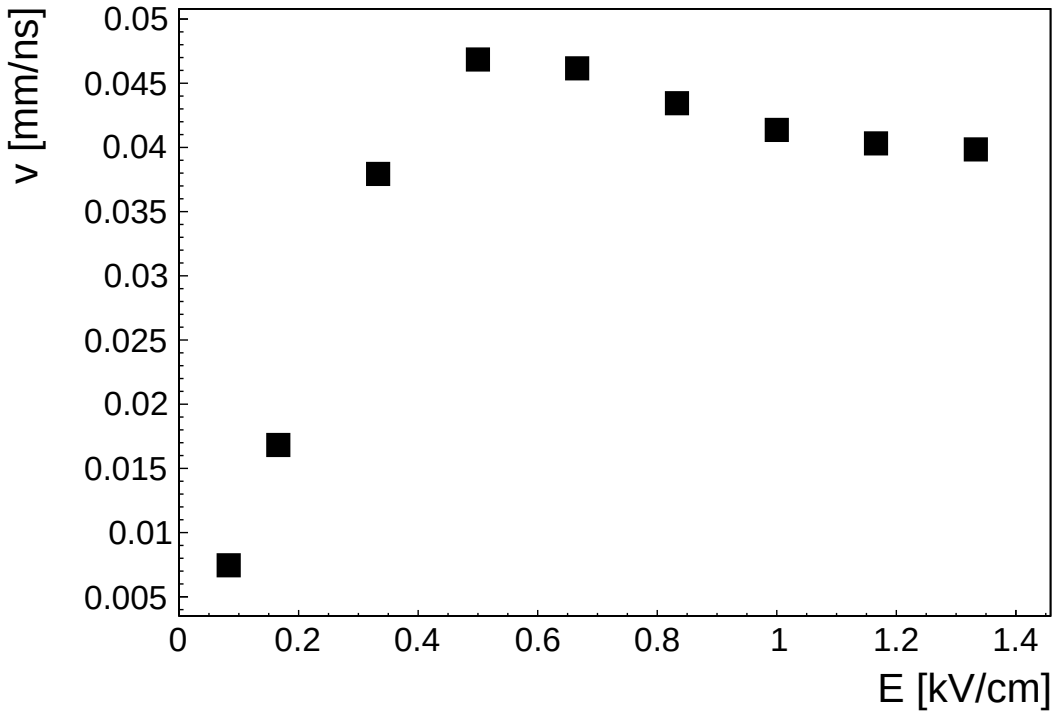

Figure B.1: Drift velocity simulated with MAGBOLTZ for the gas mixture: $AR : CO_2$ $93 : 7$ $vol.\%$. The drift velocity is depending on the the drift field.

Appendix C

Measurements with Cosmic Muons

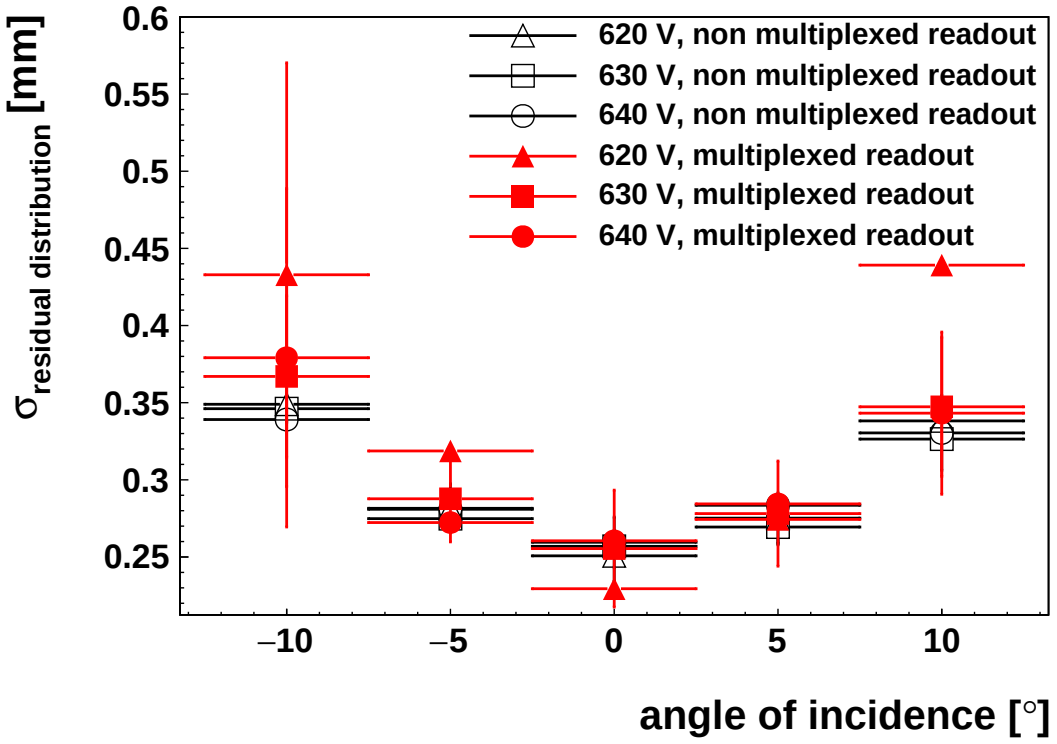

Figure C.1: Width of the residual distribution for different amplification voltages.
A residual distribution as shown in figure 6.5 is determined for each shown angle ($\Theta \pm 2.5°$) and voltage. It is fit with a double Gaussian function (see equation 6.3). The width of the double Gaussian function is used as $\sigma_{\text{residual distribution}}$. It is a measure for the detector resolution.
The statistics for incident angles $|\Theta| < 10°$ is too low to determine a proper $\sigma_{\text{residual distribution}}$.

Acknowledgments

At this point, I would like to thank the people that supported me during the last year:

- I want to thank Prof. Dr. Otmar Biebel for giving me the opportunity to write my master thesis in his group as well as for the proofreading of my thesis.
- I want to thank Dr. Ralf Hertenberger for the instructive discussions during the last year and for the proofreading of my thesis.
- I want to thank Dr. Andre Zibell for helping me to design the PCB for the multiplexed readout
- Especially I want to thank the whole detector group, Maximillian Herrmann, Maximilian Rinnagel, Dr. Felix Klitzner, Dr. Ralph Müller, Dr. Philipp Lösel, Dr. Chrysostomos Valderanis and Atila Varga,for the instructive discussions and for never becoming tired of answering questions.

I am truely sorry if I forgot anyone.

Declaration of academic integrity

I hereby declare, that this thesis is my own work and that I have not used any sources and aids other than those stated in the thesis.

Christoph Jagfeld

Munich, June 11, 2019